

EXPERIMENTAL INVESTIGATION OF SUPERSONIC LAMINAR,  
TWO-DIMENSIONAL BOUNDARY LAYER SEPARATION  
IN A COMPRESSION CORNER WITH AND WITHOUT COOLING

Thesis by  
John Eldon Lewis

In Partial Fulfillment of the Requirements  
For the Degree of  
Doctor of Philosophy

California Institute of Technology  
Pasadena, California

1967

(Submitted November 15, 1966)

### ACKNOWLEDGMENTS

I wish to express my sincere gratitude and indebtedness to Professors Lester Lees and Toshi Kubota who suggested, supervised and contributed significantly to this research.

I wish to thank Mrs. T. Van Harreveld for her assistance in reducing the data; the staff of the GALCIT Hypersonic Wind Tunnel, P. Baloga, S. Roman, G. Van Halewyn, J. Van Dijk and H. Mazurowski and the staff of the Jet Propulsion Laboratory's Supersonic Wind Tunnel for their assistance during the wind tunnel tests; the staff of the Aeronautics Shop, particularly G. Carlson and A. Slater, for manufacturing the models and probes; and Mrs. V. Conner and Mrs. E. Fox for their careful typing of this thesis.

I wish to acknowledge the receipt of a Graduate Research Assistantship from the California Institute of Technology for the academic year 1962-1963 and the TRW Fellowship for the academic years 1963-1966.

I wish particularly to thank my wife Maryann and my parents for their encouragement and support.

This work was carried out under the sponsorship and with the financial support of the U. S. Army Research Office and the Advanced Research Projects Agency under Contract No. DA-31-124-ARO(D)-33. This research is a part of Project DEFENDER sponsored by the Advanced Research Projects Agency.

## ABSTRACT

An experimental investigation of the boundary layer separation associated with a compression corner was conducted in the GALCIT Mach 6 wind tunnel, and a supplementary study was performed in the JPL supersonic wind tunnel. Special emphasis was placed on the development of a wind tunnel model which approximated true two-dimensional flow, and which could be run in either a highly cooled or an adiabatic configuration. The basic measurements consist of the model surface pressure and temperature, and Pitot surveys of the boundary layer. The surface pressure distributions for the adiabatic wall configurations are compared with the theory of Lees and Reeves (modified by Klineberg and Lees). The surface pressure distribution for the cold wall was compared with the adiabatic configuration for a laminar interaction, and the dependence on Reynolds number for both laminar and transitional interactions are observed. The "free interaction" similarity suggested by Chapman is empirically tested and found to be a good approximation for the adiabatic configuration, but it fails to correlate the cooled with the adiabatic case. The scaling suggested by Curle was tested and found to eliminate this deficiency.

## TABLE OF CONTENTS

PART	TITLE	PAGE
	Acknowledgments	ii
	Abstract	iii
	Table of Contents	iv
	List of Figures	vii
	List of Symbols	xi
1.	INTRODUCTION	1
2.	EXPERIMENTAL APPARATUS	4
2.1.	Wind Tunnels and Free Stream Conditions	4
2.2.	Models and Surface Instrumentation	4
2.2.1.	Models Tested in JPL Supersonic Wind Tunnel	4
2.2.2.	Models Tested in GALCIT Mach 6 Wind Tunnel	5
2.3.	Probe Measurements	7
2.3.1.	Pitot Measurements	7
2.3.2.	Fluctuation Measurements	7
2.4.	Data Reduction	8
3.	TWO-DIMENSIONALITY	9
3.1.	Definition and Approach	9
3.2.	Preliminary Measurements	10
3.3.	JPL Aspect Ratio Study	11
3.4.	Reynolds Number Correlation	13
4.	PURELY LAMINAR FLOW WITH AND WITHOUT COOLING	14
4.1.	Confirmation of Laminar Flow	14

## TABLE OF CONTENTS (Cont'd)

PART	TITLE	PAGE
	4.1.1. Adiabatic Model (C-1)	15
	4.1.2. Cold Model (C-1)	16
4.2.	Laminar Flow	18
	4.2.1. Experimental Correlations	18
	4.2.1.1. Effect of Cooling	18
	4.2.1.2. Effect of Reynolds Number	19
	4.2.2. Comparison with Lees-Reeves Theory	19
5.	TRANSITION	22
	5.1. Observations of Transition and its Effect	22
	5.2. Fluctuation Measurements (GALCIT, Model X-1, adiabatic wall, $M_{\infty} = 6.06$ )	24
	5.3. Model Correlations	26
	5.3.1. Two Model Correlation (JPL, Models AR-1 and 2, Adiabatic Wall, $M_{\infty} = 4.0$ )	26
	5.3.2. Reynolds Number Correlation (GALCIT, Models X-1, 3 and 4, Adiabatic, $M_{\infty} = 6.60$ )	27
6.	FREE INTERACTION	29
7.	SUMMARY	39
	7.1. Two-Dimensionality	39
	7.2. Laminar Flow	39
	7.3. Transition	40
	7.4. Free Interaction	41
	7.5. Suggestions for Future Work	41

## TABLE OF CONTENTS (Cont'd)

PART	TITLE	PAGE
	REFERENCES	43
	APPENDIX 1	45
	APPENDIX 2	48
	FIGURES	57

## LIST OF FIGURES

NUMBER		PAGE
1.	JPL Wind Tunnel Models AR-1, -2.	57
2.	JPL Wind Tunnel Models AR-1, -2.	58
3.	GALCIT Wind Tunnel Model C-1.	59
4.	GALCIT Wind Tunnel Model C-1.	60
5.	Surface Pressure Measurement Repeatability Check.	61
6.	Thermocouple Calibration.	62
7.	Liquid Nitrogen Pumping System.	63
8.	GALCIT Wind Tunnel Models X-1, -3 and -4.	64
9.	GALCIT Wind Tunnel Model S-1.	65
10.	Idealized Geometric Configuration.	66
11.	Side Plate Configuration.	67
12.	External Flow Field of Separation Interaction.	68
13.	Aspect Ratio Variation.	69
14.	Effect of Side Plate Removal.	70
15.	Side Plate Disturbance to Otherwise Clean Flow (Model AR-1).	71
16.	Aspect Ratio Variation on "Two-dimensional" Model AR-2 with Comparison to "Stovepipe," Model AR-2.	72
17.	Reynolds Number Correlation.	73
18.	Pre-separation Mach Number Profiles (Adiabatic Wall).	74
19.	Pre-separation Mach Number Profile Comparison with Theoretical Prediction (Adiabatic Wall).	75
20.	Reattachment Profiles (Adiabatic Wall) at $Re_{xc} = .15 \times 10^6$ .	76

NUMBER		PAGE
21.	Reattachment Profiles at "Test Station" with Increasing Reynolds Number (Adiabatic Wall).	77
22.	Pre-separation Mach Number Profiles (Cold Wall).	78
23.	Pre-separation Mach Number Profile Comparison with Theoretical Prediction (Cold Wall).	79
24.	Reattachment Profiles (Cold Wall) at $Re_{x_c} = .15 \times 10^6$ .	80
25.	Reattachment Profiles at "Test Station" with Increasing Reynolds Number (Cold Wall).	81
26.	External Flow Field (Adiabatic Wall).	82
27.	External Flow Field (Cold Wall).	83
28.	Effect of Cooling on Overall Laminar Boundary Layer Separation.	84
29.	Effect of Cooling Beyond Initial Pressure Level and Boundary Layer Scaling.	85
30.	Reynolds Number Dependence (Laminar Flow).	86
31.	Comparison of Experimental Pressure Distribution with Shock Wave-Boundary Layer Interaction Theory.	87
32.	Comparison of Experimental Form Factor, $H$ , with Shock Wave-Boundary Layer Interaction Theory.	88
33.	Comparison of Experimental Pressure Distribution with Shock Wave-Boundary Layer Interaction Theory.	89
34.	Comparison of Experimental Pressure Distribution with Shock Wave-Boundary Layer Interaction Theory.	90



NUMBER		PAGE
35.	Comparison of Experimental Pressure Distribution with Shock Wave-Boundary Layer Interaction Theory.	91
36.	Comparison of Experimental Pressure Distribution with Shock Wave-Boundary Layer Interaction Theory, Including Reynolds Number Correlation.	92
37.	Shadowgraph of Model AR-1 at $M_\infty = 4.0$ , $Re_{x_c} = .27 \times 10^6$	93
38.	Shadowgraph of Model AR-1 at $M_\infty = 4.0$ , $Re_{x_c} = .89 \times 10^6$	94
39.	Comparison with Laminar Theory	95
40.	Recovery Factor, Model C-1	96
41.	Pre-separation Pitot Trace	97
42.	Post-reattachment Pitot Trace	98
43.	Post-reattachment Pitot Trace	99
44.	Post-reattachment Pitot Trace	100
45.	Comparison with Laminar Theory	101
46.	Comparison with Laminar Theory	102
47.	Comparison with Laminar Theory	103
48.	Comparison with Laminar Theory	104
49.	Comparison with Laminar Theory	105
50.	Reynolds Number Dependence of Transitional Interactions	106
51.	Boundary Layer Thickness Definition	107
52.	Fluctuation Measurements	108
53.	Maximum Fluctuation Signal	109
54.	Comparison with Laminar Theory	110
55.	Comparison with Laminar Theory	111

NUMBER		PAGE
56.	Comparison with Laminar Theory	112
57.	Model Correlation	113
58.	Model Correlation	114
59.	Model Correlation	115
60.	Schematic of Model AR-1, -2 Locations in JPL SWT	116
61.	Reynolds Number Correlation	117
62.	Sensitivity of Model Location	118
63.	Free Interaction Step-ramp Comparison	119
64.	Typical Ramp Configuration Pressure Dis- tribution (Adiabatic Wall)	120
65.	Typical Step Configuration Pressure Dis- tribution (Adiabatic Wall)	121
66.	Chapman Correlation (Adiabatic Wall)	122
67.	Chapman Correlation Dependence on $\chi_o$	123
68.	Chapman Correlation (Cold Wall)	124
69.	Curle Correlation	125
70.	Curle Correlation Dependence on $\chi_o$	126
71.	Reynolds Number Correction	127
72.	Explicit Subsonic Mach Number Prediction with Viscous Correction	128

## LIST OF SYMBOLS

AR	aspect ratio (= width/chord)
$C_f$	skin friction coefficient $\left( = \frac{\tau_w}{\frac{1}{2} \rho_\infty u_\infty^2} \right)$
$C_p$	pressure coefficient $\left( = \frac{P - P_\infty}{\frac{1}{2} \rho_\infty u_\infty^2} \right)$
$C_\mu$	coefficient of viscous effect on Pitot pressure $\left( = \frac{p_t - p_t(\text{ideal})}{\frac{1}{2} \rho_u u^2} \right)$
$C_\infty$	Chapman-Rubesin factor $\left( = \frac{\mu_w}{\mu_\infty} \frac{T_\infty}{T_w} \right)$
h	height of tip of Pitot probe or step height
H	form factor $\left( = \frac{\theta_i}{\delta_i^*} \right)$
i	current
$l_i$	characteristic length of free interaction
M	Mach number
p	pressure
$p_o$ or $p_{e0}$	pressure at reference point near the beginning of the separation interaction
$p_{o\infty}$	free stream total pressure
$p_{t2}$	Pitot pressure
$p_\infty^+$	final downstream wedge pressure
$p_\infty^-$	free stream pressure
P	non-dimensional pressure in free interaction
r	recovery factor or distance from centerline of axisymmetric "stovepipe" model
R	hot wire resistance
$R_N$	radius of "stovepipe" model
Re	Reynolds number

## LIST OF SYMBOLS (Cont'd)

$Re_{\infty}$	free stream unit Reynolds number (per inch)
$Re_h$	Reynolds number based on height of Pitot probe
$Re_{x_c}$	Reynolds number based on chord length of model
s	length along the ramp from corner of the model
t	thickness of leading edge of flat plate
T	temperature
$T_w$	wall temperature
$T_{\infty}$	free stream total temperature
u	velocity
w	model width
x	distance along plate from leading edge
$X_c$	distance from leading edge to corner or beginning of ramp
X	non-dimensional distance in free interaction
y	distance from model surface
V	hot wire voltage
$\overline{\Delta V^2}$	mean square voltage fluctuation for whole frequency range of 1 KC to 320 KC
$\alpha$	ramp angle
$\gamma$	ratio of specific heats $\left( = \frac{C_p}{C_v} \right)$
$\delta$	boundary layer thickness
$\delta^*$	displacement thickness $\left( = \int_0^{\delta} \left( 1 - \frac{\rho u}{\rho_e u_e} \right) dy \right)$
$\Delta$	distance from surface of "stovepipe" model
e	error in Pitot probe location
$\theta$	angle of deflection of streamlines at edge of boundary layer or momentum thickness $\left( = \int_0^{\delta} \frac{\rho u}{\rho_e u_e} \left( 1 - \frac{u}{u_e} \right) dy \right)$

## LIST OF SYMBOLS (Cont'd)

$\Theta$	non-dimensional angle in free interaction
$\mu$	viscosity
$\rho$	density
$\tau$	shear
$\chi$	Hypersonic viscous interaction parameter

Subscripts

$( )_c$	corner
$( )_i$	incompressible
$( )_o$	reference point near beginning of separation interaction
$( )_w$	model surface
$( )_\infty$	free stream
$( )_{\infty^-}$	free stream
$( )_{\infty^+}$	downstream wedge

Superscripts

$( )^{(o)}$	first term of the expression in a small parameter
$\overline{(\ )}$	mean value of a fluctuating quantity

## 1. INTRODUCTION

When a boundary layer encounters a region of increasing pressure, it may under certain conditions, "separate". The fluid near the wall decelerates and is actually reversed, forcing the boundary layer to leave or "separate" from the wall. At supersonic speeds, the pressure disturbance may come in the form of an incident shock wave or a compression corner. The objective of the present experimental investigation was to measure the effect of cooling on the separation and reattachment of a boundary layer at hypersonic speeds. If one is to gain understanding into this very complicated problem, it is necessary to eliminate as many unknowns and secondary parameters as possible, clearly identifying those remaining, in order that one can ascribe the observed effects to the main parameters. It was felt that this objective could be best accomplished by observing the flow separation of a well defined boundary layer on a body of fixed geometry, both with and without cooling. Many experiments have been made of the phenomenon of boundary layer separation at supersonic and even hypersonic speeds for adiabatic models [Chapman, Kuehn and Larson (1), Gadd (2), Hakkinen, et al (3), and Sterrett and Emery (4), to mention just a few]. However, to the author's knowledge, all experiments involving highly cooled walls have been performed in transient facilities, e.g. the works of Bogdonoff and Vas (5), Miller, et al (6) and more recently Needham (7), which preclude any observation of an adiabatic mode.

Two commonly used idealizations in theoretical analyses, as for example the integral or moment solutions of Lees and Reeves (8),

are two-dimensionality and purely laminar flow. Clearly, an experimental work which is amenable to analysis is of far more value than one that is too complex to allow analysis. With these goals in mind the first objective of this investigation was to establish the conditions under which an experiment satisfied the previously mentioned constraints, and then to observe the effect of cooling.

A geometry consisting of a flat plate with a sharp leading edge allowed for the formation of a boundary layer well defined by the experimental work of Kendall (9) and the theoretical work of Lees and Probstein (10) and others. The boundary layer was then separated by a fixed angle ramp placed at a distance far enough from the leading edge of the plate as to insure the separation occurring in a region of otherwise weak interaction.

The finite span model which the experimentalist must accept will not in general conform to the criteria of two-dimensionality because of outflow and/or interaction with wind tunnel boundary layers. One can eliminate these effects by mounting side plates on the model large enough to contain the entire separation interaction (inviscid external flow as well as separation bubble) and then determining and minimizing (if possible eliminating) the disturbances caused by the side plates themselves. The disturbances caused by the side plates were determined by measuring their effect on an otherwise perfect flow which approximated the two-dimensional phenomenon; an axisymmetric "stovepipe"-flare in the JPL supersonic wind tunnel.

During the present study the Reynolds numbers encountered on the plate insure the existence of laminar flow preceding separation

for both adiabatic and cold wall configurations at  $M_\infty = 6$ . However, separated layers undergo transition at much lower Reynolds numbers than do attached boundary layers, so it is necessary to confirm that the flow remains laminar throughout reattachment. Since the characteristics of the mean flow of a turbulent boundary layer are quite distinct from the laminar case, it is possible to ascertain whether the flow undergoes transition by surveying the boundary layer at a station "far downstream" of reattachment.

Reeves (11) has pointed out the similarity between the shock wave-boundary layer interaction and the compression corner for small angles. The experimental pressure distribution of the adiabatic flow separation associated with a compression corner can be compared to the prediction of the Lees-Reeves theory for an equivalent shock wave-boundary layer interaction ( $Re_{x_{corner}} = Re_{x_{shock}}$  and  $p_\infty + \frac{1}{2}\rho U^2$  identical). A comparison of transitional interactions with the laminar theory will allow one to infer the effects of transition.

The "free interaction" similarity suggested by Chapman (1) for the flow upstream of the separation inducing disturbance is empirically tested and found to be a good approximation for the adiabatic configuration but fails to correlate the cooled case to the adiabatic case. The scaling suggested by Curle (12) is tested and found to eliminate this deficiency and finally, this scaling is examined on the basis of the Lees-Reeves formulation and the approximations necessary to obtain similarity are clarified.



## 2. EXPERIMENTAL APPARATUS

### 2.1. Wind Tunnels and Free Stream Conditions

The experiments reported here were conducted in two continuous flow wind tunnels:

- (a) The Jet Propulsion Laboratory's 18" × 20" Supersonic Wind Tunnel at a nominal Mach number of 4.00 (with some additional measurements at Mach 5.00).
- (b) The GALCIT 5" × 5" Hypersonic Wind Tunnel at a nominal Mach number of 6.06.

The unit Reynolds number  $\frac{\rho_{\infty} u_{\infty}}{\mu_{\infty}}$ , was varied by changing the stagnation pressure, keeping the stagnation temperature approximately constant: at JPL ( $M_{\infty} = 4.00$ ),  $33,000 \leq Re_{\infty}/\text{inch} \leq 300,000$ ,  $68,000 \leq Re_{x_c} \leq 894,000$ ; at GALCIT ( $M_{\infty} = 6.06$ ),  $60,000 \leq Re_{\infty}/\text{inch} \leq 200,000$ ,  $150,000 \leq Re_{x_c} \leq 1,000,000$ .

### 2.2. Models and Surface Instrumentation

#### 2.2.1. Models Tested in JPL Supersonic Wind Tunnel

Model AR-1 (Figures 1,2) is an annular stovepipe flare consisting of a 3 inch long plate with a sharp ( $t \leq .003''$ ) leading edge, wrapped around a 10 inch diameter, followed by a 4 inch long  $10^{\circ}$  flare. The model was sting mounted and the internal diameter was large enough to allow internal supersonic flow. The model was made of stainless steel and instrumented with 30 static pressure orifices .012 inches in diameter, located in a single radial plane but never less than .125 inch (approximately 10 diameters) apart.

Model AR-2 (Figures 1,2) is a flat duplicate of AR-1 consisting of a 3 inch long plate with sharp ( $t \leq .003''$ ) leading edge followed

by a 4 inch long,  $10^\circ$  ramp. The model is 18 inches wide and spanned the JPL tunnel. It was supported on each side and rubber O-ring type seals were used to prevent outflow. The pressure instrumentation was identical to that of AR-1.

Both models were fitted with side plates or fins swept to an angle of  $15^\circ$ ; the leading edges of these plates or fins were sharp. The fins were bonded to the models with Eccobond which insured a seal and allowed for easy removal (Figure 2).

The surface pressures were measured with a multiple pressure measuring system designed by J. M. Kendall, Sr. (13). The device consists of a minimum volume (to reduce response time) pressure transducer which is mechanically moved from one pressure lead to the next and is capable of handling over 100 such measurements. One calibration point was checked against the reading on a mercury manometer for each run.

Schlieren and Spark-Shadowgraph photos were taken of AR-1 for all conditions.

#### 2.2.2. Models Tested in GALCIT Mach 6 Wind Tunnel

Model C-1 (Figures 3, 4) is a model made of nondeforming tool steel (Ketos), consisting of a 2.50 inch plate with a sharp ( $t \leq .003''$ ) leading edge followed by a  $10.25^\circ$ , 3.0 inch long ramp. The model is 5 inches wide and spanned the GALCIT tunnel. It is hollow and capable of allowing the internal flow of liquid nitrogen ( $T \sim -320^\circ\text{F}$ ). It is instrumented with 22 static pressure orifices along its centerline and 6 copper-constantan thermocouples. The pressures were recorded on a multiple tube silicone manometer

board and the repeatability of these measurements for both the adiabatic and cold wall configurations is shown in Figure 5. The thermocouple output was measured on a Fairchild DVM after it was found to give readings to within a few percent of those made with a Leeds-Northrup K-2 potentiometer. The operation of the DVM required much less time and effort. The calibration data given in the Leeds-Northrup handbook taken from the National Bureau of Standards circular 561 for a copper-constantan thermocouple were used; the calibration was checked at 3 points (Figure 6). A schematic of the  $\text{LN}_2$  pumping system, which was designed by R. Batt\* for his studies of wakes of highly cooled bodies, is shown in Figure 7.

Models X-1, 3 and 4 (Figure 8) are of a similar cross-sectional geometry: a flat plate with sharp ( $t \leq .003''$ ) leading edge followed by a  $10^\circ$  ramp at a fixed distance from the leading edge of the plate. All the models spanned the 5 inch wide GALCIT tunnel and the distances from the leading edge of the plate to the beginning of the ramp are respectively 5, 3 and 2 inches; the ramp lengths 5.5, 5 and 4 inches. The models were instrumented with surface pressure orifices and the pressures were measured on a silicone manometer.

Model S-1 (Figure 9) is a flat plate instrumented with surface pressure orifices which allowed for the positioning of steps of various heights at several stations. This model was utilized to obtain more extensive separated flows for the free interaction

---

\* Graduate Student, California Institute of Technology

study.

### 2.3. Probe Measurements

#### 2.3.1. Pitot Measurements

A Pitot probe with a flattened (.003"  $\times$  .05") tip was used for the boundary layer and external flow surveys. The pressures were measured on a Statham 5 psia pressure transducer which was calibrated before and after the test program. The measurements were recorded on a Moseley autograph and the position of the probe was indicated by a helipot connected to the actuating mechanism of the tunnel. For each trace, the probe was positioned with respect to the model by electrical contact, the model being insulated from the probe until there was contact with the probe tip.

#### 2.3.2. Fluctuation Measurements

The hot-wire probe consisted of two needle tips, attached to a brass holder designed by C. F. Dewey, Jr. (14) to which a hot wire was soft soldered. The wires were platinum-10% rhodium, .0001 inch in diameter and had an aspect ratio of approximately 100. The measurements presented were made with a single wire so that qualitative comparisons could be made without regard for the characteristics of the wire itself. A Shapiro-Edwards Model 50B constant-current hot-wire set was utilized to convert the voltage fluctuation across the hot wire caused by flow fluctuations into a D.C. output which is proportional to the mean square voltage fluctuation.

The hot wire was placed at the edge of the boundary layer, the time constant measured and the time lag compensated for at an

overheat corresponding to a 10% increase in the wire resistance. The probe was then transversed across the boundary layer at this constant current and the output,  $\overline{\Delta V^2}$ , recorded on a Moseley autograph as a function of position. For the hot-wire measurements, the probe was positioned visually with respect to the model, with a few mils allowed for clearance to prevent wire breakage.

#### 2.4. Data Reduction

Tunnel free Pitot surveys were made of both the JPL SWT and the GALCIT Mach 6 wind tunnels under the operating conditions encountered in the model tests. The local static pressure was then calculated by assuming the flow to expand isentropically from the stagnation conditions. The measured surface pressures were then normalized by using the local tunnel free static pressure as  $p_\infty$ .

The Pitot measurements in the subsonic region of adiabatic wall boundary layers were corrected for Reynolds number effects (Appendix 1).

### 3. TWO-DIMENSIONALITY

#### 3.1. Definition and Approach

The purpose of this investigation was to observe the effect of cooling on the separation and reattachment of a laminar boundary layer at hypersonic speed. In order to study the effect of cooling alone, it is necessary to eliminate as many other parameters as possible. A two-dimensional geometry consisting of a flat plate and a compression corner formed by a ramp of infinite extent was chosen as the basic idealized configuration for this study (Figure 10). Unfortunately, the two infinite lengths required for this idealization do not conform to the constraints of our experimental facility. However, the finite extent of the ramp should not appreciably affect the interaction provided that the ramp terminates many boundary layer thicknesses aft of the reattachment region. By limiting the angle of the ramp to small values, the ramp can be made long enough to satisfy this criterion and yet not exceed the maximum permissible blockage of the tunnel.

The constraint of two-dimensionality is more difficult. The cross-section of the GALCIT Mach 6 tunnel is about 5 inches  $\times$  5 inches with approximately 1 inch boundary layers, leaving a uniform core of about 3 inches  $\times$  3 inches (somewhat less than  $\infty \times \infty$ !). Thus, out-flow and other interactions with the tunnel boundary layers must be considered. In order to eliminate these effects, side plates large enough to contain the entire separation interaction, including the inviscid external field as well as the separation bubble, were mounted on the model (Figure 11). This configuration effectively isolates the

interaction with the tunnel boundary layers, but now the disturbances from the side plates themselves must be quantitatively determined. By choosing side plates with sharp leading edges swept at an angle slightly larger than the angle of a local Mach wave (just large enough to contain the separation shock), the disturbance should be minimized. For large enough aspect ratios the flow at the centerline of the model should approach the two-dimensional phenomenon.

### 3.2. Preliminary Measurements

Figure 12 shows the actual external flow field of an adiabatic model with side plates, including off-center measurements at a station far aft of reattachment. Within experimental variation, the boundary layer edge and shock locations are independent of the spanwise location over the center 2 inches of the model (this distance corresponds to about 20 boundary layer thicknesses). Since the boundary layer thickness and the length of the separated region decrease with cooling, the adiabatic configuration is believed to require the largest aspect ratio ( $AR = w/x_c$ ) for a given configuration and flow conditions. Hence, the study of two-dimensionality will be restricted to adiabatic models.

The behavior of the centerline pressure distribution when the aspect ratio is varied by placing the side plates at various spanwise locations is shown in Figure 13. It appears that a limit is being approached as the aspect ratio is increased. However, because of the relatively small range of aspect ratio available there remains some question as to whether a limit has been attained. Furthermore, it is not obvious that the "limit" attained is not

dominated by some end effect, so that the flow does not really correspond to the infinite aspect ratio configuration. The model was instrumented also with pressure orifices over the center 2 inches in the spanwise direction at several stations. No perceptible spanwise variation was observed for any of the aspect ratios, except for the orifices immediately adjacent to the side plates, although the centerline distribution is changing with aspect ratio. This observation points up the interesting fact that although spanwise uniformity is a necessary condition for two-dimensionality, it is by no means sufficient.

Removing the side plates entirely resulted in very little difference to the reattachment region, but appears to have almost collapsed the separated region (Figure 14).

### 3.3. JPL Aspect Ratio Study

Although some insight into the problem was gained by these preliminary experiments, no evidence was found that would conclusively support the premise of two-dimensionality. In order to supply such evidence, a series of tests was performed in the JPL 20 inch Supersonic Wind Tunnel. Two models were constructed for this test; AR-1, a "two-dimensional" model consisting of a flat plate with sharp leading edge followed by a  $10^\circ$  ramp beginning 3 inches from the leading edge of the plate, the model spanning the 18 inch wide tunnel; AR-2, an open-end cylinder with flare — "stove-pipe" — with the identical cross section of the two-dimensional model. The diameter of 10 inches for the cylinder was chosen large enough to allow internal supersonic flow and keep the parameter  $\frac{\Delta}{R_N} \leq \frac{1}{10}$



( $r = R_N + \Delta$ ). In the limit as  $\frac{\Delta}{R_N} \rightarrow 0$  this configuration corresponds exactly to the two-dimensional configuration.

First the "stovepipe" was fitted with fins at various aspect ratios. This configuration approximates the two-dimensional phenomenon and there are no end effects. Thus the disturbances caused solely by the side plates to an otherwise "perfect" flow which approximates the idealized flow can be determined, at least in regard to their effect on the centerline surface pressure distribution. The results of this test for a typical interaction at  $M_\infty = 4.0$  are shown in Figure 15. Under these conditions ( $M_\infty$ ,  $Re_{x_c}$ , etc.) one cannot distinguish the surface pressure distribution from the "clean" configuration for  $AR \geq 1$ . It is concluded that the disturbance caused by the fins can be neglected.

Secondly, the "two-dimensional" model was also tested with varying aspect ratios under identical freestream conditions. Again a limit was approached for  $AR \geq 1$ . Furthermore, for the case shown (Figure 16) this limit corresponds closely to the pressure distribution attained on the stovepipe, up to a location approximately 2 inches along the flare, where the effect of the axisymmetric configuration begins to become important and the static pressure approaches the cone value instead of that of the wedge.

By using fins similar to those indicated in Figure 11 and by systematically varying the aspect ratio under the operating conditions to be encountered, it is concluded that: (1) a limit will be reached at moderate aspect ratio; (2) this limit truly corresponds to the two-dimensional phenomenon.

### 3.4. Reynolds Number Correlation

As an additional verification that this limit had been obtained in the GALCIT Mach 6 tunnel, a Reynolds number correlation was made with three geometrically similar adiabatic models (flat plate with sharp leading edge, followed by a  $10^\circ$  ramp) with different chord lengths and unit Reynolds numbers. Each model had a different aspect ratio and a different ratio of ramp length to chord length (Figure 17). Since the chord length was taken to be the only characteristic length in this correlation the results obtained appear to confirm: (1) the supposition that the termination of the ramp in no appreciable way affected the interaction (length of ramp/length of plate varied from 1.0 to 1.5); and (2) the two-dimensional limit had been attained. It should be emphasized that the necessary ramp length and aspect ratio will of course vary with flow conditions, extent of separation, etc.

Finally, it should be noted that all of these conclusions were drawn from interactions believed to be purely laminar. Transitional interactions and their correlations will be discussed later.

#### 4. PURELY LAMINAR FLOW WITH AND WITHOUT COOLING

##### 4.1. Confirmation of Laminar Flow

The Reynolds numbers encountered on the plate of Model C-1 insure the existence of laminar flow preceding separation for both adiabatic and cold wall conditions at  $M_\infty = 6$ . However separated flows are known to undergo transition earlier than attached flows, so it was necessary to confirm that the flow remained laminar throughout the reattachment region by a direct measurement. In this section the experimentally measured pre-separation and post-reattachment Mach number profiles are presented for a series of tunnel supply pressures, or Reynolds numbers,  $Re_{x_c}$ , for both the adiabatic and cold wall condition. Once the range of  $Re_{x_c}$  for the purely laminar interaction is established, the main features of the interaction can be compared with the theoretical calculations of Lees-Reeves ( 8 ) as modified by Klineberg and Lees ( 15 ).

Since the characteristics of the mean flow of a turbulent boundary layer are quite distinct from the laminar case, one can ascertain if the flow undergoes transition by surveying the boundary layer at a station far downstream of reattachment. If the flow remains laminar, the boundary layer will approach a self-similar, zero pressure gradient laminar profile which can be theoretically predicted. The predictions are limited to this asymptotic downstream profile. However, any experimental profile which exhibits a "fuller" distribution than the asymptotic prediction has been distorted beyond what would have occurred if the flow had remained purely laminar.

#### 4.1.1. Adiabatic Model (C-1)

When no internal flow was allowed, the temperature of the model surface at a station 1 inch from the leading edge, which is upstream of separation, varied between  $636^{\circ}\text{R}$  and  $645^{\circ}\text{R}$ , or within 2 percent of the temperature predicted for an adiabatic plate at Mach 6. The temperature of the model aft of separation is discussed in the following section.

Pitot surveys were made upstream of separation and compared to a theoretical prediction (16) assuming zero pressure gradient and using the Sutherland viscosity law (Figures 18,19). The agreement is found to be reasonably good down to  $M \sim 1$ , below which the experimental measurements indicate a higher Mach number than is theoretically predicted. When the probe is farther than  $\sim 3h$  from the plate, the difference is attributed to viscous effects and a correction of the form  $C_{\mu} = \frac{2.2}{\text{Re}_h}$  (Appendix 1) has been applied to all adiabatic profiles.

The Mach number distributions obtained throughout the re-attachment region for the adiabatic configuration at  $\text{Re}_{x_c} = .15 \times 10^6$  ( $p_{\infty} = 30 \text{ psia}$ ) are shown in Figure 20 together with the theoretical estimate of the laminar asymptotic profile. Included in Figure 20 is the surface pressure distribution in this region showing the corresponding locations at which the profiles were taken. Choosing station 5.0 as a "test station", the profiles obtained at higher Reynolds numbers are shown in Figure 21, and the distortion beyond the predicted asymptotic profile is interpreted as the appearance of transition.

#### 4.1.2 Cold Model (C-1)

As previously indicated, the model was designed to allow the internal flow of a liquid coolant. When liquid nitrogen was used in conjunction with the flow system designed by R. Batt, a uniform model temperature of  $-310^{\circ}\text{F} \pm 5^{\circ}$  was obtained, with the possible exception of the leading edge of the flat plate. After a few minutes run time a light frost, only a few mils thick, was formed over the entire surface of the model, with the exception of a region extending aft  $\sim 1/4$  inch from the leading edge, indicating in all probability a "hot" leading edge. The thermocouple nearest to the leading edge at  $x = 1$  inch indicated the uniform temperature, and since separation did not occur until about twenty boundary layer thicknesses aft of this station, it was assumed that this non-uniformity did not appreciably affect the interaction.

The Pitot surveys of the cold model were subject to a typical positioning error of approximately .003 inch. This error may have been caused by the operational procedure followed for the "cold" configuration. The Pitot probe was positioned by an electrical contact with the surface of the model. It was then moved away from the surface into the external flow, where it remained while the model was brought to uniform temperature, after which the survey was carried out. The entire process took approximately 10 to 15 minutes. It was not possible to check the position of the probe at the end of the run because the light frost did not allow the electrical contact to be made. The positioning error might also be caused by a change in the effective location of the wall when the frost layer is present.

The positioning error, though small in absolute magnitude, leads to an appreciable relative error in the boundary layer. For example, for a typical condition

$$\begin{aligned} \epsilon &= \pm .003 \\ \delta &= .050 \\ \text{at } \frac{y}{\delta} &= .50 \end{aligned} \qquad \begin{aligned} \frac{y}{\delta} &= \frac{y}{\delta} (1 \pm \frac{\epsilon}{y}) \\ (\frac{y}{\delta})_{\text{measured}} &= .45 \rightarrow .55 \end{aligned}$$

The detection of possible distortion of the velocity profile is limited by this "spread." The preseparation profiles for the cold wall configuration are shown in Figure 22. The spread in the data is of the order expected from the positioning error. However, all cases fall below the theoretical prediction (Figure 23), which might tend to support the idea that the frost formation caused a change in the "effective" location of the wall. The effect of cooling causes the subsonic region to lie almost entirely within 4 probe heights of the surface, and no Reynolds number correction has been attempted for this case.

The Mach number distributions downstream of reattachment at  $Re_{x_c} = .15 \times 10^6$  are repeated for the cold wall configuration and again contrasted with the predicted asymptotic profile (Figure 24). Because of the scale reduction which occurs during cooling, the pressure gradient has nearly vanished by station 4.0 and this station is chosen as a "test station." For this configuration no obvious distortions exist (Figure 25) until  $Re_{x_c} = .50 \times 10^6$  ( $p_{o\infty} = 100$  psia), and it is assumed that below this Reynolds number the interaction is effectively laminar.

It must be emphasized that the length of the separated region has been greatly reduced in the cold wall configuration (by approximately a factor of 3) and hence the overall effect of stabilization does not support any conclusion as to the stabilizing effect of cooling when applied to either boundary layers or free shear layers.

## 4.2 Laminar Flow

### 4.2.1. Experimental Correlations

#### 4.2.1.1. Effect of Cooling

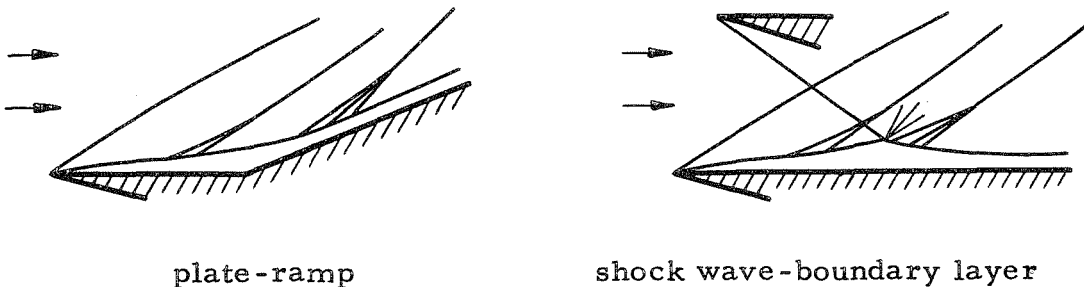
For one condition the flow was judged laminar for both the adiabatic and the cold wall cases ( $Re_{x_c} = .15 \times 10^6$ ). The boundary layer edge and the shock waves in the external flow for each case are shown in Figures 26 and 27. The effect of cooling on the surface pressure distribution of a laminar, two-dimensional, complete (in the sense of an infinite ramp) boundary layer separation for a fixed geometry,  $Re_{x_c}$  and  $M_\infty$  is shown in Figure 28. In order to eliminate two obvious effects of the reduction of the initial pressure level (viscous interaction) and the reduction of the boundary layer thickness and thereby bring out the additional effects of cooling a new pressure parameter is defined,  $\frac{p-p_o}{p_o^+ - p_o}$  and plotted versus a coordinate scaled by a characteristic thickness associated with an undisturbed plate boundary layer, holding the corner fixed,  $\xi \propto \frac{x-x_c}{\delta_c^*}$ . The data (Figure 29) show a remarkable similarity when viewed in this light; the cold wall case exhibits less upstream influence than the adiabatic case, but the two are almost identical throughout the reattachment region. (See later discussion of "free interaction" scaling.)

#### 4.2.1.2. Effect of Reynolds Number

Unfortunately the appearance of transition at higher Reynolds numbers for the adiabatic model rules out any observation of the effect of Reynolds number on the purely laminar interaction for this case. However, over a limited range of Reynolds numbers the flow was judged laminar for the cold wall model and for a fixed  $M_\infty$ ,  $\frac{T_w}{T_\infty}$  and geometry ( $\frac{p_{\infty+}}{p_{\infty-}} = 3.81$ ), Figure 30 shows the effect of Reynolds number. The most striking feature is the upstream propagation of separation with increasing  $Re_{x_c}$ , which is in agreement with the trend predicted for the adiabatic case by the Lees-Reeves theory, and that observed experimentally by Needham (7).

#### 4.2.2. Comparison with Lees-Reeves Theory

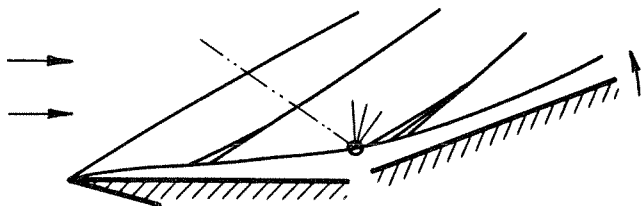
Similarity between the separation associated with a compression corner and that of an incident shock wave-boundary layer interaction was noticed by Reeves (11).



If the strength of the shock in the shock wave-boundary layer interaction is small enough so that the entropy loss can be neglected, we see that within a small displacement the geometry of the boundary layer is quite similar to that of the plate ramp configuration,



provided the overall pressure rise is matched.



A comparison of the experimental pressure distribution of the laminar interaction on the adiabatic plate-ramp to the theoretical prediction for an equivalent shock wave-boundary layer interaction ( $Re_{x_{corner}} = Re_{x_{shock}}$  and  $p_{\infty}^+/p_{\infty}^-$  identical) is shown in Figure 31.

In addition the form factor  $H = \theta_i/\delta_i^*$ ,

where

$$\theta_i = \int_0^{\delta_i} \frac{u}{u_e} \left(1 - \frac{u}{u_e}\right) dY, \quad \delta_i^* = \int_0^{\delta_i} \left(1 - \frac{u}{u_e}\right) dY, \quad \rho dY = \rho_e dy$$

has been calculated from the experimental Mach number distributions by approximating the temperature field by

$$\frac{T}{T_e} = \frac{1 + r \frac{\gamma-1}{2} M_e^2}{1 + r \frac{\gamma-1}{2} M^2}, \quad r = .845$$

and the variation of this parameter is also compared to the theory in Figure 32. During the aspect ratio study at JPL, at  $M_{\infty} = 4.0$  we had a visual (shadowgraph) indication that flow may have remained laminar below  $Re_{x_c} = .17 \times 10^6$  and these pressure distributions, including those obtained on the stovepipe configuration (AR-1) which approximated the two-dimensional flow, are shown in Figures 33, 34, 35. Finally the condition at which we obtained Reynolds number

correlation at  $M_\infty = 6.06$  ( $\alpha = 10^\circ$ ) is included (Figure 36). In all these cases the moment method of Lees and Reeves gives a satisfactory description of the surface pressure distribution throughout the interaction region. The discrepancy between the experiment and the theory at  $M_\infty = 6.06$  and  $Re_{x_c} = .15 \times 10^6$  (Figure 31) is believed to be due to improper initial conditions utilized in the theoretical analysis. The initial viscous interaction ( $\chi_o \simeq .75$ ) makes the assumption of Blasius initial conditions suspect and this, including the details of the corner problem, is presently being considered by D. Ko\* at Caltech.

---

\* Graduate Student, California Institute of Technology

## 5. TRANSITION

### 5.1. Observations of Transition and its Effect

In order to ascertain the effect of transition, and in particular its effect on the surface pressure distribution, interactions known to be transitional have been contrasted with the theoretical prediction for the laminar shock wave-boundary layer interaction. Within the limitations of this theoretical prediction for the laminar flow, such a comparison will show the effect of transition.

The shadowgraphs taken of Model AR-1 at JPL during the aspect ratio study show evidence of turbulence aft of reattachment for  $Re_{x_c} \geq .27 \times 10^6$  at  $M_\infty = 4.0$  (Figure 37). A qualitative change occurs in the characteristics of the boundary layer in the region aft of reattachment, as compared to the boundary layer forward of separation. The boundary layer upstream of reattachment, including the separated layer, exhibits a distinct edge. This edge vanishes in the region aft of reattachment. Also, a structure becomes plainly visible, beginning with striations at the lower Reynolds numbers and becoming "grainlike" at the higher Reynolds numbers (Figure 38). It would seem plausible that the striations are caused by a vortex-like structure and the grains are turbulent eddies. The surface pressure distributions for both Models AR-1 and -2 are contrasted with the laminar theory for  $Re_{x_c} = .27 \times 10^6$  (Figure 39). For this Mach number and ramp angle, the next highest Reynolds number exceeds the limitations placed on the theory by the one parameter description; for higher Reynolds numbers (more highly separated flows) the appearance of a predicted static pressure maximum in

the "free interaction" region is deemed physically unrealistic (8).

The surface temperature of the GALCIT model C-1 was recorded for the adiabatic configuration (in which no internal flow was permitted) and the local recovery factor was calculated; the results are shown in Figure 40. The pre-separation ( $x = 1$  inch) recovery factor increases from  $r = .845$  to  $.859$  as the unit Reynolds number is increased. This deviation is believed to be caused by heat conduction within the model, which extends into the tunnel boundary layers (turbulent for  $p_{\infty} > 40$  psia). The post-reattachment ( $s = 1.46$ ) value of  $r$  shows an increase with increasing unit Reynolds number, and it approaches a value exceeding the expected turbulent recovery factor by about the same amount as the plate value exceeds the laminar prediction. This behavior is associated with the transitional nature of the boundary layer in addition to heat conduction within the model.

The Pitot surveys in the reattachment region for the higher Reynolds numbers exhibit the characteristic properties of transitional or turbulent boundary layers. The edge becomes poorly defined and the profile becomes increasingly full. A region near the wall appears in which the profile is similar to the laminar boundary layer profiles, and this region is believed to be the laminar sublayer of a turbulent boundary layer. This qualitative change in the Pitot surveys is seen in Figures 41, 42, 43, 44, which include a pre-separation laminar profile for comparison.

All the pressure distributions, including that of the laminar case for comparison, are shown with the laminar theoretical

prediction. The Mach number distributions obtained in the reattachment regions are also included in Figures 45, 46, 47, 48, 49.

The effect of transition appears to be threefold: (1) the upstream influence has been retarded; (2) the pressure gradient in the reattachment region has steepened; and (3) the pressure overshoot (above inviscid  $p_{\infty}^+$ ) has increased.

The appearance of transition at higher Reynolds numbers for the adiabatic configuration ruled out any observation of the effect of Reynolds number on a purely laminar interaction. The cold wall configuration, which remained laminar over a limited range of Reynolds numbers, exhibited the upstream propagation of separation with increasing Reynolds number which has been predicted by Lees and Reeves. The effect of transition on upstream influence is to reverse this trend (Figure 50), a result which has also been observed by Needham (7).

## 5.2. Fluctuation Measurements (GALCIT, Model X-1, adiabatic wall, $M_{\infty} = 6.06$ )

The location of a point of transition would allow one to define a sufficient criterion for an effectively laminar interaction. The Pitot profiles exhibit a continuous variation from separation-like profiles to profiles of a transitional or turbulent nature. In order to establish whether there exists a point of transition, fluctuation measurements were made across the boundary layer at several stations and tunnel conditions (Reynolds numbers). The measurements were made using a Shapiro and Edwards constant-current hot-wire set. The sensitivity of the measurements to local conditions, which change greatly across

the boundary layer, require numerous measurements under differing conditions (e.g. wire overheat) in order that one can be certain what portion of the hot-wire voltage output is truly flow fluctuation. Such measurements were not carried out during this investigation and these measurements are necessarily of a qualitative nature. The hot wire was placed just outside the boundary layer and the time constant was determined by the square wave method at an overheat corresponding to 10% increase in the wire resistance above its adiabatic value.

With this fixed current, the hot wire was then traversed across the boundary layer and the mean square voltage output recorded on a Moseley autograph versus the position of the hot wire. The measurements represent contributions from all frequencies between 1 cycle and 300 kilocycles. Pitot surveys were taken under identical conditions and with the boundary layer thickness,  $\delta$ , defined as the maximum slope intercept (Figure 51); the mean square voltage fluctuation was then plotted versus  $y/\delta$  and is shown in Figure 52.

Well defined maxima occur within the boundary layer for stations located at or near the corner of the model for all 3 Reynolds numbers. At the lowest Reynolds number ( $p_{\infty} = 30$  psia), this behavior remains the same as one moves aft, with an increase in the magnitude of the maxima and a slight shift of the location of the maxima toward the wall. At the higher Reynolds numbers, the picture undergoes a qualitative change. The maxima are less well defined and tend to "spread out", with a marked increase in magnitude. At the highest Reynolds number,  $p_{\infty} = 100$  psia, the measurement ( $\overline{\Delta V^2}$ ) reaches a maximum and then begins to decrease as

one moves aft (Figure 53).

No criteria, such as an abrupt increase in fluctuation, were observed which would allow one to define a "point of transition" and hence a sufficient criterion for an effectively laminar interaction.

The Pitot surveys show a distinct sublayer at  $x \sim 2.0$  for  $Re_{x_c} = 1.0 \times 10^6$  and  $x \sim 3.0$  for  $Re_{x_c} = .50 \times 10^6$  (none at  $Re_{x_c} = .30 \times 10^6$ ), which, accompanied by the peaking of the fluctuation measurement at  $Re_{x_c} = 1.0 \times 10^6$ , suggests the existence of a fully developed turbulent boundary layer. The severity of the effect of this level of transition on the interaction is seen when the pressure distributions are contrasted with the laminar theory. (Figures 54, 55, 56) The deviation from the laminar prediction increases with increasing Reynolds number while simultaneously the fluctuation measurements undergo the qualitative changes previously described.

### 5.3. Model Correlations

#### 5.3.1. Two Model Correlation (JPL, Models AR-1 and 2, Adiabatic Wall, $M_\infty = 4.0$ )

The correlation between the pressure distributions of the two-dimensional and annular models used in the aspect ratio study at JPL has been demonstrated at  $Re_{x_c} = .068 \times 10^6$ . As the Reynolds number was increased this correlation becomes increasingly poor. (Figures 57, 58, 59). The only parameter ( $\frac{\Delta}{R_N}$ ) which governs the difference between the two models remains relatively unchanged. At the highest Reynolds numbers the stovepipe is known to be transitional (shadow-graph observation), and it is concluded that this lack of correlation is directly attributable to the degree of transition which each model

experiences. The stovepipe model is mounted approximately 2 feet aft of the two-dimensional model, and its surface is as close as 2 inches from the tunnel boundary layer (Figure 60), while the surface of the two-dimensional model is approximately 7 inches from the edge of the tunnel boundary layer. It is believed that this variation in location is subjecting the stovepipe configuration to a higher level of "noise" from the turbulent tunnel boundary layers, thereby more effectively tripping the separated flow.

### 5.3.2. Reynolds Number Correlation (GALCIT, Models X-1, 3 and 4, Adiabatic, $M_\infty = 6.60$ )

As previously shown, a good correlation of surface pressure distributions was obtained with different size models when free stream conditions (unit Reynolds numbers) were adjusted such that  $Re_{x_c}$  was invariant (see Figure 17). For  $Re_{x_c} > .30 \times 10^6$ , where the flow was in a state of transition, this correlation failed (Figure 61). When a given model (X-3) was moved approximately 9 inches aft in the wind tunnel it exhibited a different pressure distribution (Figure 62) thereby confirming the sensitivity of model location to the phenomenon of transition. Behrens (17) has made fluctuation measurements in the GALCIT Mach 6 tunnel which show an increase in the free stream fluctuation ( $\overline{\Delta V^2}$ ) of approximately a factor of 3 (1 cycle/sec to 20 kilocycle/sec) over this distance.

The apparent sensitivity to model location within a given tunnel, and to tunnel conditions (unit Reynolds number, etc.) and/or model size makes it impossible to ascribe a critical Reynolds number to the transition phenomenon in a separation interaction in wind



tunnels. One must have the capability to run a tunnel with laminar tunnel boundary layers so that there would be no "noise," and then vary Reynolds numbers by changing model size in order to arrive at a criterion which would be of value under flight conditions. This procedure has not been attempted during this investigation because of the limitations of the existing experimental facilities.

## 6. FREE INTERACTION

Once a boundary layer has been separated by some disturbance (step, shock, etc.), the flow field in the region near separation is dominated by the equilibrium interaction between the boundary layer and the external supersonic flow. Although the location of the point of separation is very much a function of the location and strength of the disturbance, the pressure distribution throughout the region removed from the immediate neighborhood of the disturbance is governed by local interaction, and in this sense is independent of the disturbing mechanism. This phenomenon is commonly referred to as a "free interaction" (Figure 63)

Chapman et al. (1) obtain a similarity scaling by the following unrigorous but suggestive approach. Taking the linearized pressure coefficient referred to conditions at some reference point  $x_o$ ,

$$\frac{p-p_o}{\frac{\gamma}{2} p_o M_o^2} = \frac{2(\theta-\theta_o)}{\sqrt{M_o^2-1}}$$

and the momentum equation evaluated at the wall,

$$\frac{dp}{dx} = \left( \frac{\partial \tau}{\partial y} \right)_w$$

the introduction of the following dimensionless variables,

$$\xi = x-x_o = l_i X$$

$$dy = \delta_o^* d\bar{y}$$

$$\tau = \tau_o \bar{\tau}$$

$$\theta-\theta_o = \frac{\delta_o^*}{l_i} \Theta$$

where  $l_i$  is as yet undetermined, leads to

$$\frac{dP}{dX} = \left( \frac{\partial \tau}{\partial y} \right)_w \quad \text{and} \quad P = 2 \Theta$$

$$\text{provided } P = \frac{p-p_o}{\tau_o} \frac{\delta_o^*}{\ell_i} \quad \text{and} \quad \left( \frac{\delta_o^*}{\ell_i} \right)^2 = \frac{\tau_o}{\frac{\gamma}{2} p_o M_o^2} \sqrt{M_o^2 - 1};$$

$$\text{that is } P = \frac{C_{p_o} (M_o^2 - 1)^{\frac{1}{4}}}{\gamma C_{f_o}} \quad \text{and} \quad X = \frac{x-x_o}{\delta_o^*} \gamma C_{f_o} (M_o^2 - 1)^{\frac{1}{4}}$$

In hypersonic flows, the linearized representation of the pressure coefficient is of limited use and for our purposes it will be necessary to include the next term, that is

$$\frac{p-p_o}{p_o} = \gamma M_o \Delta \theta \left\{ 1 + \frac{\gamma+1}{4} M_o \Delta \theta + \dots \right\} \quad M_o^2 \gg 1, \quad M_o \Delta \theta \ll 1$$

The similarity form now becomes

$$P = 2 \Theta \left\{ 1 + \frac{\gamma+1}{4} M_o^{3/2} \gamma C_{f_o} \Theta \right\}$$

Hence, even from this crude argument a parameter has arisen which cannot be eliminated and in general we must expect  $P$  to depend on this parameter as well as on  $X$ , i.e.,  $P = P(X; M_o^{3/2} \gamma C_{f_o})$ .

Since the experimental measurements were limited to  $p = p(x)$ , it was necessary to predict the initial scaling parameters. Restricting the argument to the separation of a boundary layer formed on a flat plate, in a moderately hypersonic flow ( $M_o^2 \gg 1$ ) and occurring in the weak interaction regime of the boundary layer,  $M_o \left( \frac{d\delta^*}{dx} \right) \ll 1$ , it can be shown (Appendix 2a) that the Chapman similarity variables become,

$$P = \frac{C_{p_o} (M_o^2 - 1)^{\frac{1}{4}}}{\sqrt{C_{f_o}}} = 1.75 \frac{p - p_o}{p_o} \frac{1}{\sqrt{\chi_o}} \left\{ 1 + O(M_\infty \frac{d\delta^*}{dx}) \right\}$$

$$X = \frac{x - x_o}{\delta_o^*} \sqrt{C_{f_o}} (M_o^2 - 1)^{\frac{1}{4}} = 0.82 \frac{x - x_o}{x_o} \frac{1}{\sqrt{\chi_o}} G^{-1}(M_\infty, \frac{T_w}{T_\infty})$$

$$\left\{ 1 + O(M_\infty \frac{d\delta^*}{dx}) \right\}$$

where  $G(M_\infty, \frac{T_w}{T_\infty}) = \frac{\delta^*}{x} \frac{\sqrt{Re_x}}{M_\infty^2 \sqrt{C_\infty}}$

is a relatively insensitive function of Mach number for the adiabatic wall and  $M_\infty \geq 4$ .

#### Adiabatic

$M_\infty = 4.00$	$G = .443 + \frac{1.730}{M_\infty^2}$	$= .551$
$= 5.00$		$= .512$
$= 6.06$		$= .472$
$\rightarrow \infty$		$\rightarrow .443$

The function G does change significantly for a cooled wall, for example :

$M_\infty = 6.06$	$\frac{T_w}{T_\infty} = 1.70$	$G = .200$
-------------------	-------------------------------	------------

(As  $M_\infty \rightarrow \infty$ ,  $\frac{T_w}{T_\infty}$  - fixed, the scaling function G becomes independent of wall temperature, corresponding to a physical scale approximately one-quarter that of the adiabatic configuration,  $G \rightarrow .116$ ).

For the flat plate boundary layer the additional parameter,  $M_o^{3/2} \sqrt{C_{f_o}}$ , which entered because of the nonlinear term in the pressure coefficient is just  $\sqrt{\chi_o}$  and  $P = P(X; \chi_o)$ .

Restricting attention at first to the adiabatic mode, the pressure distributions obtained on three models (the stovepipe -  $10^\circ$  flare at  $M_\infty = 4.0$  and  $5.0$ , a plate -  $10^\circ$  ramp and a .10 inch step placed on a plate at  $x = 3$  inches and  $x = 5$  inches at  $M_\infty = 6.06$ ) have been reduced according to this similarity scaling. In all cases transition appears to occur in the neighborhood or downstream of reattachment (Figure 38), leaving the "free interactions" laminar. Hence, the free interactions of transitional as well as purely laminar overall interactions have been correlated.

Figures 64, 65 show typical pressure distributions obtained with these configurations, and Figure 66 shows the Chapman correlation including all values of  $\chi_o$ . In order to investigate the dependence on the interaction parameter,  $\chi_o$ , the values of  $P$  occurring at each of 3 fixed values of  $X$  (obtained by curve fit) are plotted versus  $\chi_o$  (Figure 67). The variation observed amounts to approximately 10% for each value of  $X$ , and appears to be a definite trend, such that  $P$  decreases with increasing  $\chi_o$ .

The effect of wall temperature on Chapman's scaling has been assumed to enter solely through its effect on the reference quantities ( $\delta^*$ , etc.) of the scaling. The pressure distribution obtained on a plate upstream of a  $10^\circ$  ramp at  $M_\infty = 6.06$  with  $\frac{T_w}{T_\infty} \cong 1.70$  is correlated in the same manner and presented in Figure 68 together

with the band of adiabatic data. Although data taken at all Reynolds numbers for this fixed wall temperature collapse into a single curve, the curve is quite distinct from that obtained in the adiabatic case. The major difference appears to be in the X scaling which may reflect an "error" in the choice of  $\delta_o^*$  as an appropriate scaling factor for  $\theta$  and/or  $(\frac{\partial}{\partial y})_w$  when  $T_w/T_\infty$  is not fixed.

Using an approximate integral of the energy equation and a Pohlhausen type analysis, Curle (12) argues (see appendix 2b) for a flat plate that

$$C_{p_o} (M_o^2 - 1)^{\frac{1}{4}} Re_x^{\frac{1}{4}} \sim F \left\{ \frac{x - x_o}{x_o} \left( \frac{T_w}{T_e} \right)_o^{-1} (M_o^2 - 1)^{\frac{1}{4}} Re_x^{\frac{1}{4}} \right\}$$

The similarity variable P is identical to that of Chapman's scaling, but

$$X \sim \frac{x - x_o}{x_o} \frac{1}{\sqrt{\chi_o}} M_\infty^2 \left( \frac{T_w}{T_\infty} \right)^{-1}$$

The actual tabulated values of  $F(x)$  agree with Chapman's empirical values for the separation pressure, but considerably overestimate the plateau pressure. If it is assumed that the discrepancy is caused solely by the functional dependences assigned to the Pohlhausen parameter, the similarity scaling is unaffected and one is free to search for an empirical relation between the similarity variables.

Curle uses the linearized form of the pressure coefficient and by the same argument as before we can expect  $\chi_o$  to enter again as an independent parameter under the hypersonic conditions

encountered here.

As in Chapman's scaling, for adiabatic flow and relatively high Mach number,  $M_\infty^2 \left( \frac{T_w}{T_\infty} \right)^{-1}$  (which takes the place of  $G^{-1}$ ) is insensitive to Mach number.

Adiabatic wall

$$M_\infty = 4.00$$

$$= 5.00$$

$$= 6.06$$

$$\rightarrow \infty$$

$$M_\infty^2 \left( \frac{T_w}{T_\infty} \right)^{-1} = 4.32$$

$$= 4.79$$

$$= 5.10$$

$$= 5.92$$

but the effect of cooling is further magnified

e.g.  $M_\infty = 6.06$   $\frac{T_w}{T_\infty} = 1.70$

$$M_\infty^2 \left( \frac{T_w}{T_\infty} \right)^{-1} = 21.5$$

In order to compare the two scaling laws, the constant in Curle's scaling is adjusted such that it agrees with Chapman in the adiabatic, infinite Mach number limit.

As  $M_\infty \rightarrow \infty$  (adiabatic wall)

$$X_{\text{Chapman}}^{(o)} \rightarrow 1.840 \frac{x-x_o}{x_o} \frac{1}{\sqrt{\chi_o}} \equiv X_{\text{Curle}}^{(o)}$$

Adiabatic wall

$$M = 4.00$$

$$= 5.00$$

$$= 6.06$$

$$\rightarrow \infty$$

Chapman

$$X^{(o)} = 1.479 \frac{x-x_o}{x_o} \frac{1}{\sqrt{\chi_o}}$$

$$= 1.591$$

$$= 1.729$$

$$= 1.840$$

Curle

$$X^{(o)} = 1.342 \frac{x-x_o}{x_o} \frac{1}{\sqrt{\chi_o}}$$

$$= 1.488$$

$$= 1.582$$

$$= 1.840$$

$$\begin{array}{lcl}
 \text{Cold wall} & & \\
 \text{e.g. } \frac{T_w}{T_\infty} = 1.70 & & \\
 M_\infty = 6.06 & X^{(o)} = 4.08 \frac{x-x_o}{x_o} \frac{1}{\sqrt{\chi_o}} & X^{(o)} = 6.69 \frac{x-x_o}{x_o} \frac{1}{\sqrt{\chi_o}} \\
 \rightarrow \infty \left( \frac{T_w}{T_\infty} - \text{fixed} \right) & \rightarrow 7.05 & \rightarrow \infty \\
 & & \text{(which implies } \frac{\Delta x}{x_o} \rightarrow 0)
 \end{array}$$

We see that the two scaling laws are empirically indistinguishable when applied to the experimental range of adiabatic conditions. However, for the cold wall at Mach 6 Curle's scaling shows nearly twice the effect of Chapman's scaling, becoming more severe at higher Mach numbers. This difference seems to be reflected in the experimental correlation shown in Figure 69, where Curle's scaling is used for both adiabatic and cold wall data (all  $\chi_o$ ). The variation of  $P$  with  $\chi_o$ , including the cold wall data, again exhibits the same decreasing trend with  $\chi_o$  (Figure 70).

Lees (18) has considered this problem with the aid of the moment or integral method and is able to show (appendix 2c) that Curle's scaling is valid; however for highly cooled walls  $\frac{T_o}{T_{o\infty}}$  cannot be entirely eliminated and enters as a parameter. The empirical fact that the present investigation does not exhibit an appreciable dependence on  $\frac{T_w}{T_{o\infty}}$  is not fully understood and any conclusion must be withheld until the equations, including the energy equation, have been integrated. This is presently being investigated by J. Klineberg at Caltech using a two parameter moment formulation.



In summary, it has been demonstrated that the similarity scaling obtained by the dimensional argument of Chapman contains the wall temperature ratio as an important independent parameter,  $P = P \left( X_{\text{Chapman}}; \chi_o, \frac{T_w}{T_\infty} \right)$ . On the other hand, in the similarity variables suggested by Curle the temperature ratio does not appear as an independent parameter, and over the reasonably wide range of experimental conditions encountered during this investigation all data reduce to a single curve with a slight dependence on  $\chi_o$  which is attributed to the nonlinear term in the pressure-deflection relation,  $P \cong P \left( X_{\text{Curle}}; \chi_o \right)$ . No quantitative measure was made of the location of separation and hence of the separation pressure. However, the plateau pressure which is being approached appears to be in good agreement with the empirical data for  $1.3 \leq M_\infty \leq M_\infty \leq 3.6$  of Chapman ( $P_p \cong 2.23$ ) and the theoretical estimate and experimental data at  $M_\infty = 2.0$  of Hakkinen ( $P_p = 2.33$ ).

**TABLE 1**

Range of Experimental Parameters for Free Interaction Correlation

Model	Wall Temperature	Mach No.	$\chi_o$	Symbol
AR-1	adiabatic	4.00	.0798	◇
			.0925	◇
			.1098	◇
			.129	◇
			.152	▢
			.187	▢
			.219	▢
			.284	▢
AR-1	adiabatic	5.00	.192	▽
			.229	Υ
			.266	×
			.306	+
			.378	⋈
S-1	adiabatic	6.06	.274	▽
			.303	▽
			.387	▴
			.429	▴
			.483	□
			.579	□
C-1	adiabatic	6.06	.386	○
			.406	△
			.430	□
			.461	◇
			.499	▴

Table 1 (Cont'd)

Model	Wall Temperature	Mach No.	$\chi_o$	Symbol
C-1	adiabatic	6.06	.543	▲
			.603	◻
			.685	D
C-1	$\frac{T_w}{T_\infty} = 1.70$	6.06	.362	●
			.381	▲
			.403	■
			.425	◆
			.456	▶
			.496	▲
			.551	■
			.628	D

## 7. SUMMARY

A study has been made of the two-dimensional boundary layer separation associated with a compression corner at Mach 4-6, over a Reynolds number range of  $Re_{x_c} = 6.8 \times 10^4 - 1.0 \times 10^6$ , and for both adiabatic and highly cooled models.

### 7.1. Two-Dimensionality

In order to obtain two-dimensional flow the outflow and the disturbance caused by the interaction with the wind tunnel boundary layers were eliminated by mounting side plates or fences on the model. The disturbance caused by the side plates themselves was minimized by designing them swept and with sharp leading edges. The spanwise distance between them was varied until the centerline surface pressure distribution reached a limit for each configuration and condition; the limit was attained at a moderate aspect ratio (of order 1 under the conditions encountered). The spanwise pressure distribution became uniform while the centerline distribution was still varying and hence this test is not acceptable as a sufficient experimental criterion for two-dimensional flow. An observation of the disturbance caused by the side plates to a flow which approximated the two-dimensional flow and had no end effects (stovepipe configuration at JPL) confirmed that the limit was not affected by the side plates.

### 7.2. Laminar Flow

A model which could be run either in a highly cooled or an adiabatic wall condition was designed for use in the GALCIT Mach 6 tunnel. Pitot pressure surveys were made of the boundary layer downstream of reattachment and the Mach number distribution was

calculated by assuming that the static pressure was constant across the boundary layer. The Mach number distributions were then contrasted with a theoretically predicted asymptotic laminar profile. Those flows undergoing transition exhibited distinct distortions beyond (fuller profiles) this prediction. It was assumed that those flows which did not exhibit this level of distortion were "effectively" laminar.

The effect of cooling for laminar flow with a fixed geometry, Mach number and Reynolds number was observed to be: (1) a reduction of scale approximately proportional to the reduction in the displacement thickness of an undisturbed boundary layer; (2) a reduction of upstream influence beyond this scaling effect; (3) a reduction in the overall pressure level of the magnitude of the reduced interaction pressure on the plate preceding separation.

Those flows which remained laminar as the Reynolds number was increased exhibited the upstream propagation of separation predicted by Lees and Reeves.

All adiabatic flows believed to be laminar were compared with the Lees-Reeves theory (as modified by Klineberg and Lees) and good correlation was obtained over a wide range of parameters.

### 7.3. Transition

In addition to the distortion of boundary layer profiles, the surface recovery temperature, qualitative fluctuation measurements and some shadowgraph observations were used to detect the existence of transition. In all cases, the transition appeared to occur near or aft of reattachment.

In order to ascertain the effect of transition, transitional interactions were compared with the theoretical prediction for the laminar shock wave-boundary layer interaction. Within the limitations of this theoretical prediction for the laminar flow, such a comparison shows the effect of transition to be threefold: (1) the upstream influence has been reduced; (2) the pressure gradient in the reattachment region has steepened; and (3) the pressure overshoot (above inviscid  $p_\infty$ ) has increased.

The effect of increasing Reynolds number for transitional interactions was to decrease the upstream influence, which is opposite to the trend observed for laminar flows.

#### 7.4. Free Interaction

The "free interaction" concept was confirmed and the data correlated according to the scaling suggested by both Chapman and Curle. Both correlate the adiabatic wall data well, with the exception of a dependence on the interaction parameter,  $\chi_0$ , which is shown to be important for hypersonic flows. The correlation of the cold wall data exhibits a dependence on wall temperature beyond that suggested by the Chapman scaling. The form suggested by Curle appears to remove this additional dependence.

#### 7.5. Suggestions for Future Work

Several extensions of the investigation present themselves:

(1) The measurement of heat transfer and skin friction throughout the interaction region.

(2) An investigation of the effect of wall temperature over a wider range of  $\frac{T_w}{T_\infty}$ .

- (3) An investigation of the effect of initial conditions; for example, the effect of a negative pressure gradient upstream of the interaction.
- (4) A quantitative study of the instability of the separated and re-attaching flow.
- (5) A study of the effect of geometry, as for example ramp curvature and ramp length.

## REFERENCES

1. Chapman, D. R., Kuehn, D. M. and Larson, H. K.: "Investigation of Separated Flows in Supersonic and Subsonic Streams with Emphasis on the Effect of Transition," NACA TN 3869 (March 1957).
2. Gadd, G. E.: "An Experimental Investigation of Heat Transfer Effects on Boundary Layer Separation in Supersonic Flow," J. Fluid Mech. 2 (1957).
3. Hakkinen, R. J., Greber, I., Trilling, L. and Abarbanel, S. S.: "The Interaction of an Oblique Shock Wave with a Laminar Boundary Layer," NASA Memo 2-18-59W (1959).
4. Sterrett, J. R. and Emery, J. C.: "Extension of Boundary Layer Separation Criteria to a Mach Number of 6.5 by Utilizing Flat Plates with Forward Facing Steps," NASA TN D-618 (Dec. 1960).
5. Bogdonoff, S. M. and Vas, I. E.: "Some Experiments on Hypersonic Separated Flows," ARS Journal 32 (Oct. 1962).
6. Miller, D. S., Hijman, R. and Childs, M. E.: "Mach 8 to 22 Studies of Flow Separations Due to Deflected Control Surfaces," AIAA J. 2:2 (Feb. 1964).
7. Needham, D. A.: "Laminar Separation in Hypersonic Flow," Ph.D. Thesis, University of London (August 1965).
8. Lees, L. and Reeves, B. L.: "Supersonic Separated and Re-attaching Laminar Flows: I. General Theory and Application to Adiabatic Boundary Layer/Shock Wave Interactions," AIAA J. 2:11 (Nov. 1964).
9. Kendall, J. M. Jr.: "An Experimental Investigation of Leading Edge Shock Wave Boundary Layer Interaction at Mach 5.8", AIAA J. 24:1 (Jan. 1957).
10. Lees, L. and Probstein, R. F.: "Hypersonic Flows of a Viscous Fluid," Unpublished Monograph, Brown University Library, Providence, R. I. (1953).
11. Reeves, B. L.: "The Compressible Boundary Layer in Separated Flow Past a Compression Corner," Space General Corporation Report (May 3, 1963).
12. Curle, N.: "The Effects of Heat Transfer on Laminar Boundary Layer Separation in Supersonic Flow," Aero. Quarterly, Vol. XII (Nov. 1961).



## REFERENCES (Cont'd)

13. Kendall, J. M. Sr.: "JPL 120-Part Multiple Pressure Measuring System," Paper presented at the 24th Semi-Annual Meeting of the Supersonic Wind Tunnel Association held at Los Angeles, California (Nov. 1, 1965).
14. Dewey, C. F. Jr.: "Measurements in Highly Dissipative Regions of Hypersonic Flows. Part II. The Near Wake of a Blunt Body at Hypersonic Speeds," Ph.D. Thesis, Calif. Inst. of Tech., Pasadena, Calif. (1963).
15. Klineberg, J. M. and Lees, L.: Private Communication (1966).
16. Kubota, T.: Private Communication (1966).
17. Behrens, W.: Private Communication (1966).
18. Lees, L.: Private Communication (1966).
19. Sherman, F. S.: "New Experiments on Impact Pressure Interpretation in Supersonic and Subsonic Rarefied Airstreams," Univ. of Calif. Tech. Rept. No. HE-150-99 (Dec. 21, 1951).
20. Homann, F.: "The Effect of High Viscosity on the Flow Around a Cylinder and Around a Sphere," Univ. of Calif. Tech. Rept. No. HE-150-88 (July 17, 1951).
21. Hayes, W. D. and Probstein, R. F.: "Hypersonic Flow Theory," Academic Press, New York and London (1959).
22. Chapman, D. R. and Rubesin, M. W.: "Temperature and Velocity Profiles in the Compressible Laminar Boundary Layer with Arbitrary Distribution of Surface Temperature," Presented at the Fluid Mechanics Session, Seventeenth Annual Meeting, I.A.S., New York (January 24-27, 1949).
23. Schlichting, H.: "Boundary Layer Theory," McGraw-Hill, New York, N. Y., pp. 344-346 (1960).

## APPENDIX 1

REYNOLDS NUMBER CORRECTION FOR PITOT MEASUREMENTS

There are at least three factors which must be considered in interpreting Pitot pressure measurements in a boundary layer: (1) as the probe nears the wall the Reynolds number becomes small, giving rise to viscous effects; (2) the stagnating streamline is displaced because of a lateral velocity gradient; (3) as the probe approaches the wall, the presence of the solid boundary becomes an important factor in the local flow field.

The experimental Mach number distribution obtained on a flat plate is contrasted with a theoretical solution based on the Sutherland viscosity law (16) (Figure 19). From the agreement with the theoretical prediction in the region  $M > 1$  it is concluded that all three effects are unimportant in this region. If it is assumed that: (1) the displacement created by the velocity gradient is not important; (2) there exists a region near enough the wall that viscous effects are important ( $Re \leq 10$ ), but far enough removed so that the boundary condition imposed by the presence of the wall does not appreciably influence the probe measurement, then we have some hope of making a meaningful correction to the measurements.

Sherman (19) has made measurements up to  $M = .7$  with two different axi-symmetric probes, one approximately source shaped with .20h opening and the other a flat-ended probe with internal chamfer. Both show reasonable agreement with the theoretical prediction of Homann (20) for the impact pressure on a sphere at  $M = 0$ .

For probe locations greater than three probe heights from the wall we have taken the difference between the measured impact pressure and that predicted by the theoretical calculations under ideal (isentropic compression) conditions, and plotted the data obtained for  $M < 1$  in the manner of Sherman; here  $C_\mu = \frac{p_t(\text{meas}) - p_t(\text{ideal})}{\gamma/2 p_1 M^2}$  and  $Re_h$  is the Reynolds number based on height of the probe (Figure 71). The Reynolds number was calculated by approximating the temperature field (which was not measured directly) by the form suggested by Schlichting (23),

$$\frac{T}{T_e} = \frac{1 + \sqrt{P_r} \frac{\gamma-1}{2} M_e^2}{1 + \sqrt{P_r} \frac{\gamma-1}{2} M_e^2}$$

The probes used throughout the investigation were flat ended (opening  $\sim .3h$  and flattened width/height  $\approx 15$ ). Homann's solution for the impact pressure on a cylinder (the probe was believed to be closer to this configuration than a sphere) is  $C_\mu = \frac{4}{Re + .46 \sqrt{Re}}$ , and this result falls within the scatter band. Because of the rather large amount of scatter the complexity of this form is not warranted and an empirical fit of the form  $C_\mu = \frac{2.2}{Re}$  has been chosen as best representing the data. As the probe came closer than  $\sim 3h$  to the plate the measured value of  $C_\mu$  showed increasing deviation from this form, and it is concluded that this region is greatly affected by the solid boundary.

This form of viscous correction requires iteration if one starts with a measured Pitot pressure, and attempts to infer Mach number. However, by starting with Mach number = .1, .2, .3 etc., knowing  $\frac{p}{p_\infty}$  and  $Re_\infty$  we can calculate  $\frac{p_t}{p_\infty}$  (meas) and since the measured impact pressure in this region is quite smooth, we can find the corre-

sponding location by curve fitting the data (Figure 72), thus eliminating the iteration.

This correction represents a "first order" look at the effect of Reynolds number on probes of the geometry utilized in this particular boundary layer study. These findings must necessarily be verified under conditions in which there does not exist either a solid boundary or a velocity gradient.

With this limitation in mind, all adiabatic profiles have been corrected according to this formulae. The subsonic portion of the cold wall profiles lies within  $\sim 4h$  and hence no correction was attempted.

## APPENDIX 2

(a) Chapman scaling

Since only  $p = p(x)$  has been determined experimentally it is necessary to estimate theoretically the other parameters which enter the free interaction similarity scaling.

First,

$$P = \frac{C_{p_o} (M_o^2 - 1)^{\frac{1}{4}}}{\sqrt{C_{f_o}}} \quad \text{and}$$

$$C_{p_o} = \frac{2}{\gamma} \frac{p - p_o}{p_o} \frac{1}{M_\infty^2} \left( \frac{M_o}{M_\infty} \right)^{-2},$$

$$C_{f_o} = C_{f_\infty} \left( \frac{p_o}{p_\infty} \right)^{-1} \left( \frac{M_o}{M_\infty} \right)^{-2} \quad \text{where} \quad C_{f_\infty} = \frac{\tau_w}{\gamma/2 p_\infty M_\infty^2}.$$

So

$$P = \frac{2}{\gamma} \frac{p - p_o}{p_o} \frac{1}{M_\infty^2} \left( \frac{M_o}{M_\infty} \right)^{-2} \frac{1}{\sqrt{C_{f_\infty}}} \left( \frac{p_o}{p_\infty} \right)^{\frac{1}{2}} \left( \frac{M_o}{M_\infty} \right)^1 M_\infty^{\frac{1}{2}} \left( \frac{M_o}{M_\infty} \right)^{\frac{1}{2}} \left\{ 1 - \frac{1}{4 M_o^2} + \dots \right\}$$

or neglecting  $1/4 M_o^2$ ,

$$P = \frac{2}{\gamma} \frac{p - p_o}{p_o} \frac{1}{M_\infty^{\frac{3}{2}} \sqrt{C_{f_\infty}}} \left( \frac{p_o}{p_\infty} \right)^{\frac{1}{2}} \left( \frac{M_o}{M_\infty} \right)^{-\frac{1}{2}}$$

Following Lees-Probstein (10) for  $M_\infty^2 \gg 1$  and  $M_\infty \frac{d\delta^*}{dx} \ll 1$ ,

$$\frac{p}{p_\infty} = 1 + \gamma \left( M_\infty \frac{d\delta^*}{dx} \right) + \dots, \quad \text{which implies}$$

$$\frac{M_e}{M_\infty} = 1 - \frac{1 + \frac{\gamma-1}{2} M_\infty^2}{M_\infty^2} \left( M_\infty \frac{d\delta^*}{dx} \right) + \dots \quad \text{and}$$

$$C_{f\infty} = C_{f\infty}^{(0)} + \frac{2}{M_\infty^3} \left( M_\infty \frac{d\delta^*}{dx} \right) + \dots \quad (\text{Ref. 21})$$

where

$M_\infty \frac{d\delta^*}{dx}$  and  $C_{f\infty}^{(0)}$  are evaluated for non-interacting flow:

$$\frac{\delta^*}{x} \sqrt{Re_x} = \sqrt{C_\infty} \left\{ 1.937 \frac{T_W}{T_\infty} + .578 \frac{\gamma-1}{2} M_\infty^2 - .207 \right\} \quad (\text{Ref. 21})$$

$$C_{f\infty}^{(0)} = \frac{.664 \sqrt{C_\infty}}{\sqrt{Re_x}} \quad (\text{Ref. 22})$$

By utilizing these relations,

$$P = \frac{2}{\gamma} \frac{p-p_0}{p_0} \frac{Re_x^{\frac{1}{4}}}{M_\infty^{\frac{3}{2}} \sqrt{.664} C_\infty^{\frac{1}{4}}} \left\{ 1 + \left( \frac{\gamma}{2} + \frac{1+\gamma-1}{2} \frac{M_\infty^2}{2M_\infty^2} \right) \left( M_\infty \frac{d\delta^*}{dx} \right) - \frac{1}{M_\infty^3} \frac{Re_x^{\frac{1}{2}}}{.664 C_\infty^{\frac{1}{2}}} \left( M_\infty \frac{d\delta^*}{dx} \right) + \dots \right\}$$

and neglecting  $\frac{1}{2M_\infty^2}$ ,

$$P = 1.752 \frac{p-p_0}{p_0} \frac{1}{\sqrt{\chi_0}} \left\{ 1 + \frac{3\gamma-1}{4} \left( M_\infty \frac{d\delta^*}{dx} \right) - \frac{1.508}{\chi_0} \left( M_\infty \frac{d\delta^*}{dx} \right)^2 + \dots \right\}$$

Next,  $X = \frac{x-x_0}{\delta_0^*} \sqrt{C_{f0}} (M_0^2 - 1)^{\frac{1}{4}} \quad \text{or,}$

$$X = \frac{x-x_0}{x_0} \left( \frac{\delta^*}{x} \right)_0 \sqrt{C_{f\infty}} \left( \frac{p_0}{p_I} \right)^{-\frac{1}{2}} \left( \frac{M_0}{M_\infty} \right)^{-1} M_\infty^{\frac{1}{2}} \left( \frac{M_0}{M_\infty} \right)^{\frac{1}{2}} \left\{ 1 - \frac{1}{4M_0^2} + \dots \right\}$$

and again neglecting  $\frac{1}{4M_0^2}$

$$X = \frac{x-x_0}{x_0} \frac{M_\infty^{\frac{1}{2}} \sqrt{C_{f\infty}}}{\left( \frac{\delta^*}{x} \right)} \left( \frac{p_0}{p_\infty} \right)^{-\frac{1}{2}} \left( \frac{M_0}{M_\infty} \right)^{-\frac{1}{2}}$$

which becomes

$$X = \frac{x-x_0}{x_0} \frac{\sqrt{.664} \operatorname{Re}_x^{\frac{1}{4}}}{M_\infty^{\frac{3}{2}} C_\infty^{\frac{1}{4}}} \frac{1}{G} \left\{ 1 + \left( -\frac{\gamma}{2} + \frac{1}{2} \frac{1+\frac{\gamma-1}{2} M_\infty^2}{M_\infty^2} \right) M_\infty \frac{d\delta^*}{dx} \right. \\ \left. + \frac{C_\infty^{\frac{1}{2}} \operatorname{Re}_x^{\frac{1}{2}}}{M_\infty^3 (.664)} \left( M_\infty \frac{d\delta^*}{dx} \right)^2 + \dots \right\}$$

where

$$G \equiv \frac{\delta^*}{x} \frac{\sqrt{\operatorname{Re}_x}}{M_\infty^2 \sqrt{C_\infty}}$$

and finally,

$$X = 0.815 \frac{x-x_0}{x_0} \frac{1}{\sqrt{\chi_0}} G^{-1} \left( \frac{T_w}{T_\infty}, M_\infty \right) \left\{ 1 - \frac{\gamma+1}{4} \left( M_\infty \frac{d\delta^*}{dx} \right) \right. \\ \left. + \frac{1.508}{\chi_0} \left( M_\infty \frac{d\delta^*}{dx} \right)^2 + \dots \right\}.$$

### (b) Curle scaling

The scaling suggested by Curle can be arrived at by Chapman's argument provided one introduces a partial transformation to incompressible variables,  $\frac{\partial}{\partial y} = \frac{\rho}{\rho_e} \frac{\partial}{\partial Y}$  and approximates the temperature field by the Crocco integral (the complexity of Curle's approximation of the energy integral is unnecessary for this argument),

$$\frac{T}{T_e} = \frac{T_w}{T_e} + \frac{T_w}{T_e} \left( 1 - \frac{u}{u_e} \right) + \frac{\gamma-1}{2} M_e^2 \frac{u}{u_e} \left( 1 - \frac{u}{u_e} \right).$$

It follows that

$$\delta^* = \int_0^\delta \left( 1 - \frac{\rho u}{\rho_e u_e} \right) dy = \frac{T_w}{T_e} \delta_i^* + \frac{\gamma-1}{2} M_e^2 \theta_i.$$

Neglecting the variation of  $M_e^2 \theta_i$  in comparison with the variation

of  $\frac{T_w}{T_e} \delta_i^*$  implies  $\theta - \theta_o \cong \frac{T_w}{T_e} \frac{d}{dx} (\delta_i^* - \delta_{i_o}^*)$ .

Now

$$\frac{p - p_o}{\frac{\gamma}{2} p_o M_o^2} = \frac{2(\theta - \theta_o)}{\sqrt{M_o^2 - 1}}$$

$$C_{p_o} \sqrt{M_o^2 - 1} = 2 \frac{T_w}{T_e} \frac{\delta_{i_o}^*}{l_i} \frac{dD}{dX} \quad \text{where } D = \frac{\delta_i^*}{\delta_{i_o}^*} - 1$$

and

$$P = 2 \frac{dD}{dX} \quad \text{provided}$$

$$P = C_{p_o} \sqrt{M_o^2 - 1} \frac{l_i}{\delta_{i_o}^*} \left( \frac{T_w}{T_e} \right)^{-1}$$

Taking the momentum equation at the wall,

$$\frac{dp}{dx} = \left( \frac{\partial \tau}{\partial y} \right)_w = \frac{p_w}{p_e} \frac{\tau_o}{\delta_{i_o}^*} \left( \frac{\partial \bar{\tau}}{\partial \bar{Y}} \right)_w$$

or

$$\frac{\gamma}{2 l_i} \frac{p_o M_o^2}{\sqrt{M_o^2 - 1}} \frac{dP}{dX} \frac{\delta_{i_o}^*}{l_i} \left( \frac{T_w}{T_e} \right) = \frac{T_e}{T_w} \frac{\tau_o}{\delta_{i_o}^*} \left( \frac{\partial \bar{\tau}}{\partial \bar{Y}} \right)_w$$

$$\text{and } \frac{dP}{dX} = \left( \frac{\partial \bar{\tau}}{\partial \bar{Y}} \right)_w \quad \text{provided } \left( \frac{\delta_{i_o}^*}{l_i} \right)^2 = \left( \frac{T_e}{T_w} \right)_o^2 C_{f_o} (M_o^2 - 1)^{\frac{1}{2}}$$

which implies

$$P = \frac{C_{p_o} (M_o^2 - 1)^{\frac{1}{4}}}{\sqrt{C_{f_o}}} \quad \text{and } X = \frac{x - x_o}{\delta_{i_o}^*} \sqrt{C_{f_o}} (M_o^2 - 1)^{\frac{1}{4}} \left( \frac{T_w}{T_e} \right)_o^{-1}.$$

The pressure scaling is identical to that of Chapman, and following Appendix 2a the X scaling can be predicted.



The temperature ratio becomes,

$$\frac{T_w}{T_e} = \frac{T_w}{T_\infty} \frac{T_\infty}{T_e} = \frac{T_w}{T_\infty} \frac{1 + \frac{\gamma-1}{2} M_e^2}{1 + \frac{\gamma-1}{2} M_e^2} = \frac{T_w}{T_\infty} \left\{ 1 - (\gamma-1) M_\infty \frac{d\delta^*}{dx} + \dots \right\}$$

and hence

$$X = \frac{x-x_0}{x_0} \frac{Re_x^{\frac{1}{4}}}{1.730 C_\infty^{\frac{1}{4}}} \sqrt{.664} M_\infty^{\frac{1}{2}} \left( \frac{T_w}{T_\infty} \right)^{-1} \left\{ 1 + \frac{3\gamma-5}{4} \left( M_\infty \frac{d\delta^*}{dx} \right) + \frac{1.508}{\chi_0} \left( M_\infty \frac{d\delta^*}{dx} \right)^2 + \dots \right\}$$

or

$$X = 0.471 \frac{x-x_0}{x_0} \frac{1}{\sqrt{\chi_0}} M_\infty^2 \left( \frac{T_w}{T_\infty} \right)^{-1} \left\{ 1 - \frac{5-3\gamma}{4} \left( M_\infty \frac{d\delta^*}{dx} \right) + \frac{1.508}{\chi_0} \left( M_\infty \frac{d\delta^*}{dx} \right)^2 + \dots \right\}.$$

### (c) Lees analysis

If one approximates the energy integral (e.g. with the Crocco integral) the interaction is determined by the following three equations (8,15) when coupled with the external Prandtl-Meyer relation:

$$(1) \quad \frac{\delta_i^*}{M_e} \frac{dM_e}{dX} = \frac{C}{Re_{\delta_i^*}} \frac{N_1}{D} (M_e, H, h)$$

$$(2) \quad \delta_i^* \frac{dH}{dX} = \frac{C}{Re_{\delta_i^*}} \frac{N_2}{D} (M_e, H, h)$$

$$(3) \quad \frac{d\delta_i^*}{dX} = \frac{C}{Re_{\delta_i^*}} \frac{N_3}{D} (M_e, H, h)$$

where

and

$$h = Re_{\delta_i^*} \frac{1 + m_e}{m_e(1+m_\infty)} \tan \Theta$$

$$Re_{\delta_i^*} = \frac{a_\infty}{v_\infty} M_e \delta_i^*.$$

If one assumes that  $\frac{\theta_i^*}{\theta_i} = K(\text{const})$ ,

$$D = (KA-G) (B-H \frac{dB}{dH})$$

$$N_1 = (KP-R) (B-H \frac{dB}{dH})$$

$$N_2 = -(KA-G)Hh - (R-KP)Hf - (GP-AR)B$$

$$N_3 = (KA-G)h - (KP-R)f + (GP-AR) \frac{dB}{dH}$$

where,

$$A = 2H+1-E$$

$$B = H + \frac{1+m_e}{m_e} (1-E)$$

$$E = -\frac{1}{\delta_i^*} \int_0^{\delta_i} \left( \frac{h_t}{h_{te}} - 1 \right) dY$$

$$f = \left[ 2 + \frac{\gamma+1}{\gamma-1} \frac{m_e}{1+m_e} \right] H + \frac{3\gamma-1}{\gamma-1} (1-E) + \frac{M_e^2-1}{m_e(1+m_e)} Z$$

$$G = 3KH + 2S_w T^*$$

$$P = P(H)$$

$$R = R(H) \quad Z = Z(H)$$

$$T^* = \frac{1}{\delta_i^*} \int_0^{\delta_i} \frac{U}{U_e} \frac{h_t - h_{te}}{h_w - h_{te}} dY$$

Utilizing the Crocco integral to approximate the temperature field,

$$\frac{h_t - h_w}{h_t - h_w} = \frac{u}{u_e} \quad \text{implies}$$

$$E = 1 - \frac{T_w}{T_{\infty}} \quad A = 2H + \frac{T_w}{T_{\infty}}$$

$$S_w T^* = -H \left( 1 - \frac{T_w}{T_{\infty}} \right) \quad G = 3KH + 2 \left( \frac{T_w}{T_{\infty}} - 1 \right) H$$

$$\frac{dB}{dH} - \frac{B}{H} = - \frac{1 + m_e}{m_e} \frac{T_w}{T_{\infty}} \frac{1}{H}$$

$$G - KA = (K-2)H + (2H-K) \frac{T_w}{T_{\infty}}$$

and the equations become,

$$(1) \quad \frac{\delta_i^*}{M_e} \frac{dM_e}{dX} = \frac{C}{Re_{\delta_i^*}} \frac{KP-R}{(2-K)H - (K-2H) \frac{T_w}{T_{\infty}}}$$

$$(2) \quad \frac{\delta_i^*}{H} \frac{dH}{dX} = - \left( \frac{T_w}{T_{\infty}} \right)^{-1} \Theta + O \left( \frac{1}{Re_{\delta_i^*}} \right)$$

$$(3) \quad \frac{d\delta_i^*}{dX} = \left( \frac{T_w}{T_{\infty}} \right)^{-1} \Theta + O \left( \frac{1}{Re_{\delta_i^*}} \right)$$

which imply

$$\frac{d\theta_i}{dX} = O \left( \frac{1}{Re_{\delta_i^*}} \right).$$

(Curle's primary assumption involves the constancy of the momentum thickness.)

By differentiating (2) and using the Prandtl-Meyer relation

$$(1 + m_e) \frac{d\theta}{d\xi} + \frac{dM_e}{d\xi} = 0 \quad \text{one finds}$$

$$(4) \quad \theta_{i_o} \frac{d}{dX} \left( \frac{1}{H^2} \frac{dH}{dX} \right) = \left( \frac{T_w}{T_\infty} \right)^{-1} \frac{1}{1+m_e} \frac{dM_e}{dX}$$

Eliminating  $\frac{dM_e}{dX}$  between Eq. (1) and (4) leads to

$$\frac{d}{dX} \left( \frac{1}{H^2} \frac{dH}{dX} \right) = \left( \frac{T_w}{T_\infty} \right)^{-1} \frac{C}{1+m_e} \frac{M_\infty H^2}{\theta_{i_o}^2 \text{Re}_{\theta_{i_o}}} \frac{KP-R}{(2-K)H+(K-2H)} \frac{T_w}{T_\infty}.$$

For

$$\frac{T_w}{T_\infty} \gg 1, \quad \frac{(2-K)H}{(K-2H) \frac{T_w}{T_\infty}} \ll 1 \quad \text{which implies}$$

$$\frac{d}{dX} \left( \frac{1}{H^2} \frac{dH}{dX} \right) \cong \frac{C}{\theta_{i_o}^2} \frac{M_\infty}{\text{Re}_{\theta_{i_o}}} \frac{1+m_\infty}{1+m_e} \left( \frac{T_w}{T_\infty} \right)^{-2} \frac{H^2 (KP-R)}{(K-2H)}$$

$$\text{and } \frac{d}{d\xi} \left( \frac{1}{H^2} \frac{dH}{d\xi} \right) + f(H) = 0 \text{ where } \xi \sim \frac{X-X_o}{\theta_{i_o}} \frac{\sqrt{C} \sqrt{M_\infty}}{\sqrt{\text{Re}_{\theta_{i_o}}}} \sqrt{\frac{1+m_\infty}{1+m_e}} \left( \frac{T_w}{T_\infty} \right)^{-1}.$$

Hence for interactions which involve small variations in  $M_e$

$$\xi \sim \frac{x-x_o}{x_o} \frac{1}{\sqrt{\chi_o}} M_\infty^2 \left( \frac{T_w}{T_\infty} \right)^{-1} \quad \text{which is}$$

the scaling obtained by Curle. However, for highly cooled walls,

$\frac{(2-K)H}{(K-2H) \frac{T_w}{T_{\infty}}} \sim 1$  and while one is free to maintain this scaling,  $\frac{T_w}{T_{\infty}}$

must be expected to enter the correlation as a parameter.

Taking the isentropic pressure deflection relation,

$$\begin{aligned} \frac{P-P_o}{P_o} &= \gamma M_o \Theta \left\{ 1 + \frac{\gamma+1}{4} M_o \Theta + \dots \right\} \\ \Theta &= \frac{T_w}{T_{\infty}} \frac{1}{\beta} \frac{\theta_{i_o}}{H^2} \frac{dH}{d\xi} \frac{d\xi}{dx} + O\left(\frac{1}{Re_{\delta_i^*}}\right) \\ \frac{d\xi}{dx} &= \frac{\bar{\beta}}{\theta_{i_o}} \frac{\sqrt{C} \sqrt{M_{\infty}}}{\sqrt{Re_{\theta_{i_o}}}} \left(\frac{1+m_{\infty}}{1+m_e}\right)^{\frac{1}{2}} \left(\frac{T_w}{T_{\infty}}\right)^{-1} \\ \Theta &= - \frac{\sqrt{C} \sqrt{M_{\infty}}}{\sqrt{Re_{\theta_{i_o}}}} \left(\frac{1+m_{\infty}}{1+m_e}\right)^{\frac{1}{2}} \frac{1}{H^2} \frac{dH}{d\xi} \end{aligned}$$

and for small variation in  $M_e$ ,

$$\frac{P-P_o}{P_o} = \sqrt{\chi_o} \left(-\frac{1}{H^2} \frac{dH}{d\xi}\right) \left\{ 1 + \frac{\gamma+1}{4} \sqrt{\chi_o} \left(-\frac{1}{H^2} \frac{dH}{d\xi}\right) \right\}$$

or

$$P = \frac{P-P_o}{P_o} \frac{1}{\sqrt{\chi_o}} = P\left(\xi; \chi_o, \frac{T_w}{T_{\infty}}\right).$$

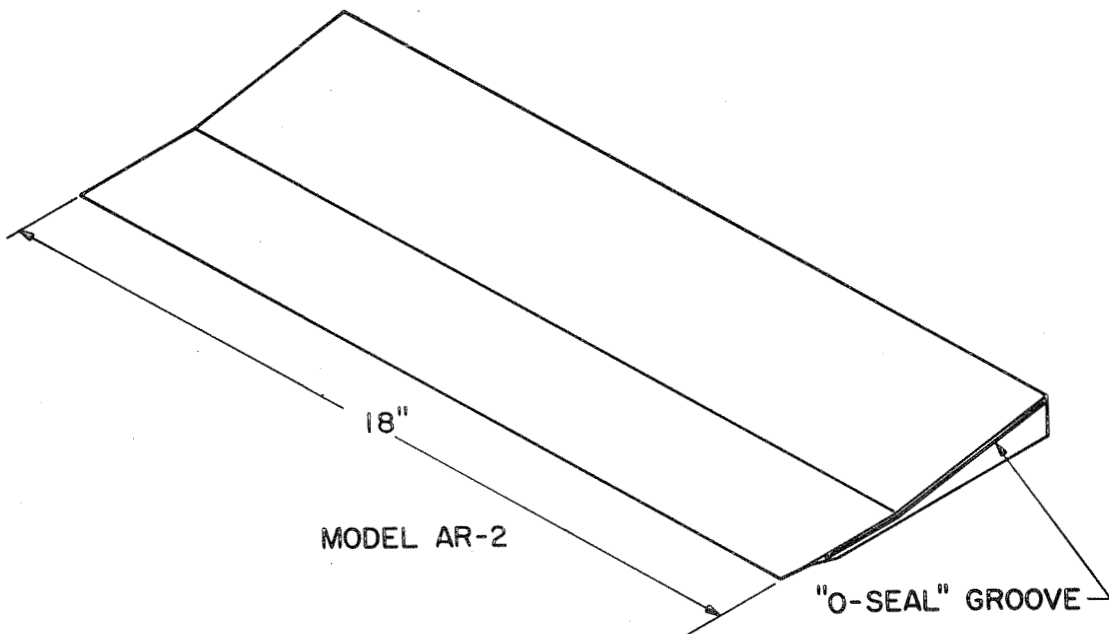
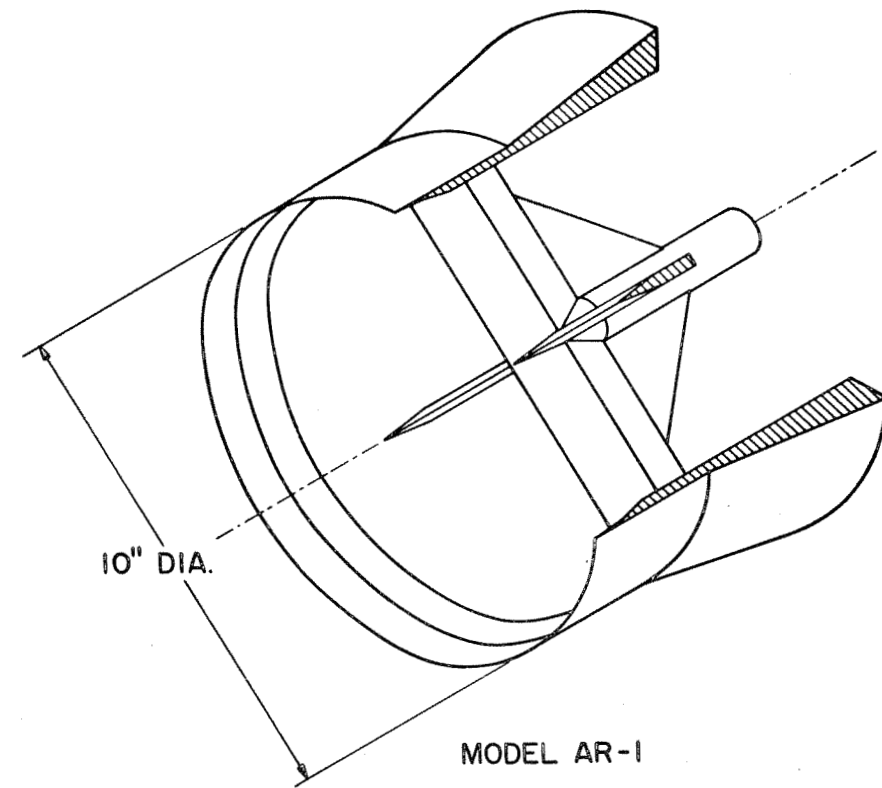


Figure 1. JPL Wind Tunnel Models AR-1, -2

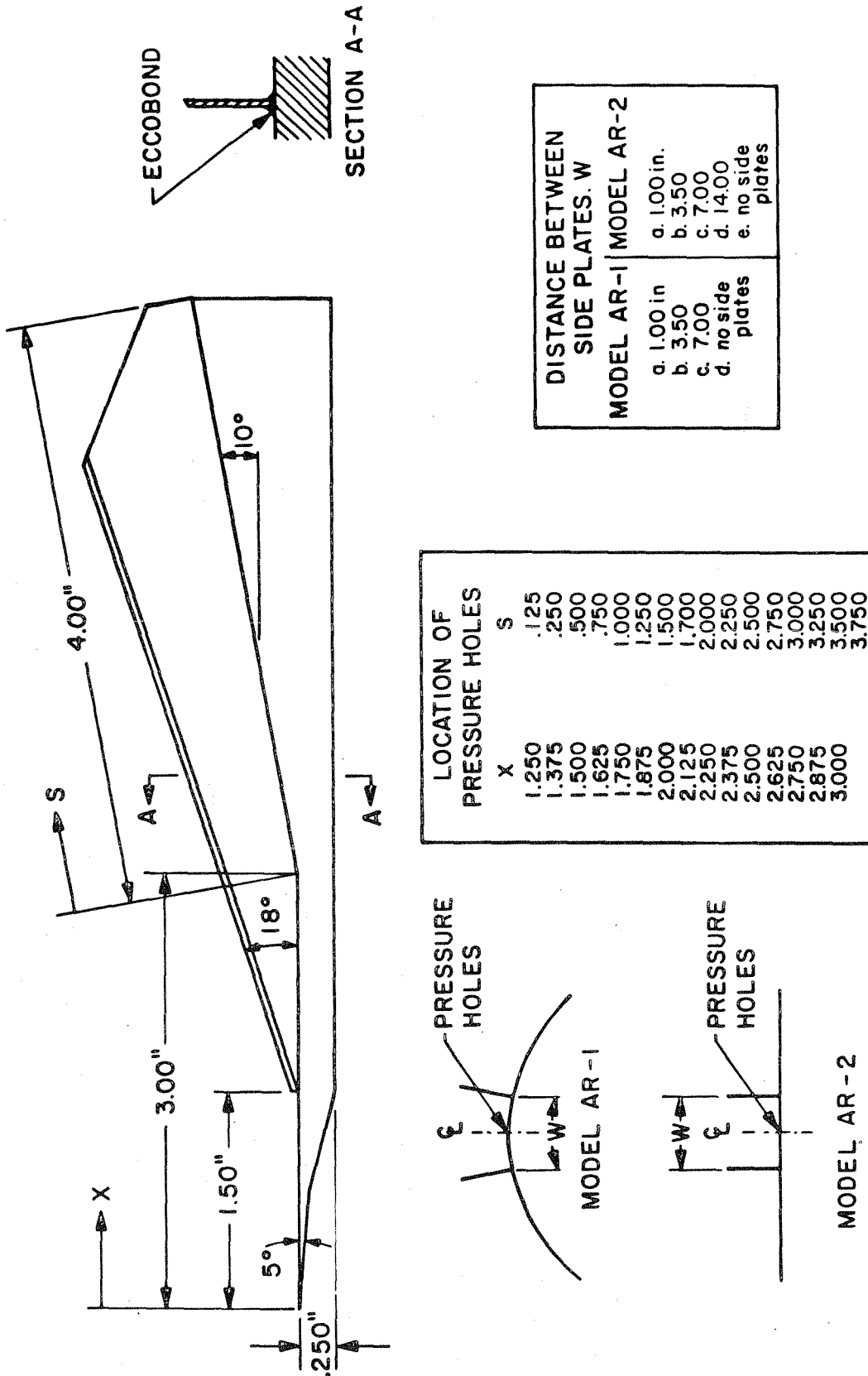


Figure 2. JPL Wind Tunnel Models AR-1, -2

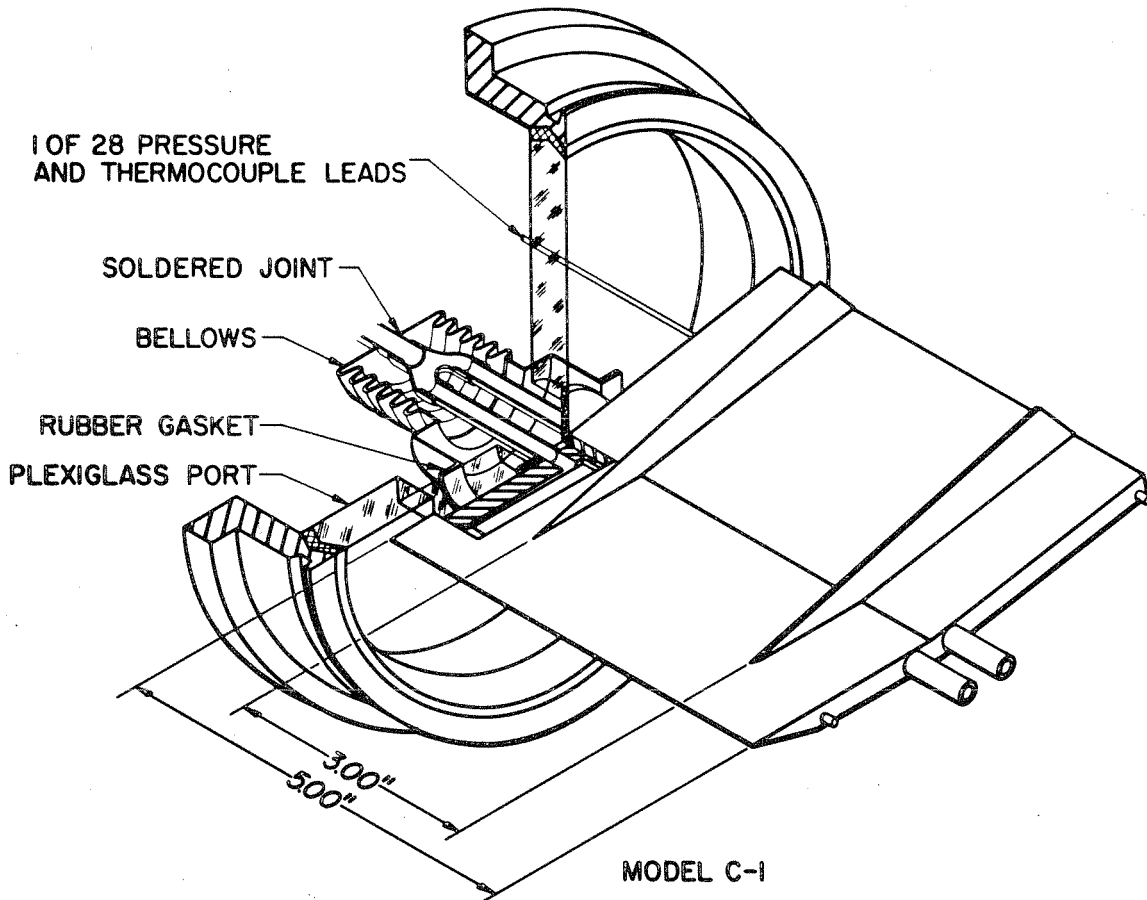


Figure 3. Wind Tunnel Model C-1.



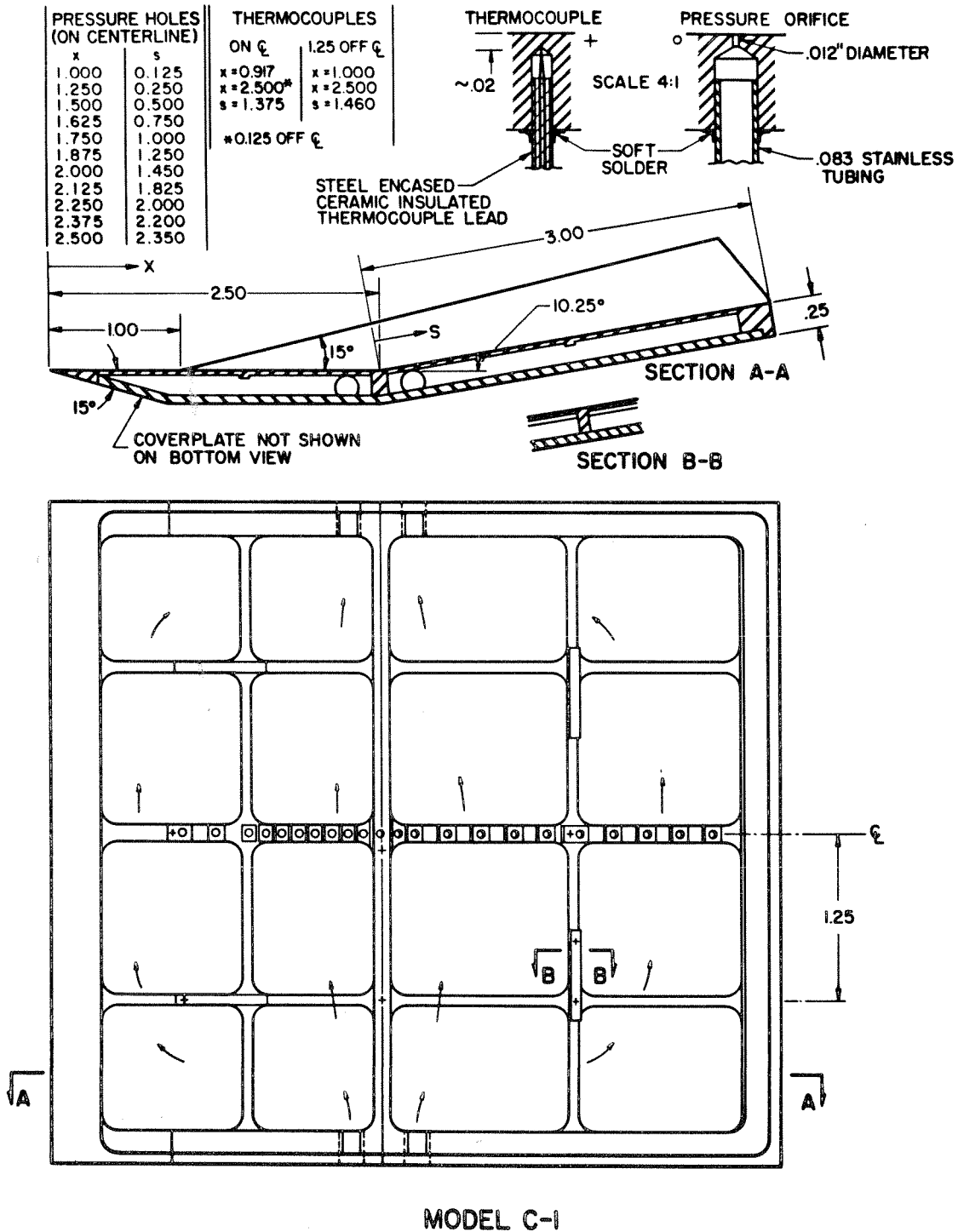


Figure 4. Wind Tunnel Model C-1.

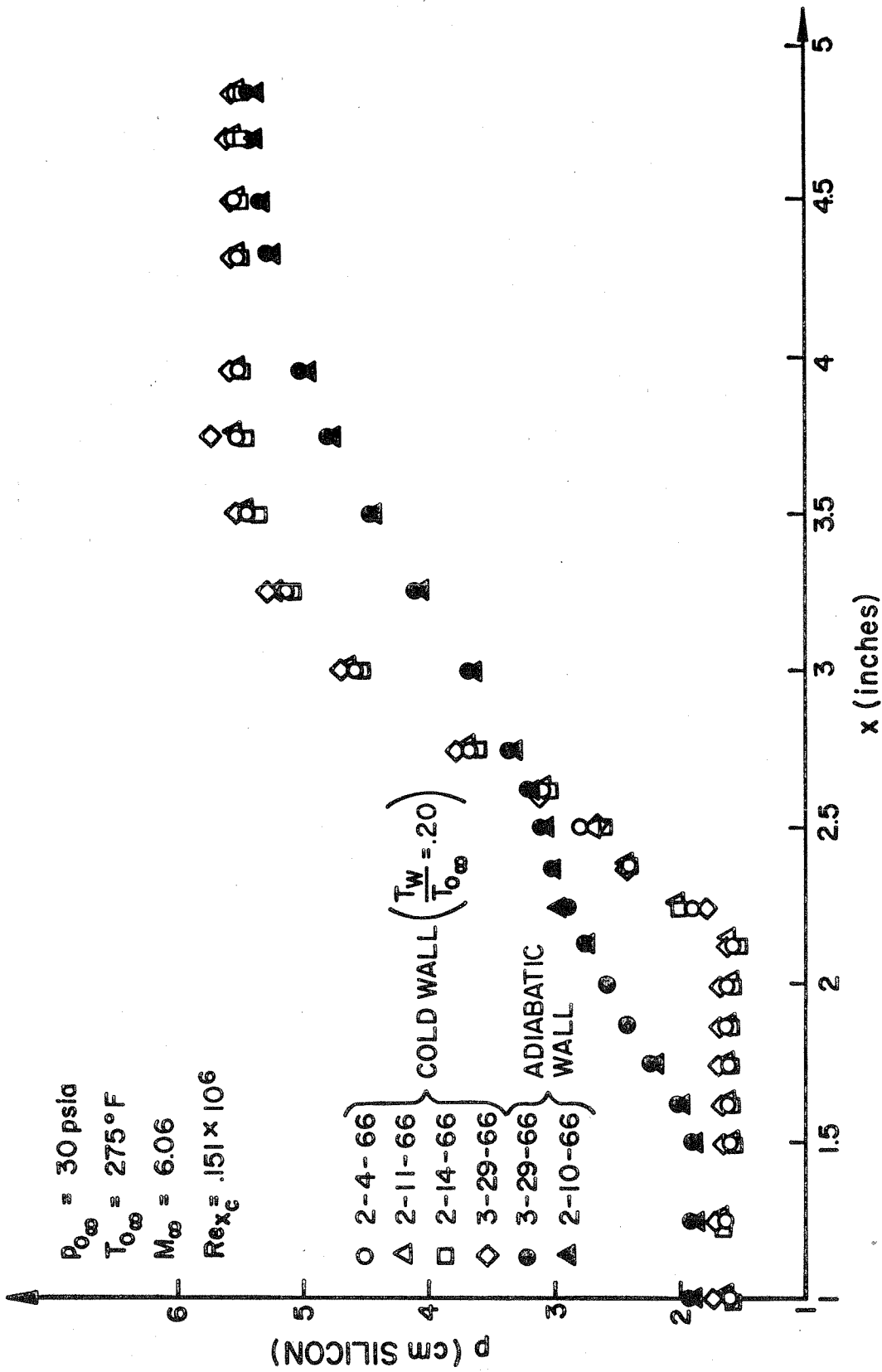


Figure 5. Surface Pressure Measurement Repeatability Check.

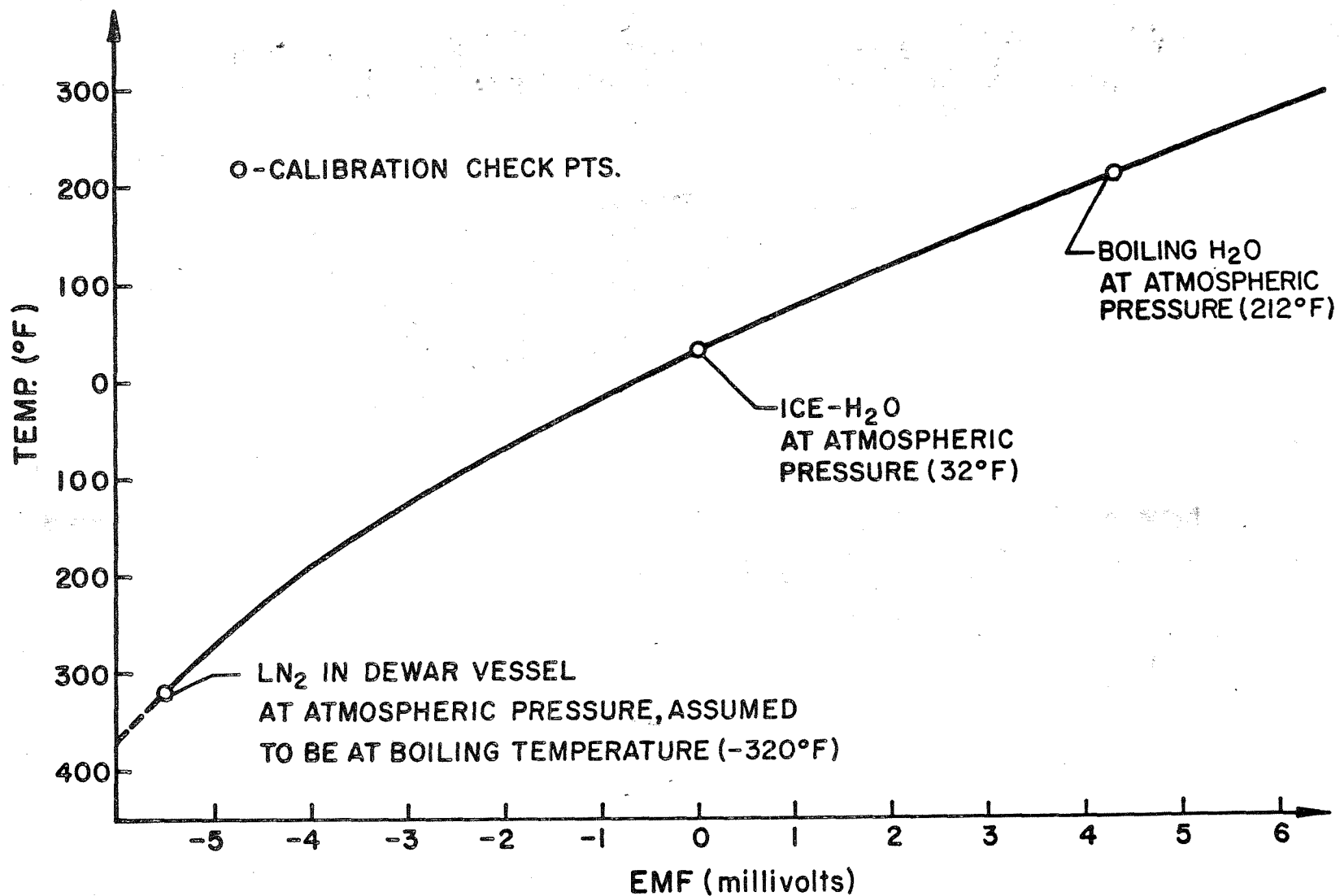


Figure 6. Thermocouple Calibration.

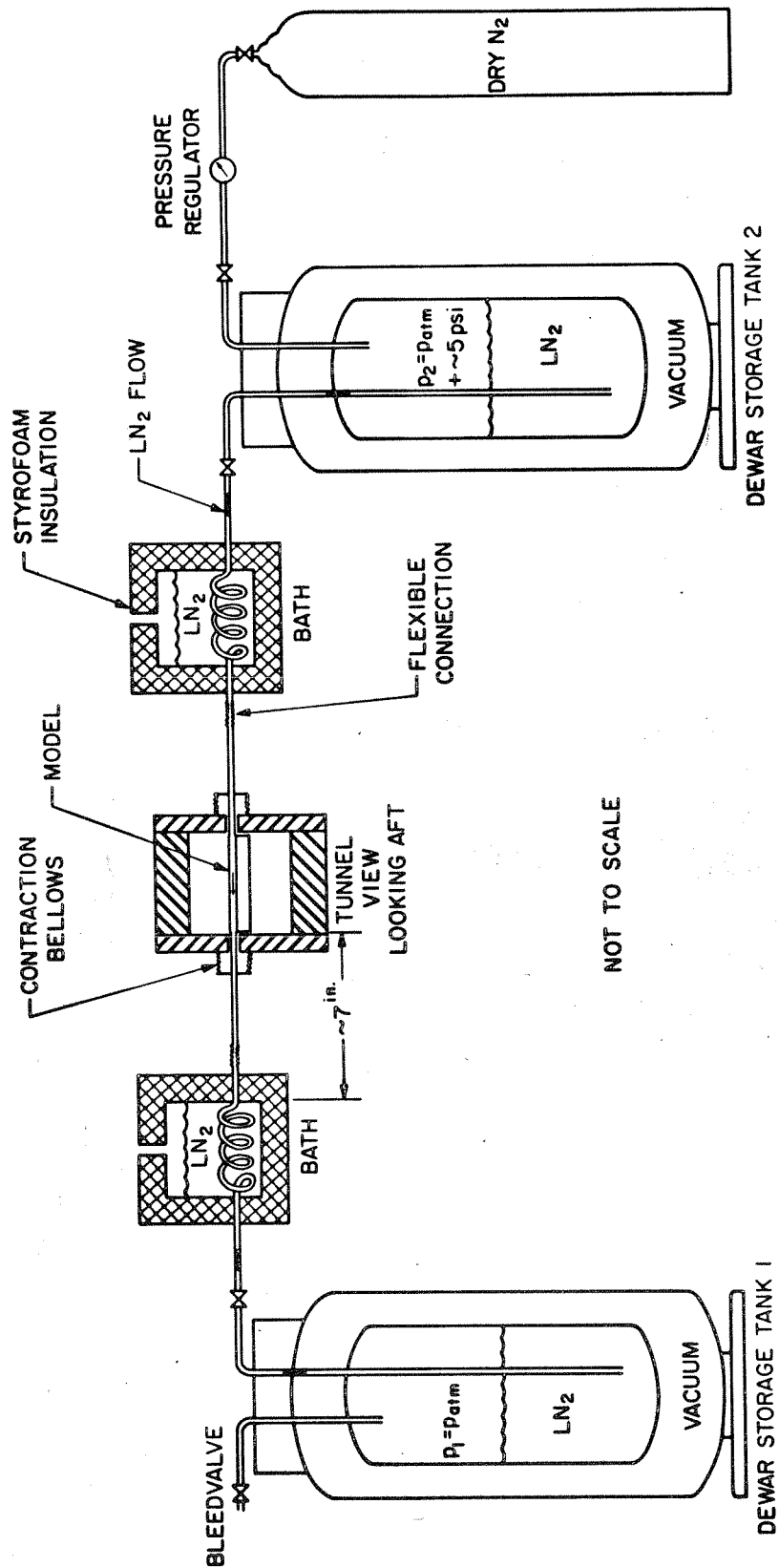
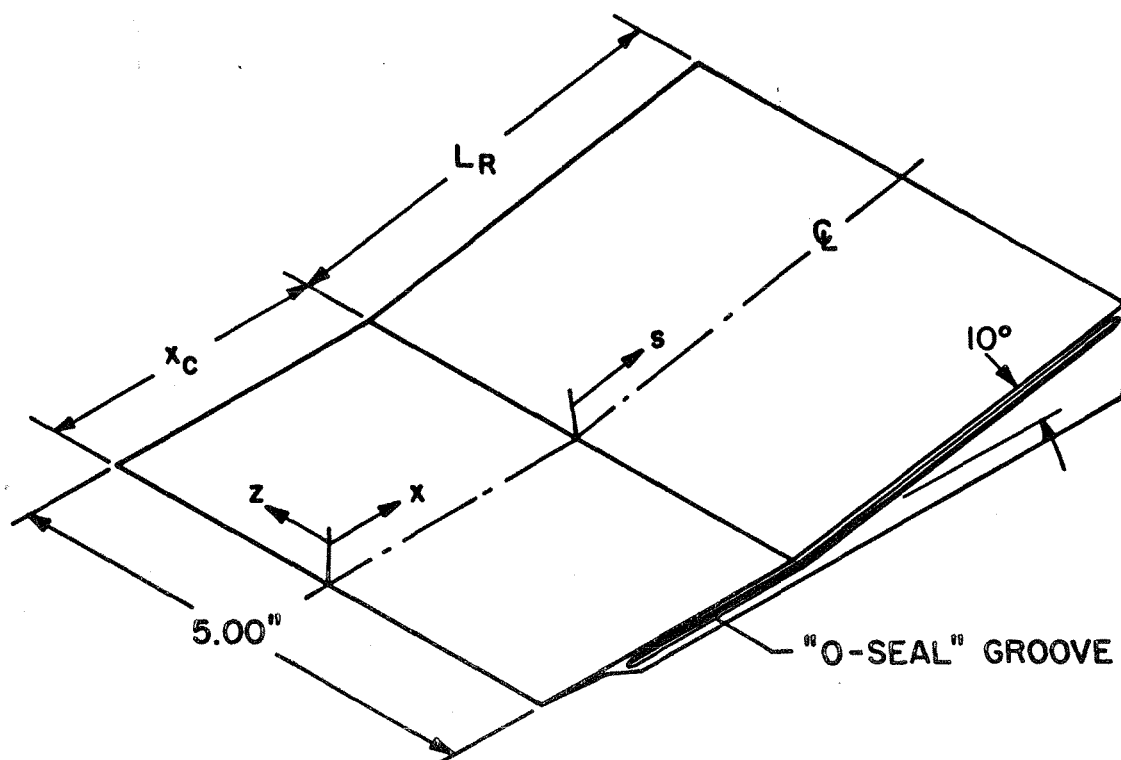


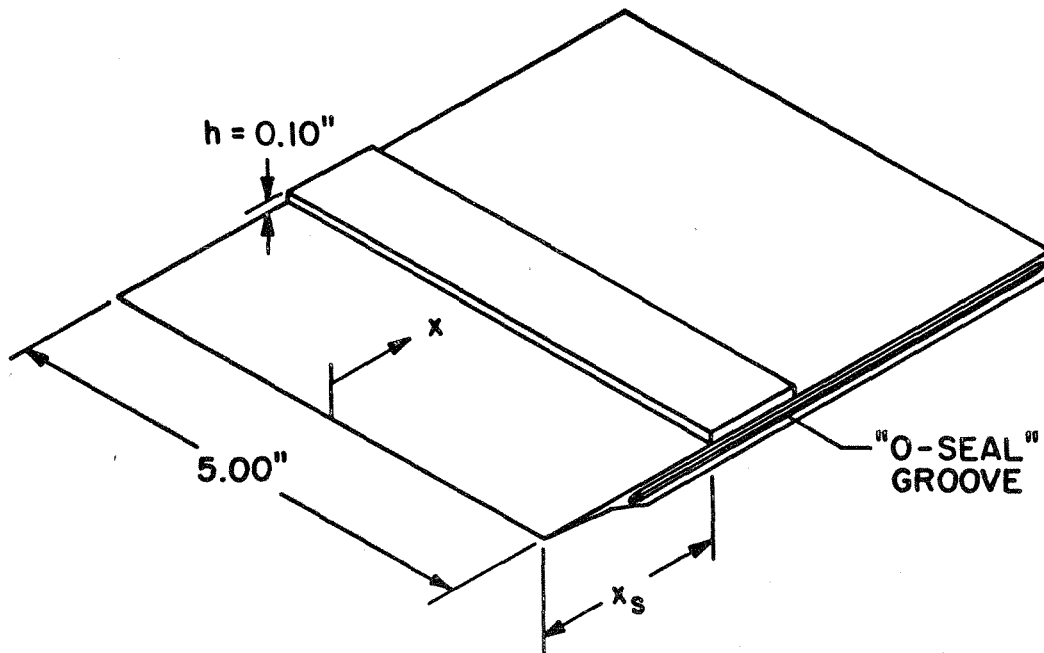
Figure 7. Liquid Nitrogen Pumping System.



MODEL X-1		MODEL X-3		MODEL X-4	
$x_c = 5.0$		$x_c = 3.0$		$x_c = 2.0$	
$L_R = 5.5$		$L_R = 4.0$		$L_R = 4.0$	
STATIC PRESSURE ORIFICES		STATIC PRESSURE ORIFICES		STATIC PRESSURE ORIFICES	
x	s	x	s	x	s
2.00	0.25	1.235	0.75	1.00	0.75
2.50	0.50	1.485	1.50	1.23	1.50
3.00	1.00	1.735	2.25	1.48	2.25
3.25	1.50	1.860	3.00	1.73	3.00
3.50	2.00	1.985		1.86	
3.75	2.50	2.110		2.00	
4.00	3.00	2.235			
4.50	3.50	2.360			
5.00	4.00	2.485			
	4.50	2.610			
	5.00	2.735			
	5.25	3.000			

\*In addition to the  $\phi$  pressure orifices, Model X-1 had 4 off center orifices ( $z = \pm .50''$ ,  $\pm 1.00''$ ) at 5 stations:  $x = 2.50$ ,  $4.00$  and  $s = .50$ ,  $2.50$ ,  $4.00$ .

Figure 8. Wind Tunnel Models X-1, -3 and -4.



MODEL S-1  
STATIC PRESSURE  
ORIFICES

$x =$	.750	} $x_s = 2''$	} $x_s = 5''$	
	.875			
	1.000			
	1.125			
	1.250			
	1.375			
	1.500			
	1.650			
	1.800			
	2.000			
	2.200			
	2.400			
	2.600			
	2.800			
	3.000			
	3.200			
	3.400			
	3.600			
	3.800			
	4.000			
	4.200			
	4.400			
	4.600			
	4.800			

Figure 9. Wind Tunnel Model S-1.

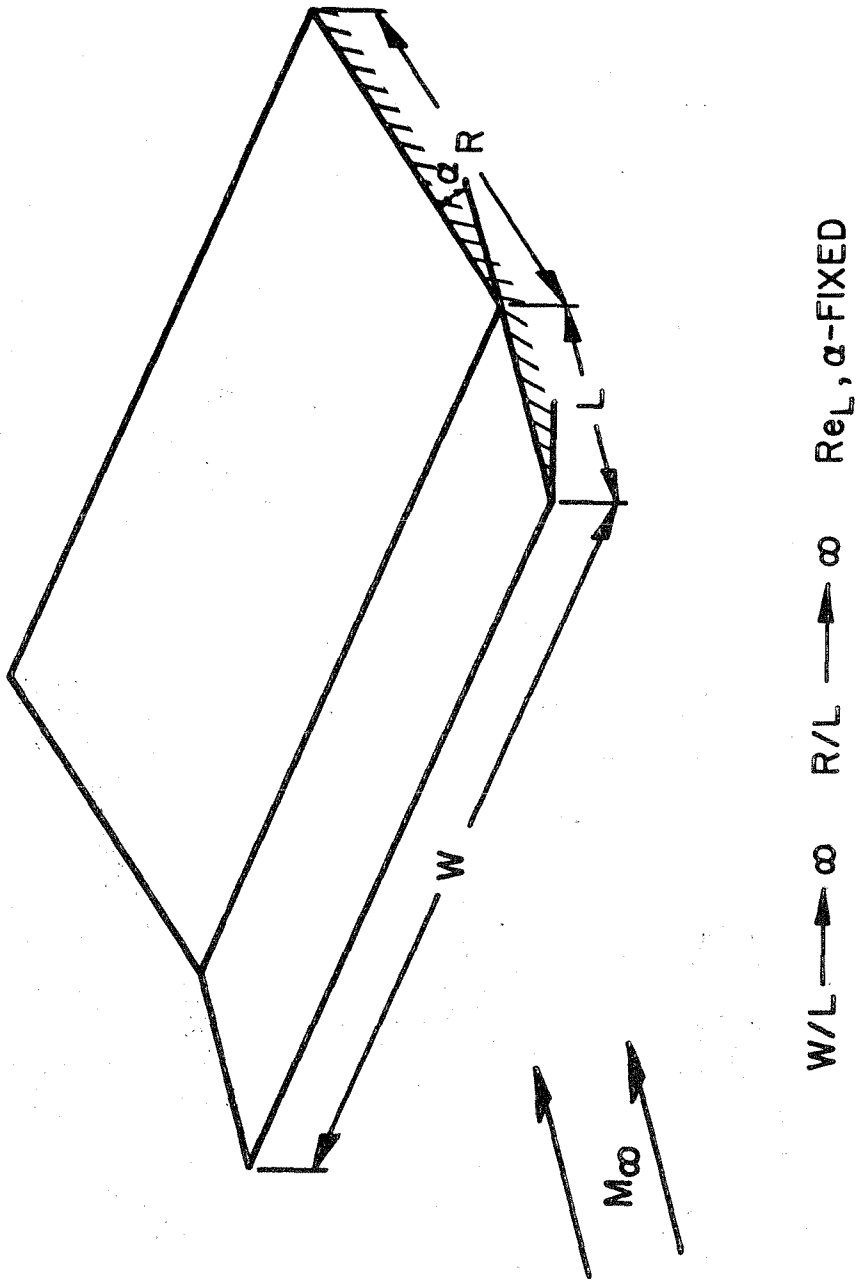


Figure 10. Idealized Geometric Configuration.

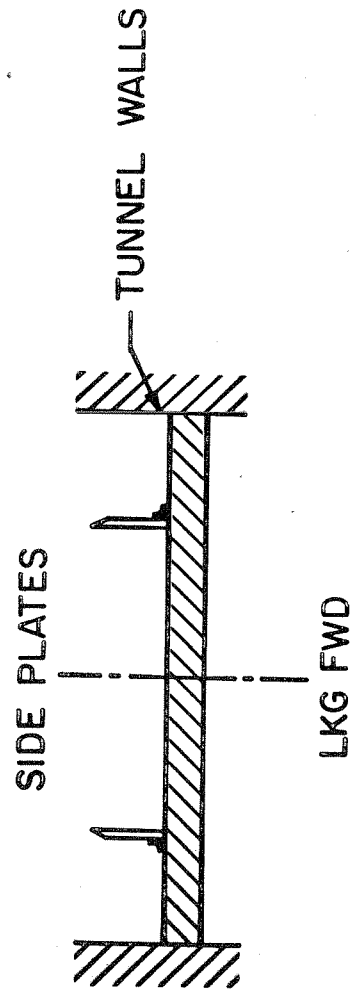
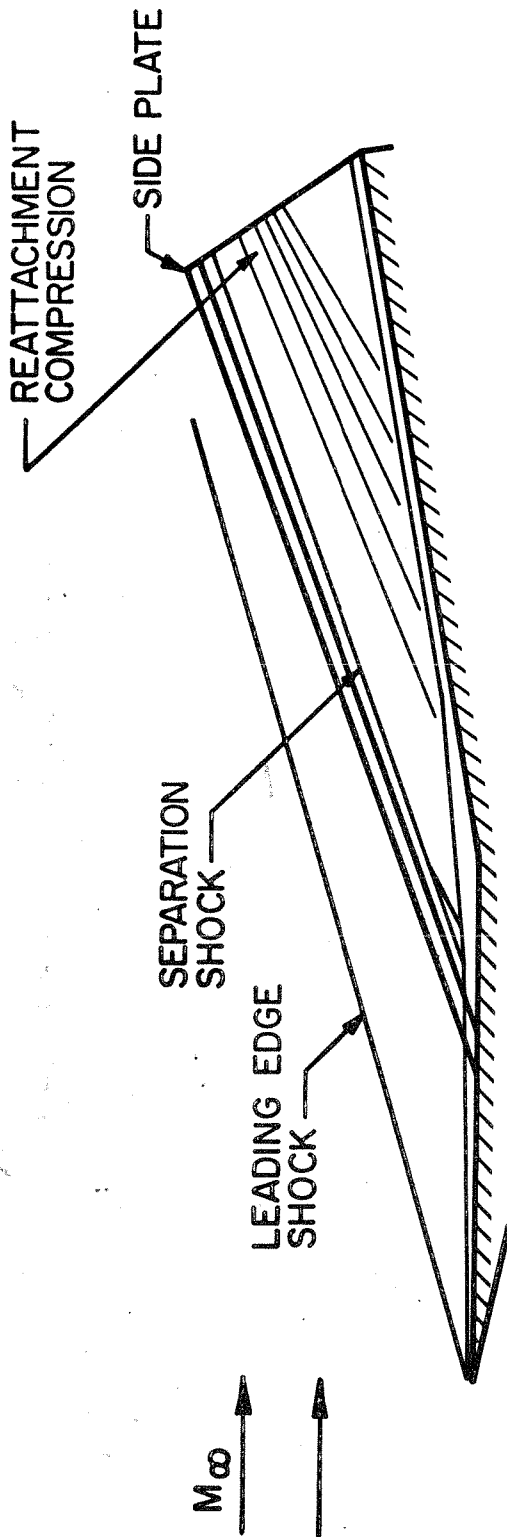


Figure 11. Side Plate Configuration.





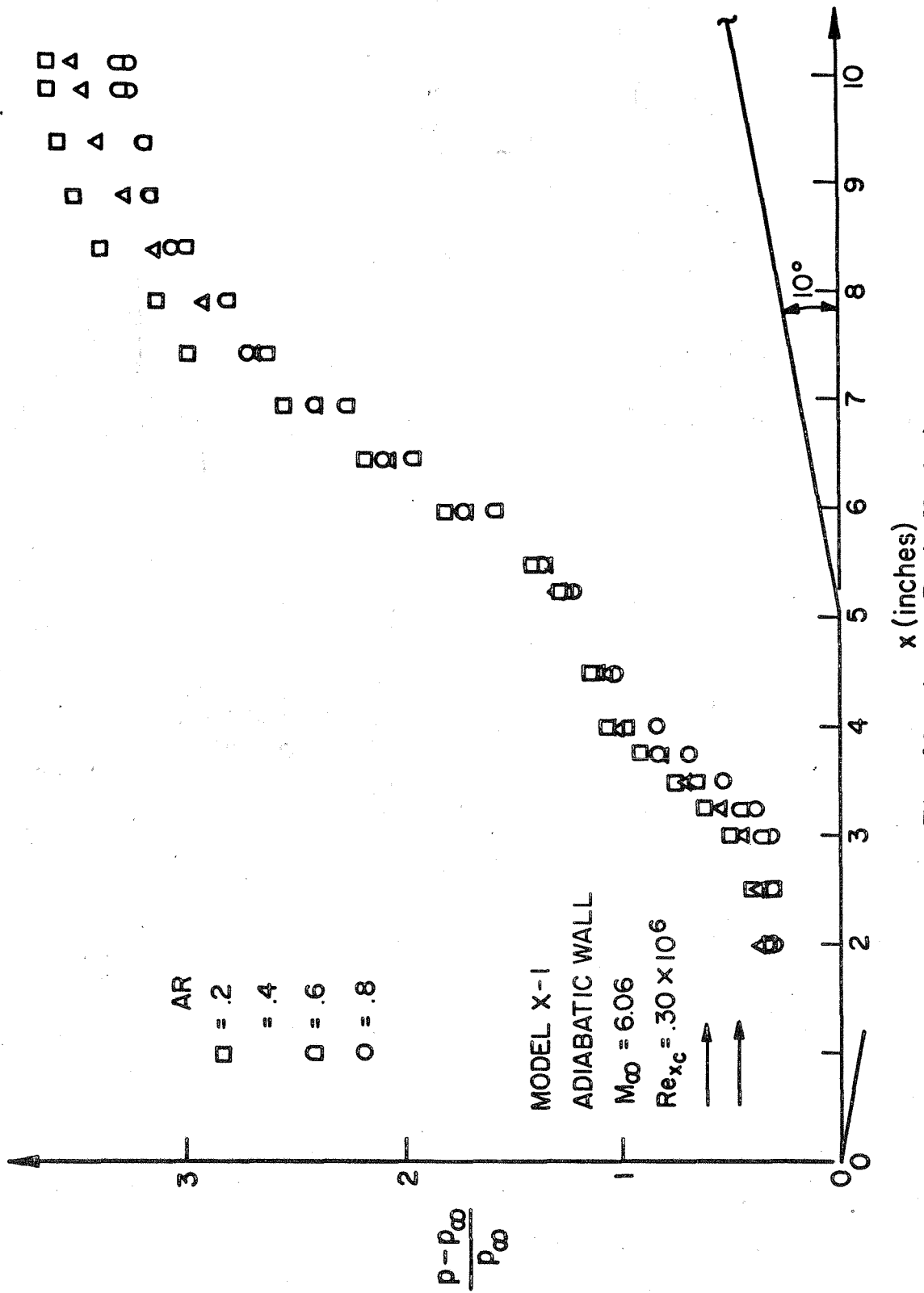


Fig. 13. Aspect Ratio Variation

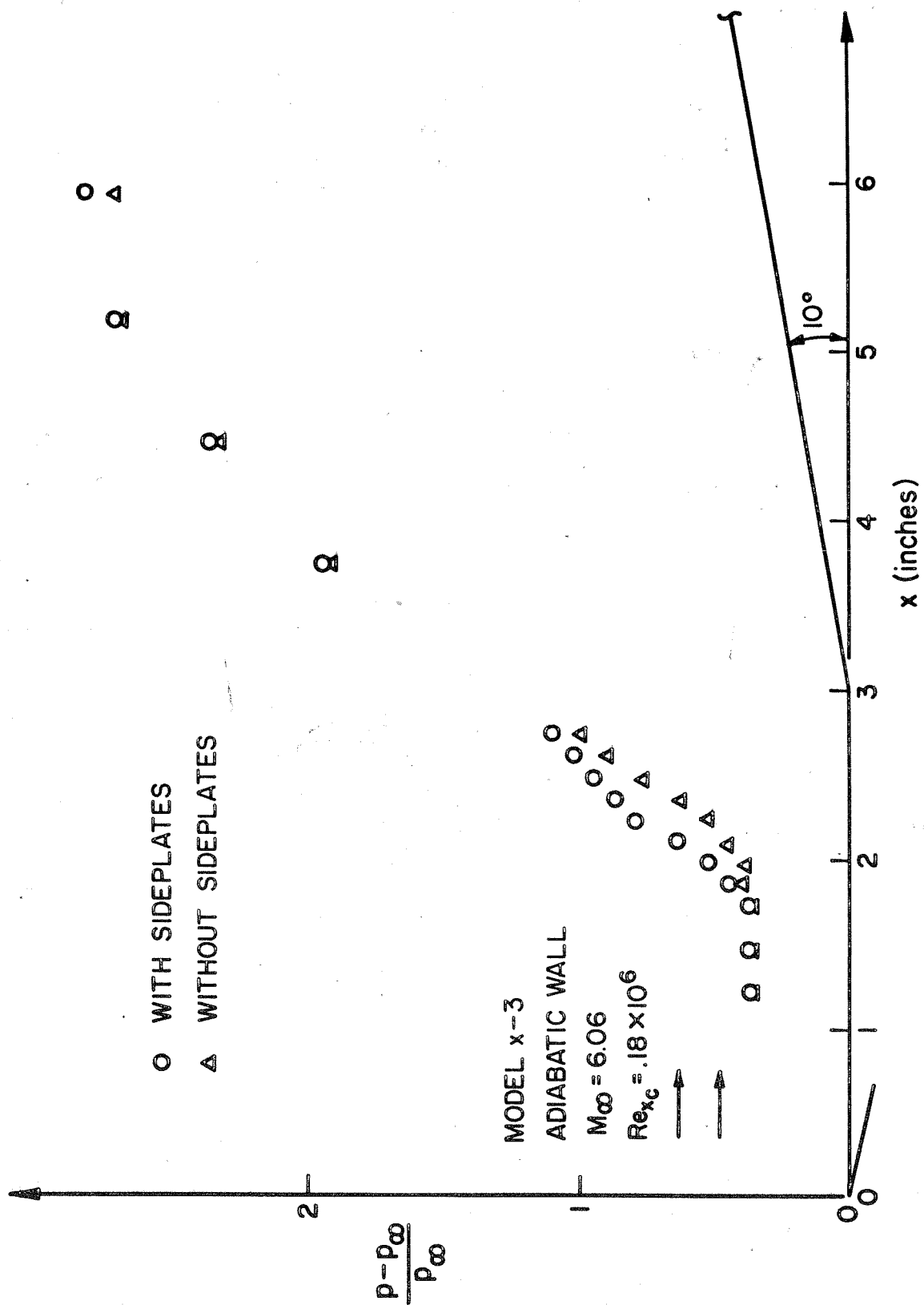


Figure 14. Effect of Side Plate Removal.

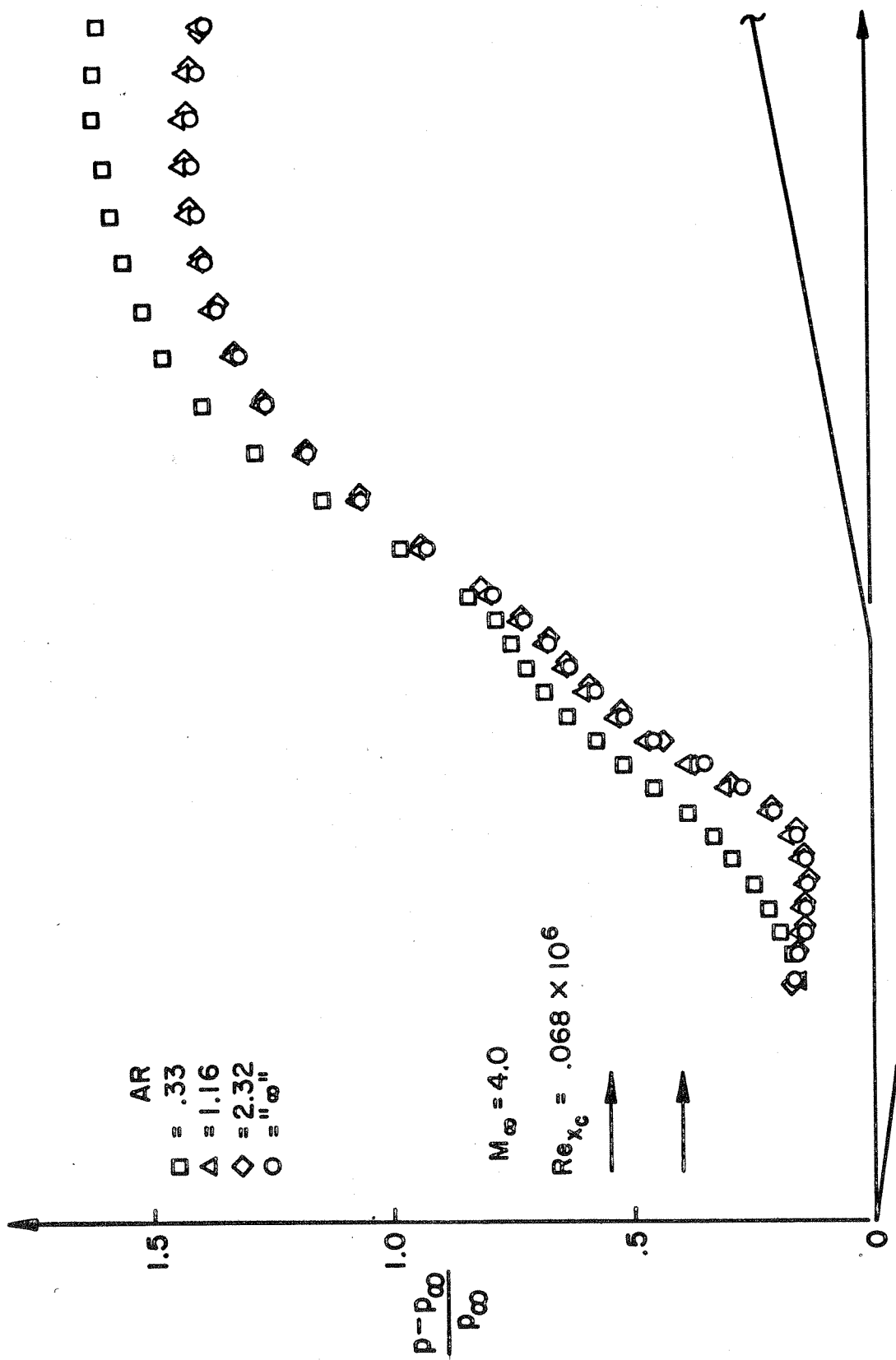


Figure 15. Side Plate Disturbance to Otherwise Clean Flow (Model AR-1).

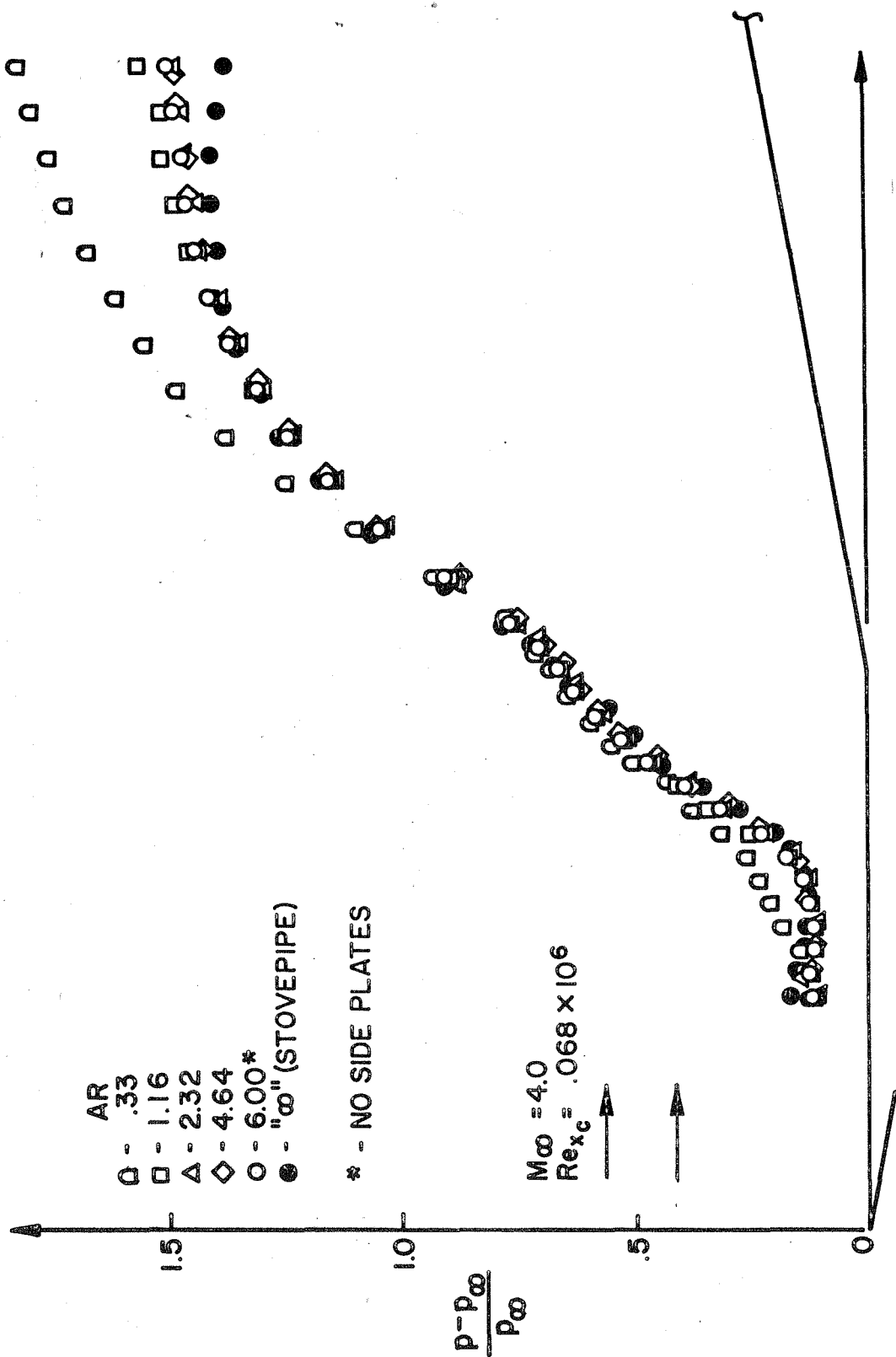


Figure 16. Aspect Ratio Variation on "Two-dimensional" Model AR-2 with Comparison to "Stovepipe," Model AR-2.

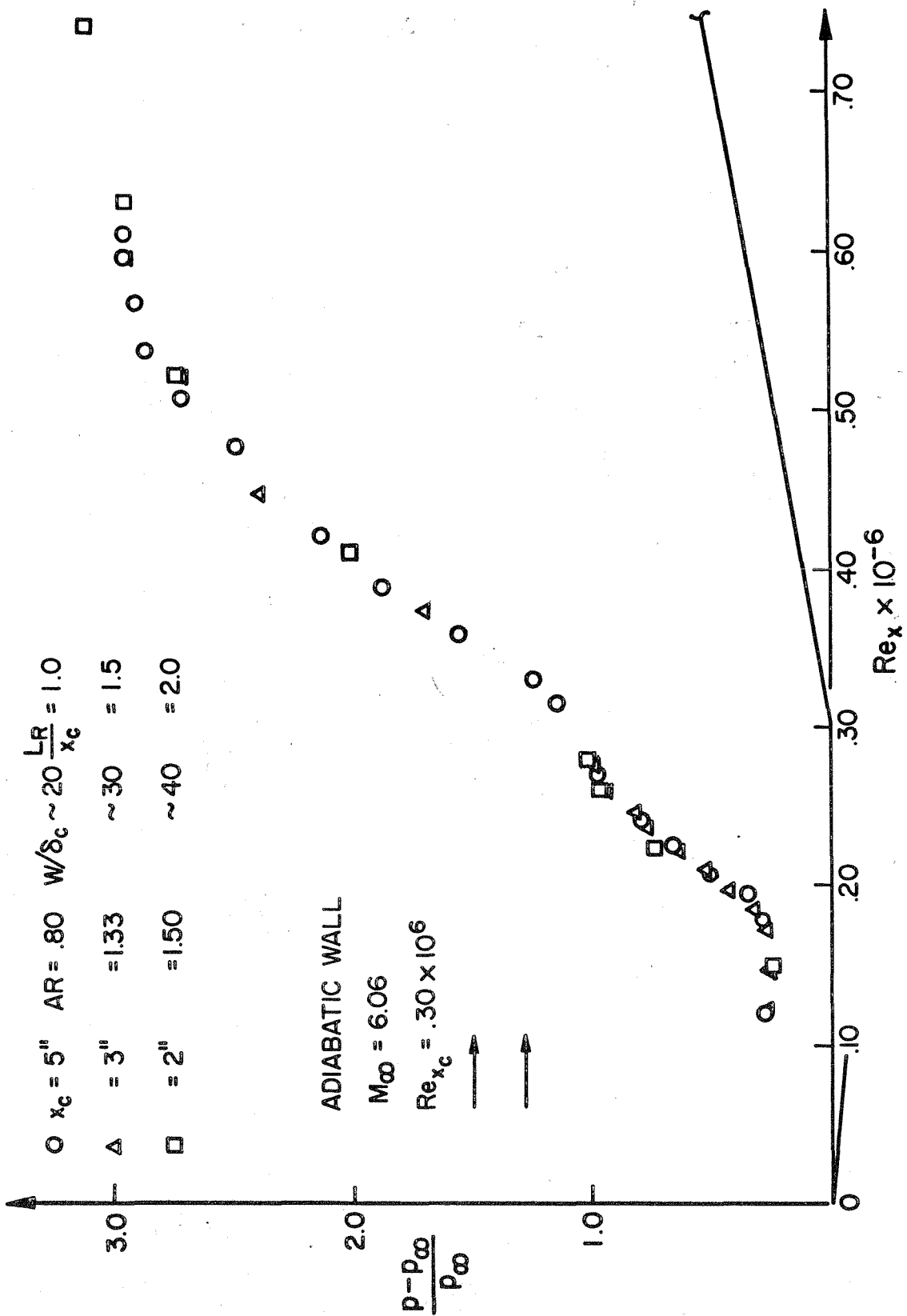


Figure 17. Reynolds Number Correlation.

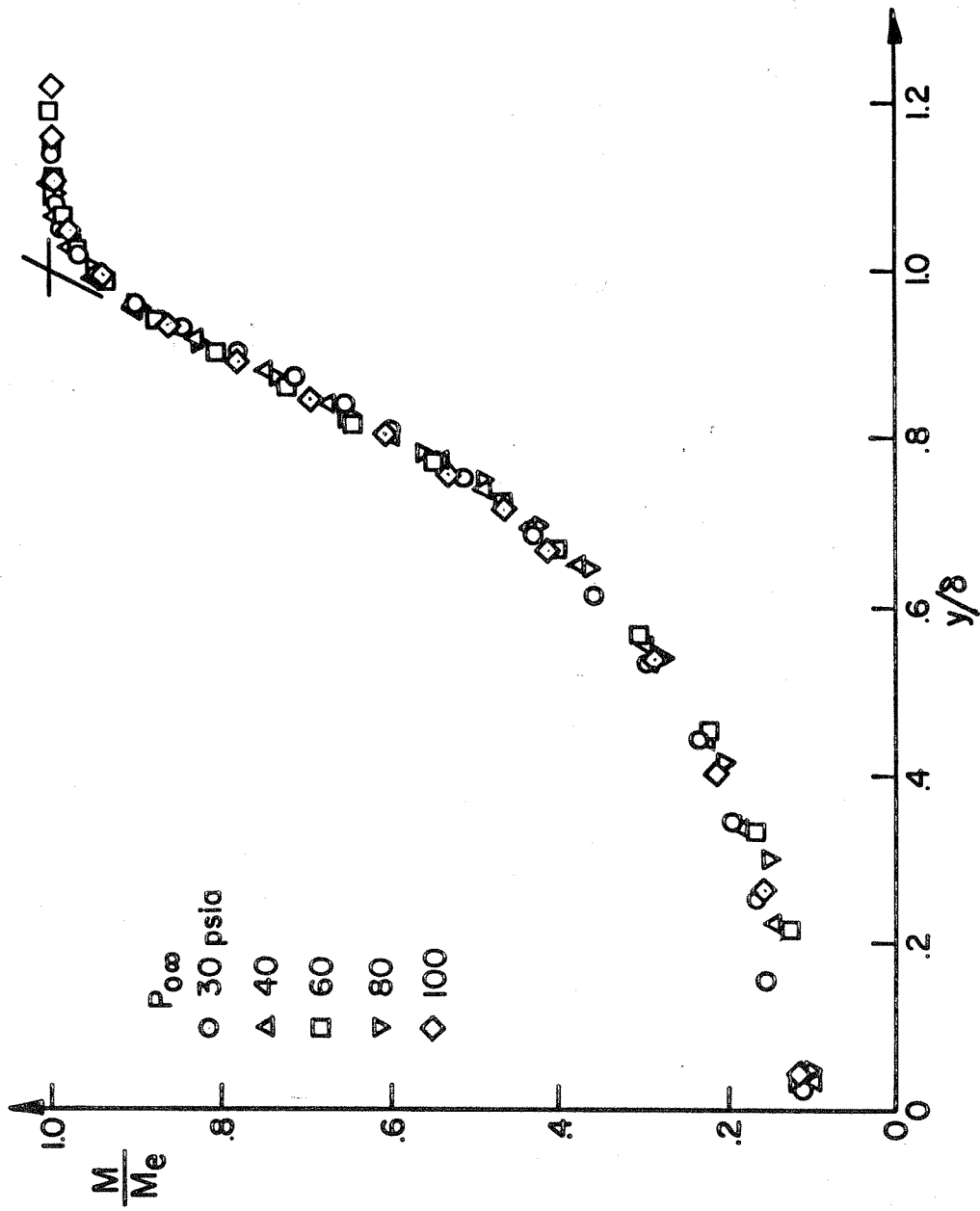


Figure 18. Pre-separation Mach Number Profiles (Adiabatic Wall).

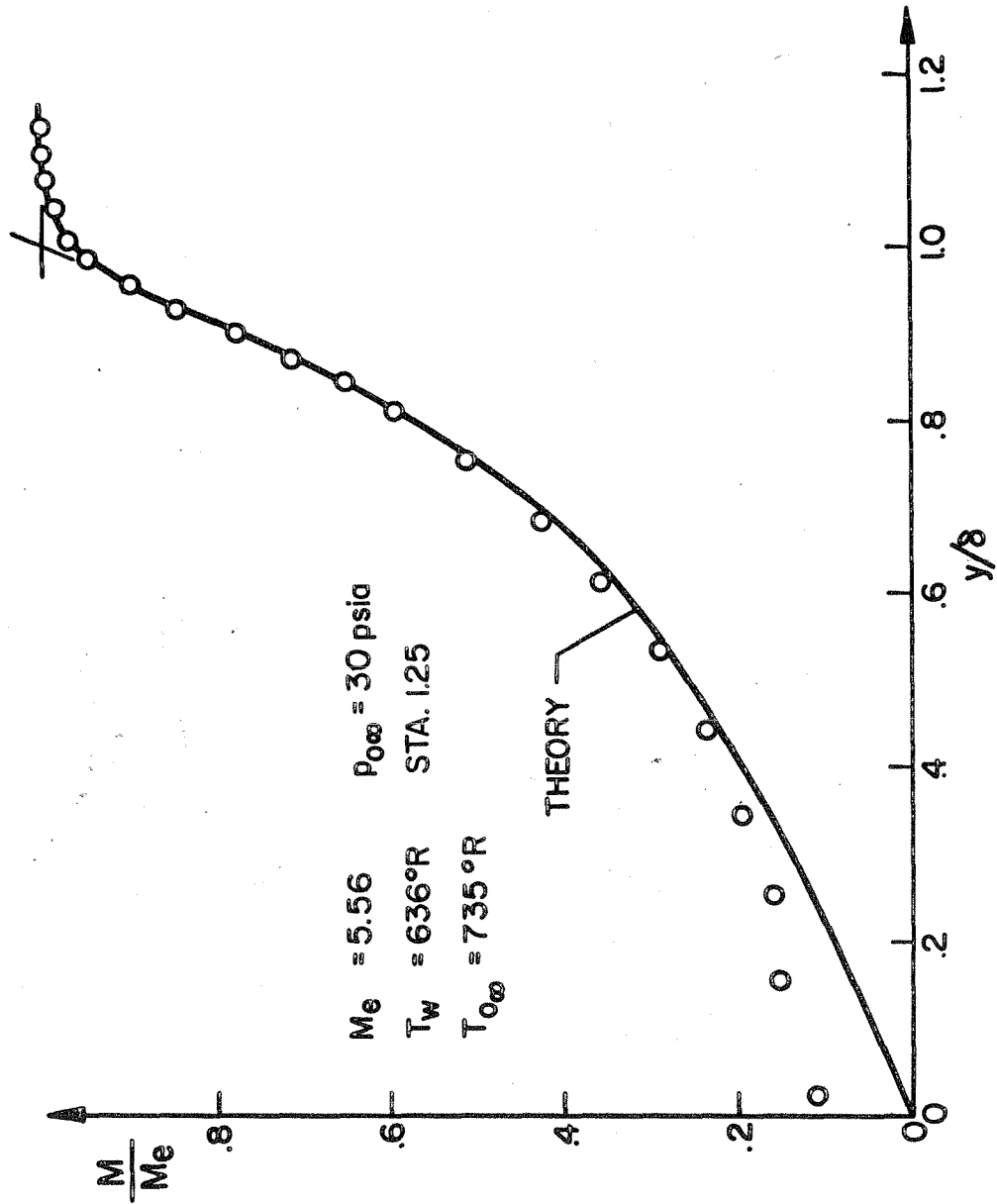


Figure 19. Pre-separation Mach Number Profile Comparison with Theoretical Prediction (Adiabatic Wall).



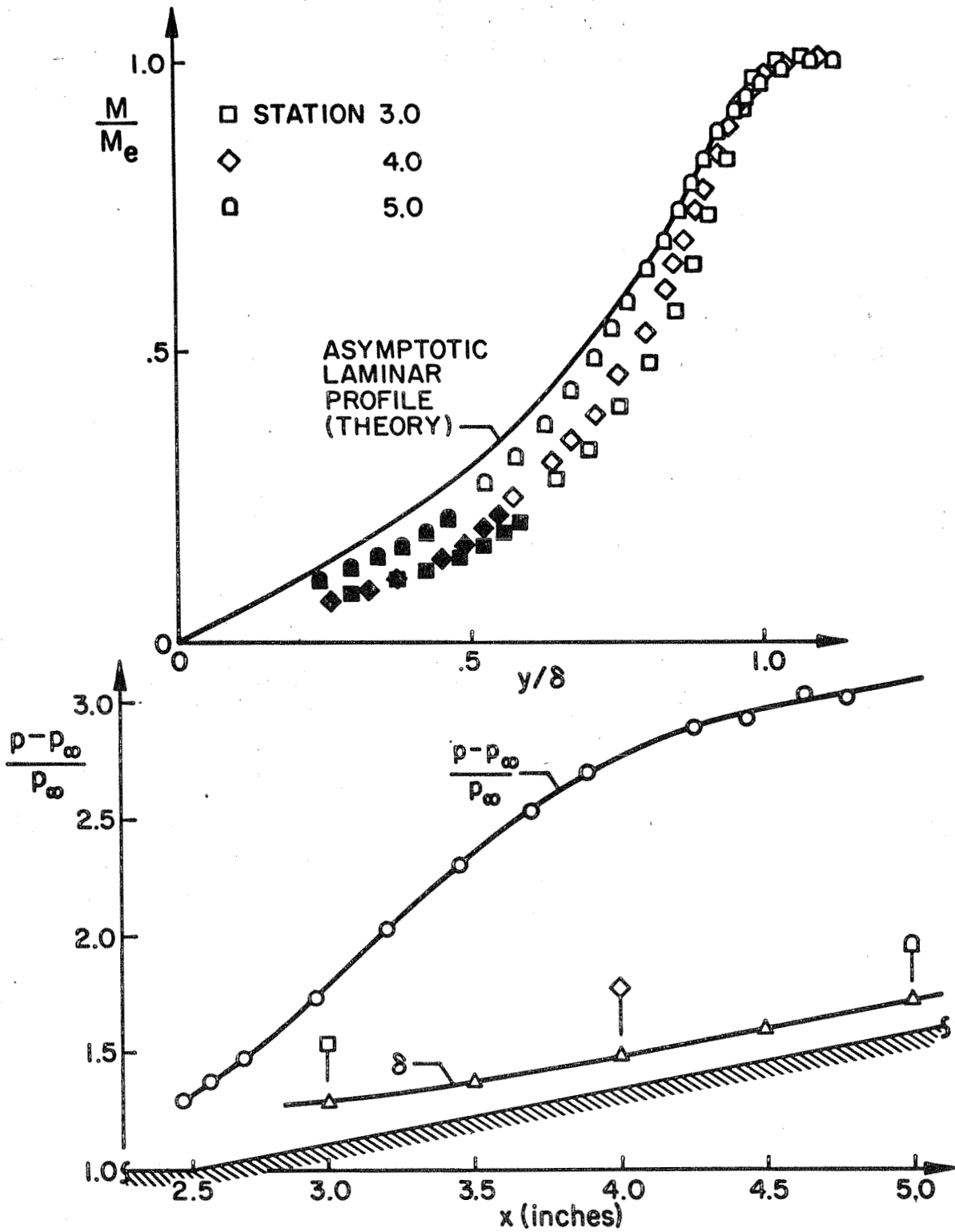


Figure 20. Reattachment Profiles (Adiabatic Wall) at  $Re_{x_c} = .15 \times 10^6$ .

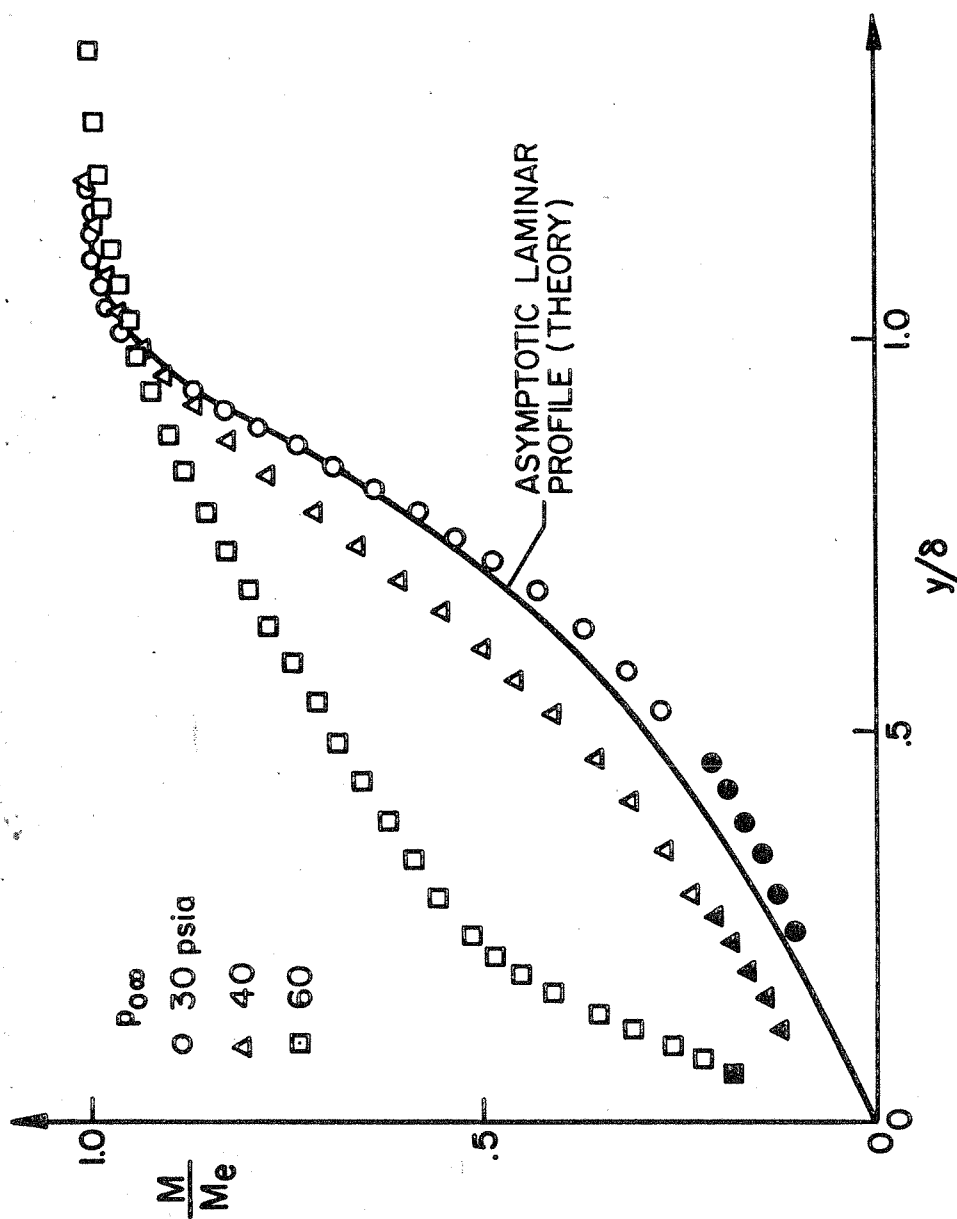


Figure 21. Reattachment Profiles at "Test Station" with Increasing Reynolds Number (Adiabatic Wall).

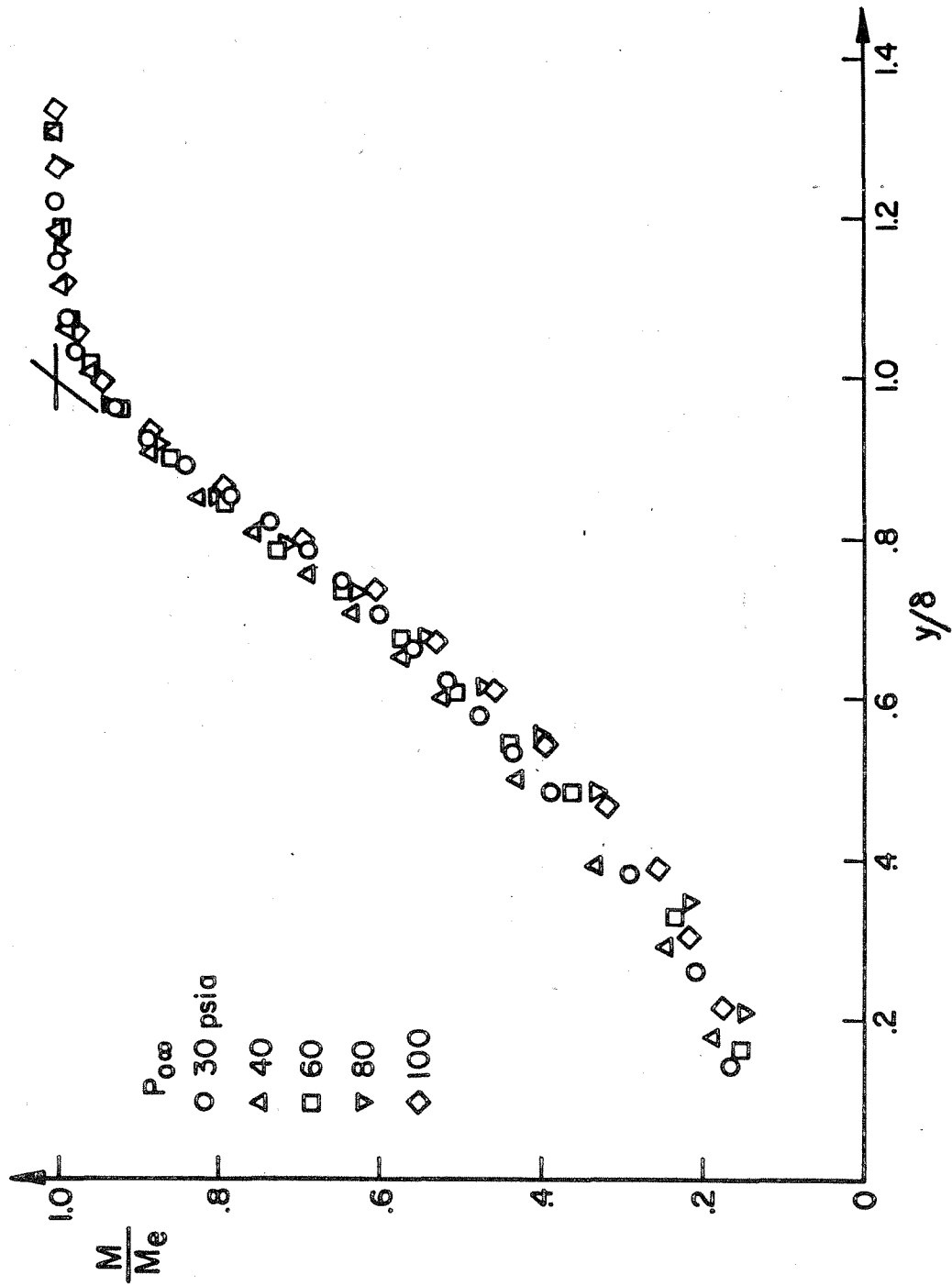


Figure 22. Pre-separation Mach Number Profiles (Cold Wall).

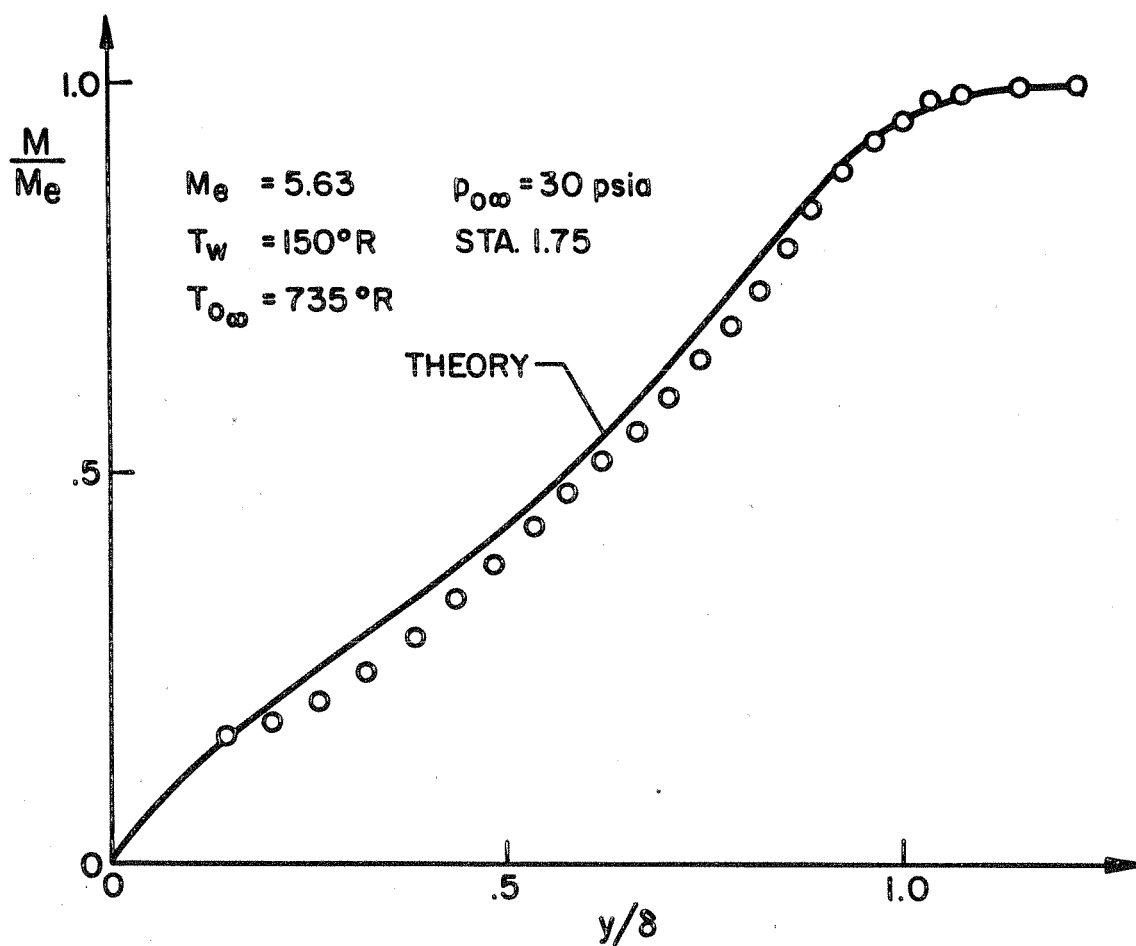


Figure 23. Pre-separation Mach Number Profile Comparison with Theoretical Prediction (Cold Wall).

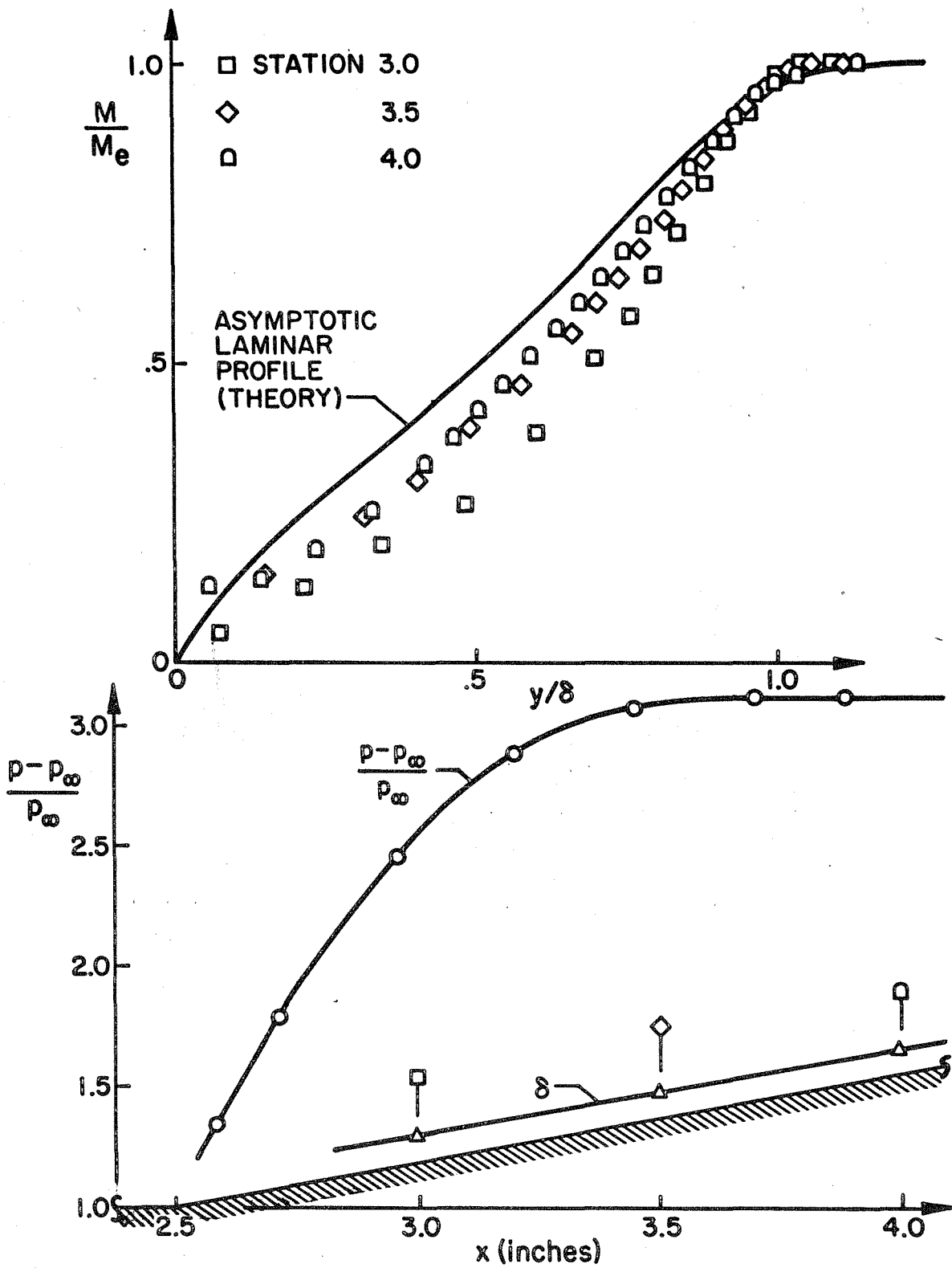


Figure 24. Reattachment Profiles (Cold Wall) at  $Re_{x_c} = .15 \times 10^6$ .

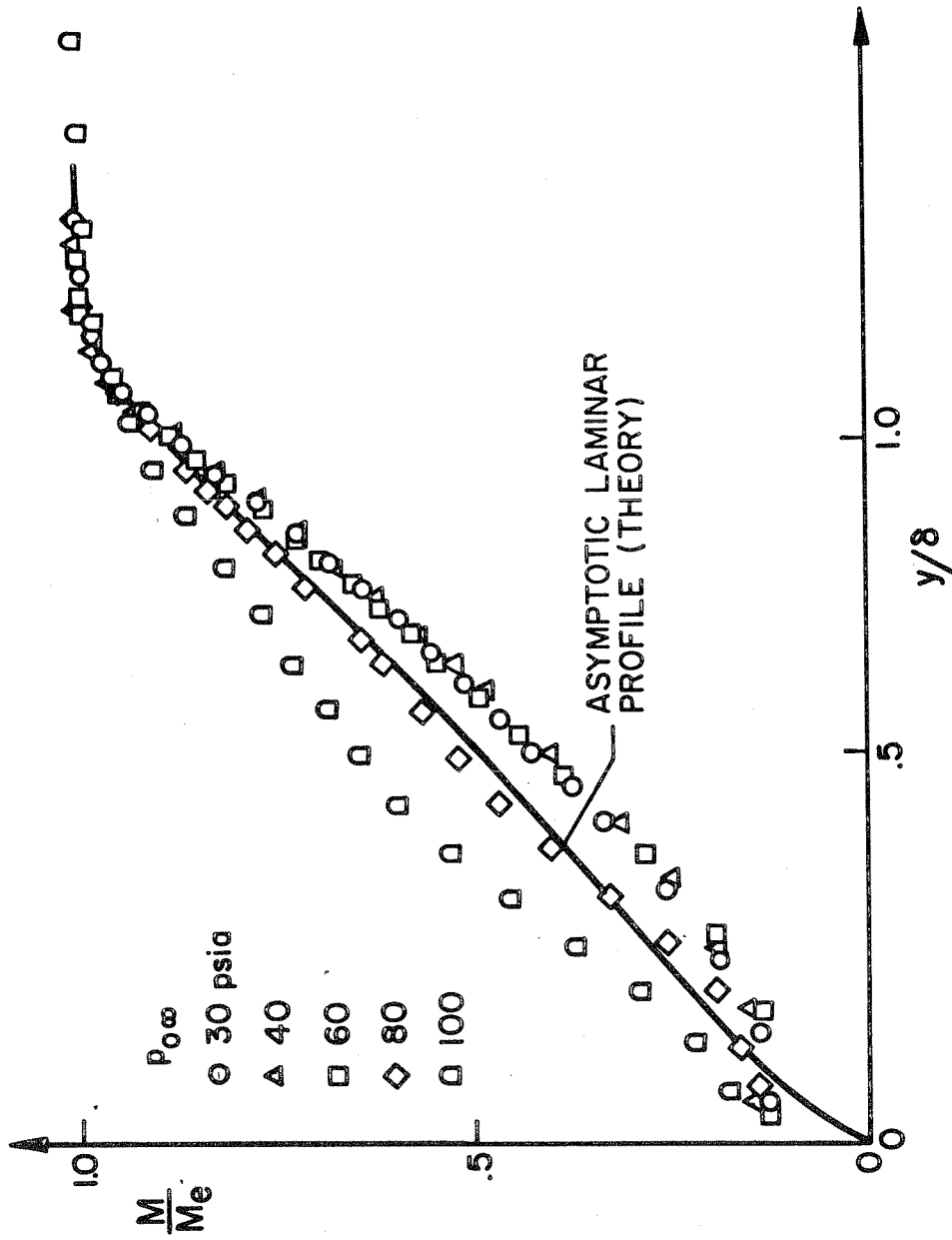


Figure 25. Reattachment Profiles at "Test Station" with Increasing Reynolds Number (Cold Wall).

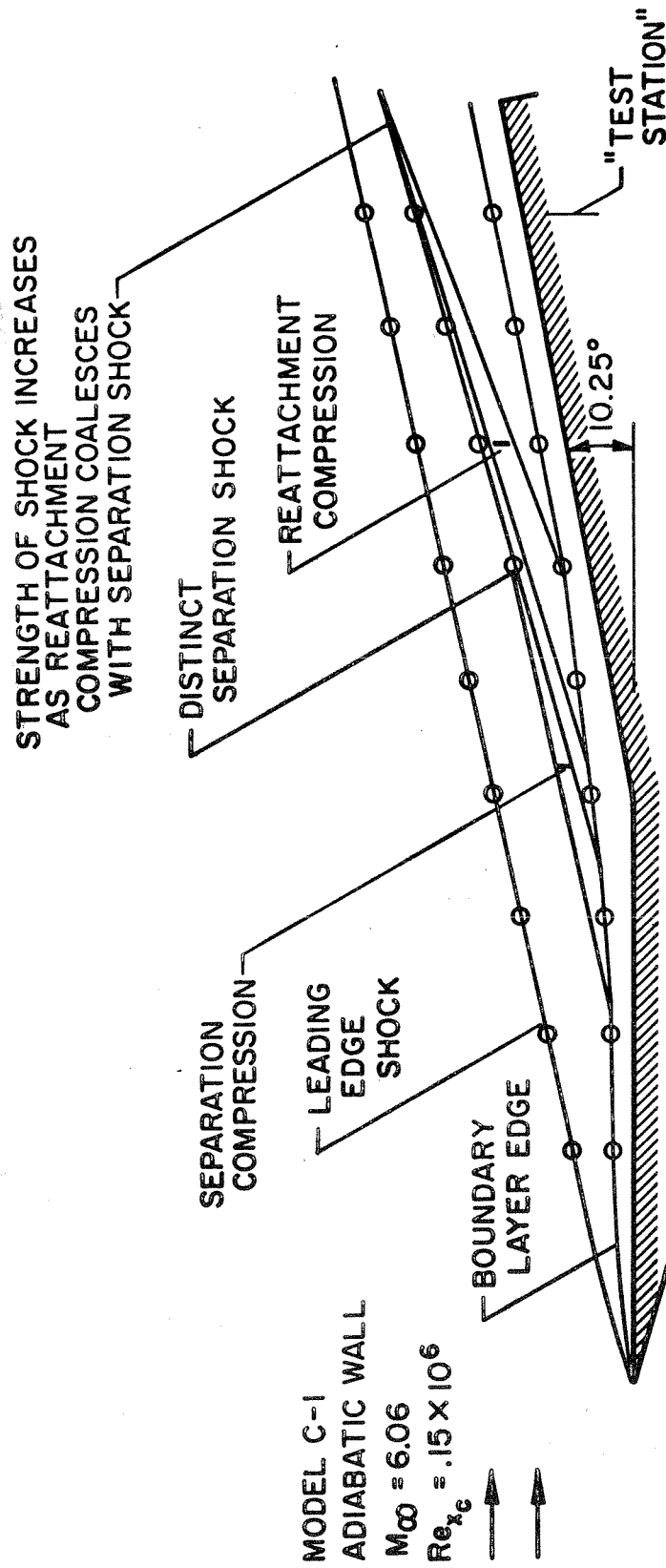


Figure 26. External Flow Field (Adiabatic Wall).

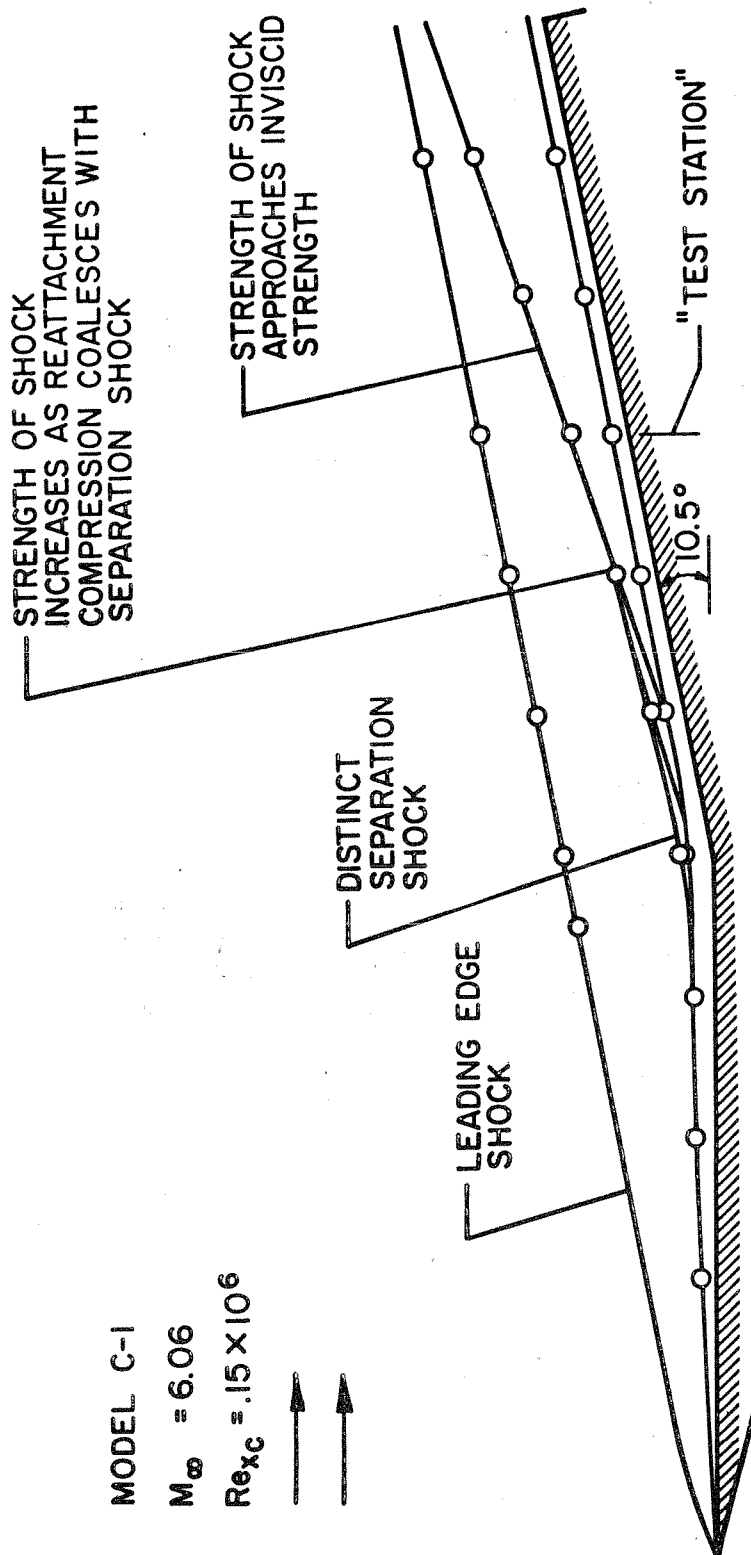


Figure 27. External Flow Field (Cold Wall).



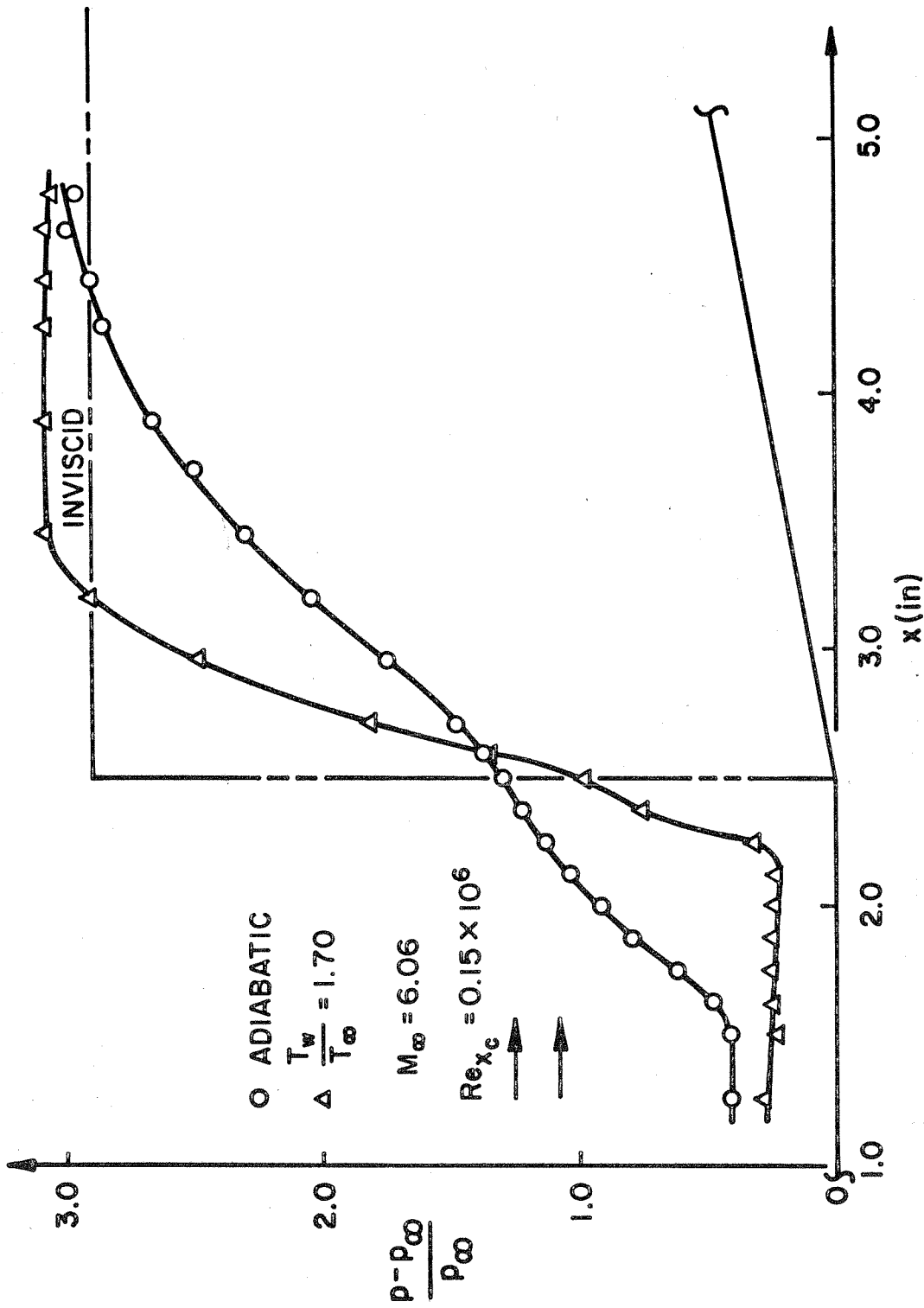


Figure 28. Effect of Cooling on Overall Laminar Boundary Layer Separation.

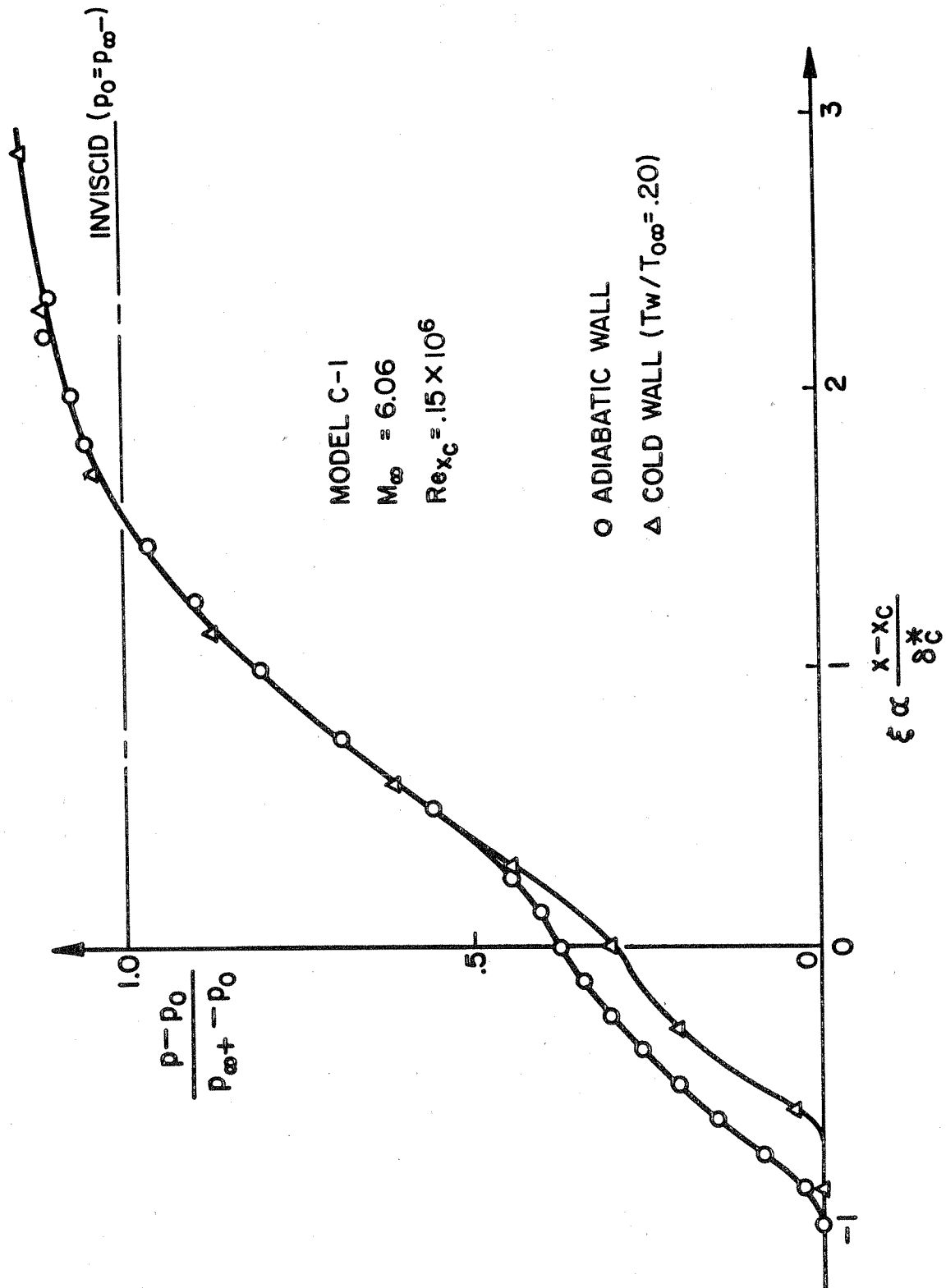


Figure 29. Effect of Cooling Beyond Initial Pressure Level and Boundary Layer Scaling.

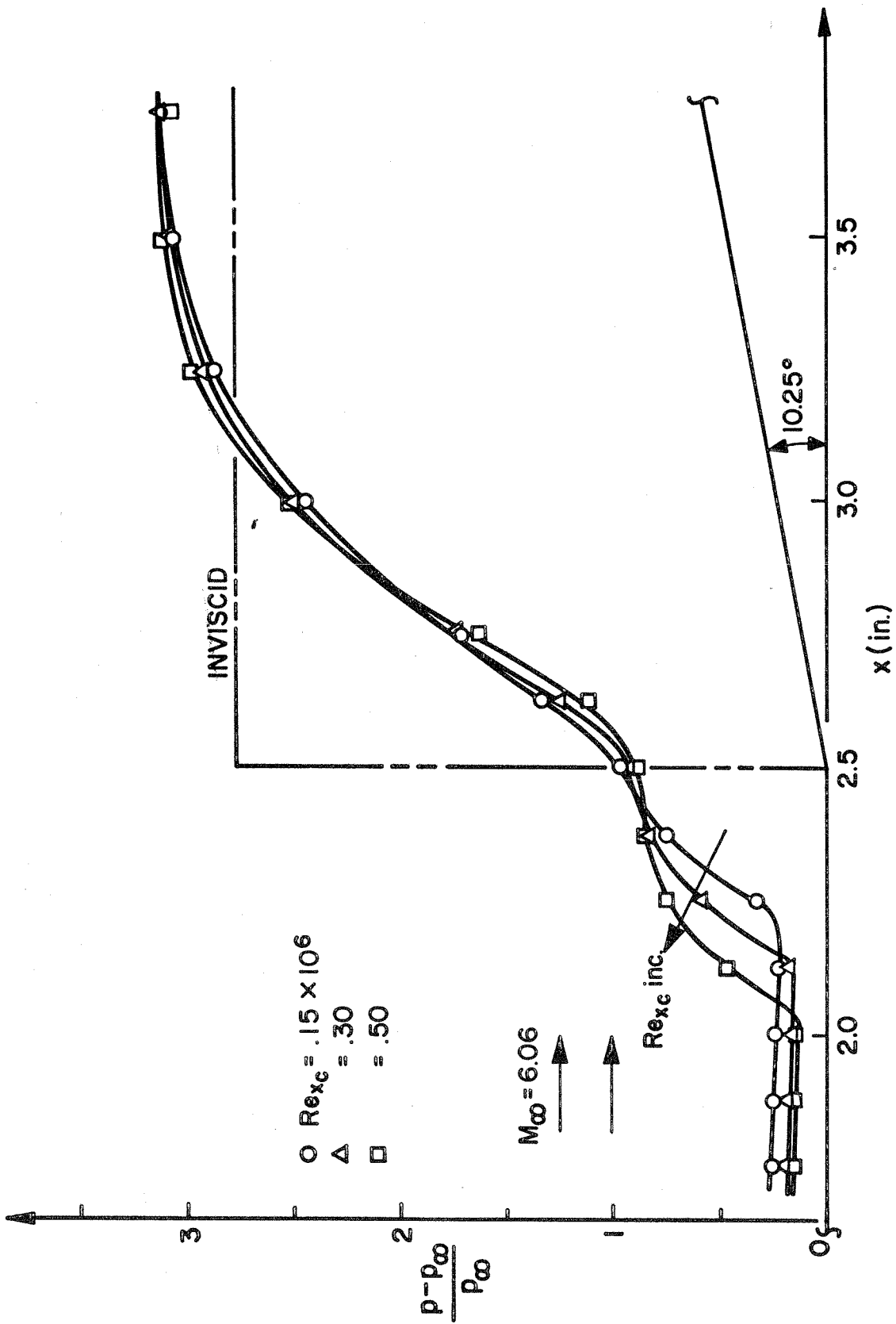


Figure 30. Reynolds Number Dependence (Laminar Flow).

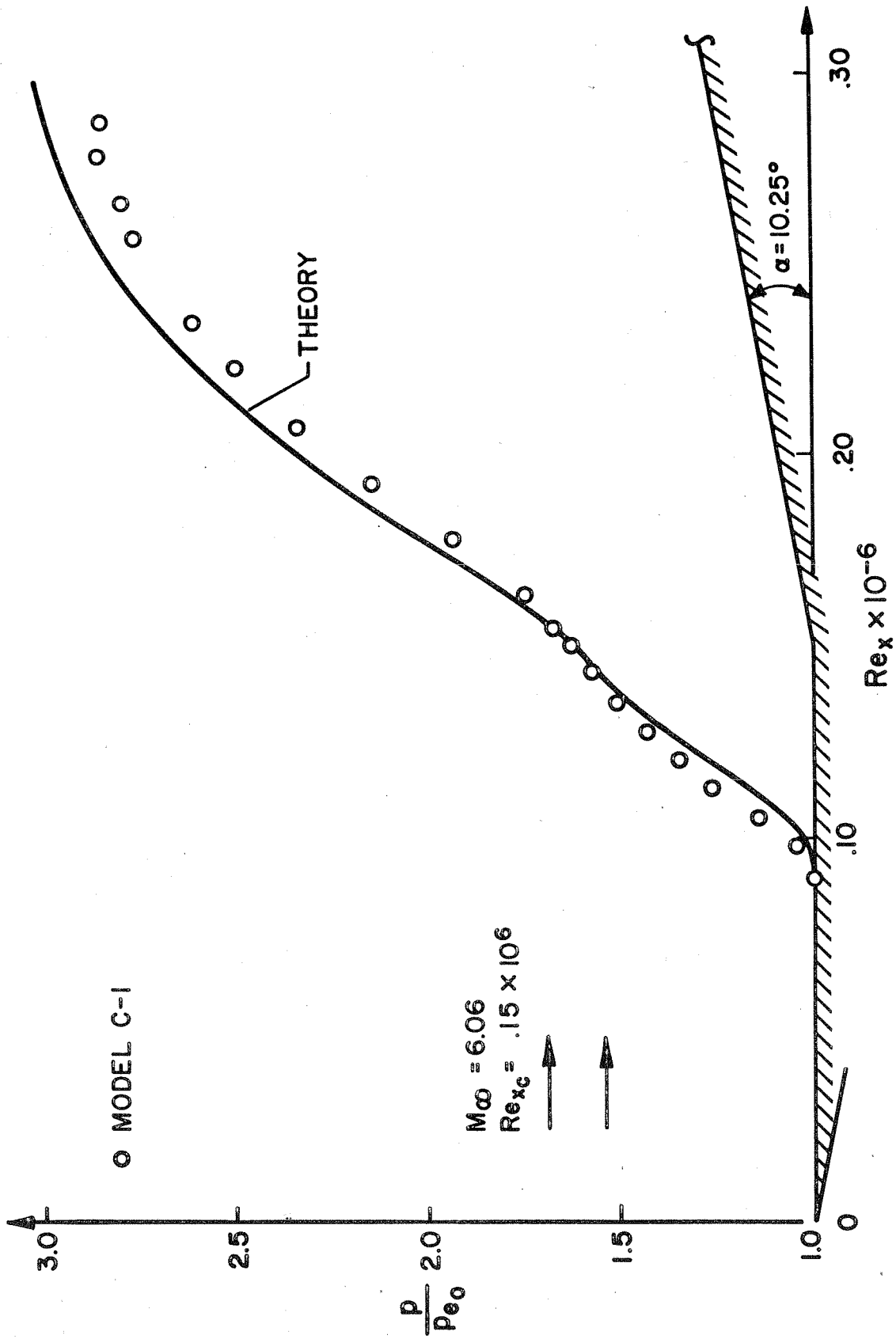


Figure 31. Comparison of Experimental Pressure Distribution with Shock Wave-Boundary Layer Interaction Theory.

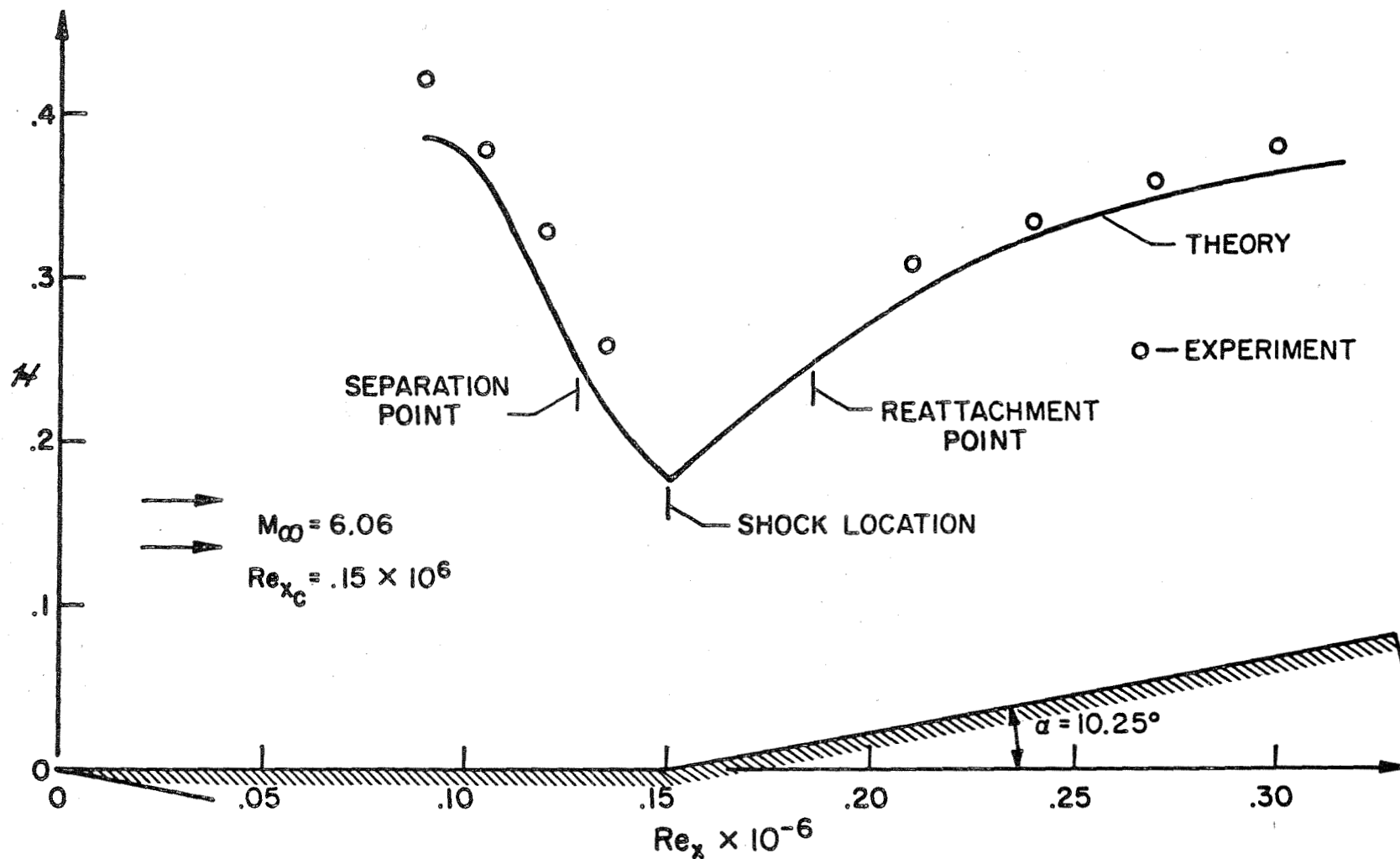


Figure 32. Comparison of Experimental Form Factor,  $H$ , with Shock Wave-Boundary Layer Interaction Theory.

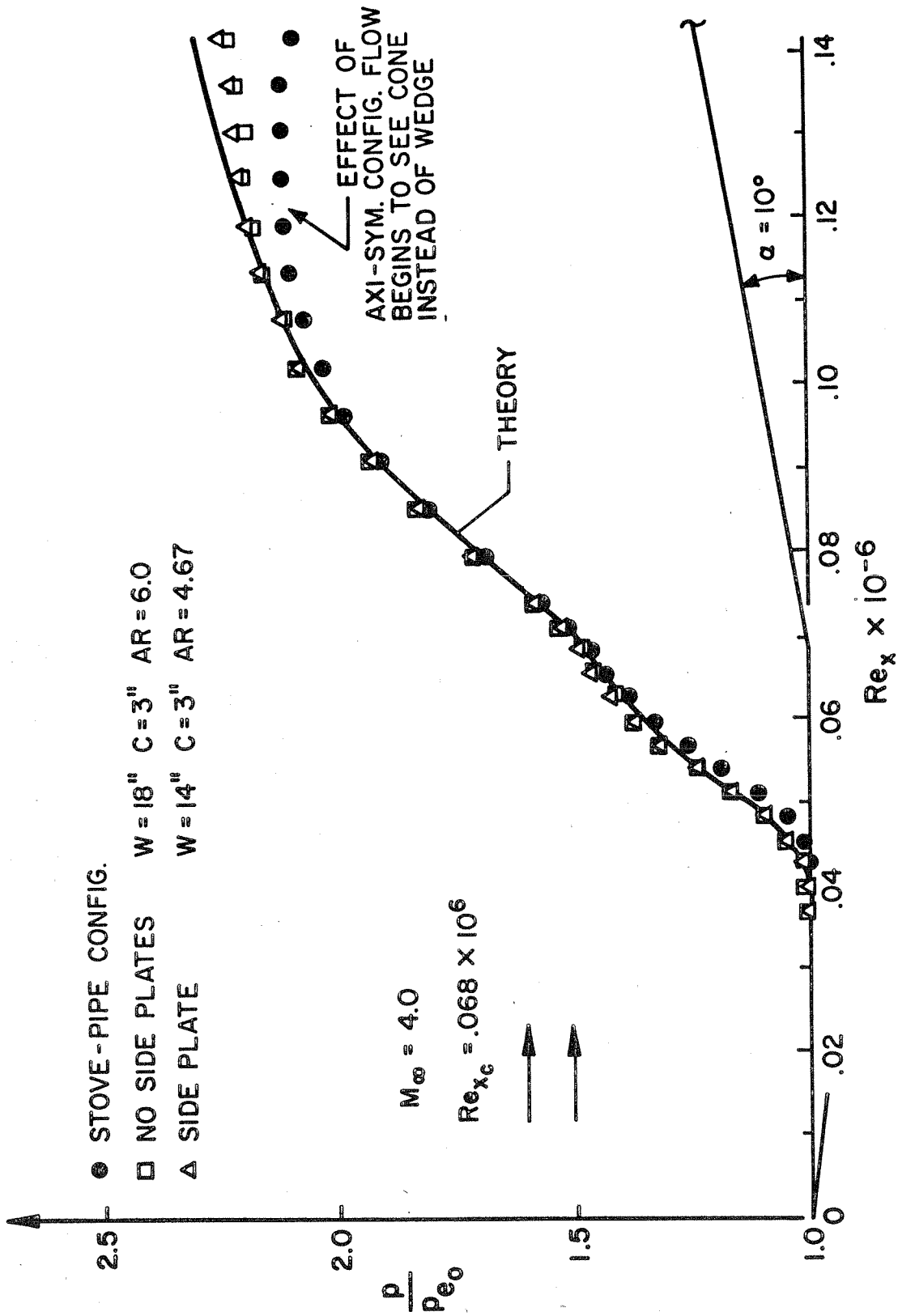


Figure 33. Comparison of Experimental Pressure Distribution with Shock Wave-Boundary Layer Interaction Theory.

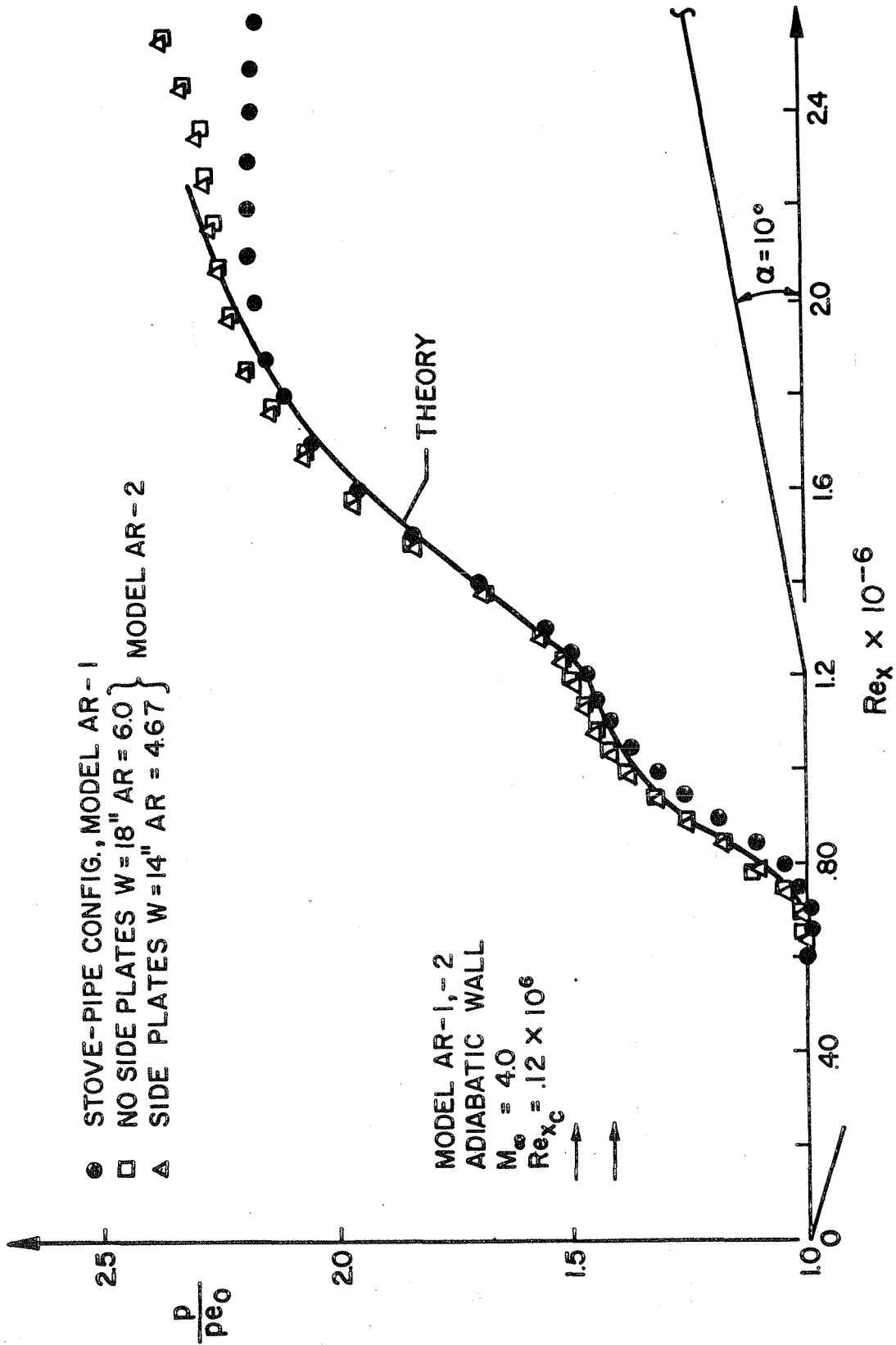


Figure 34. Comparison of Experimental Pressure Distribution with Shock Wave-Boundary Layer Interaction Theory.

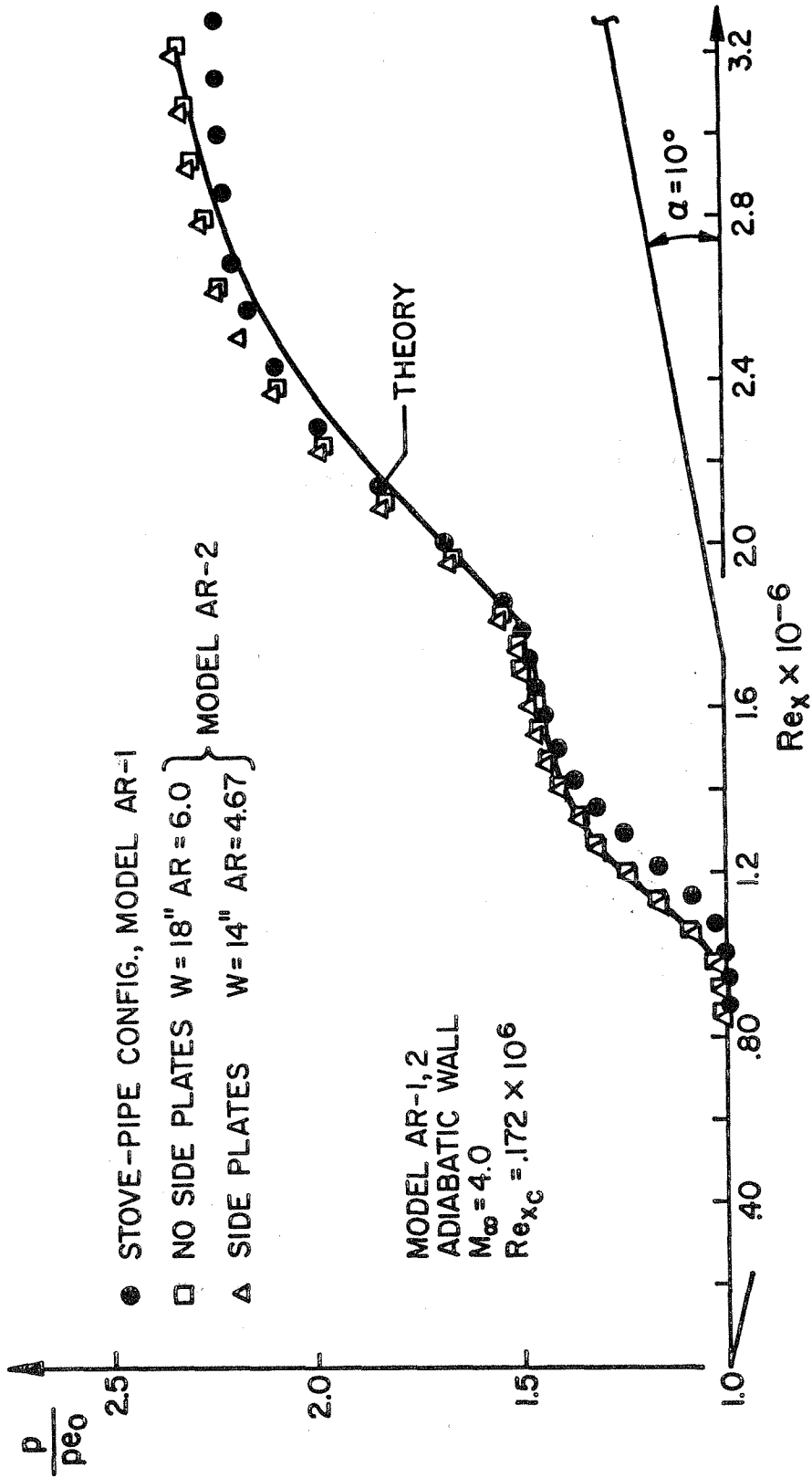


Figure 35. Comparison of Experimental Pressure Distribution with Shock Wave-Boundary Layer Interaction Theory.



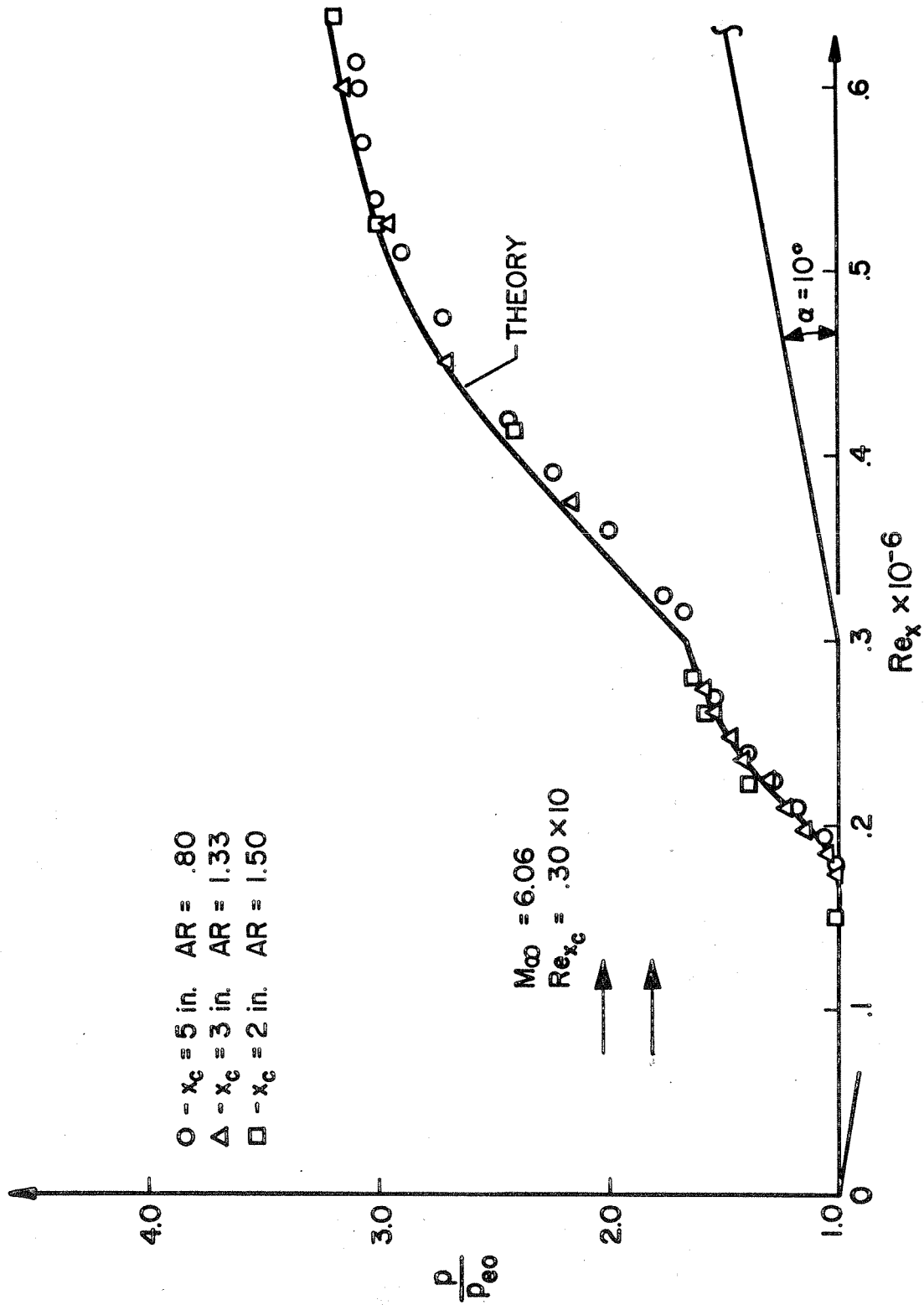


Figure 36. Comparison of Experimental Pressure with Shock Wave - Boundary Layer Interaction Theory, Including Reynolds Number Correlation.

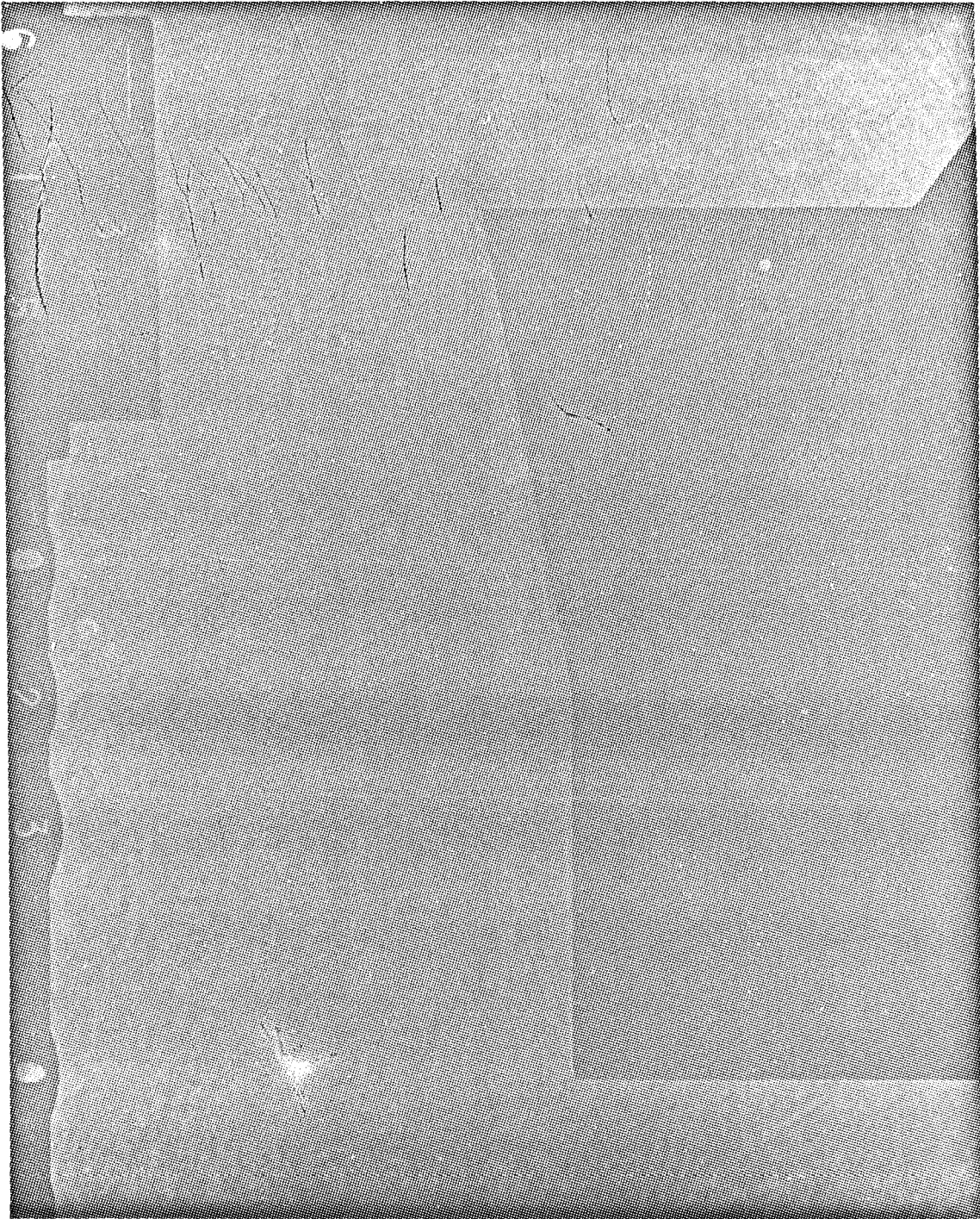


Figure 37. Shadowgraph of Model AR-1 at  $M_\infty = 4.0$ ,  $Re_{x_c} = .27 \times 10^6$ .

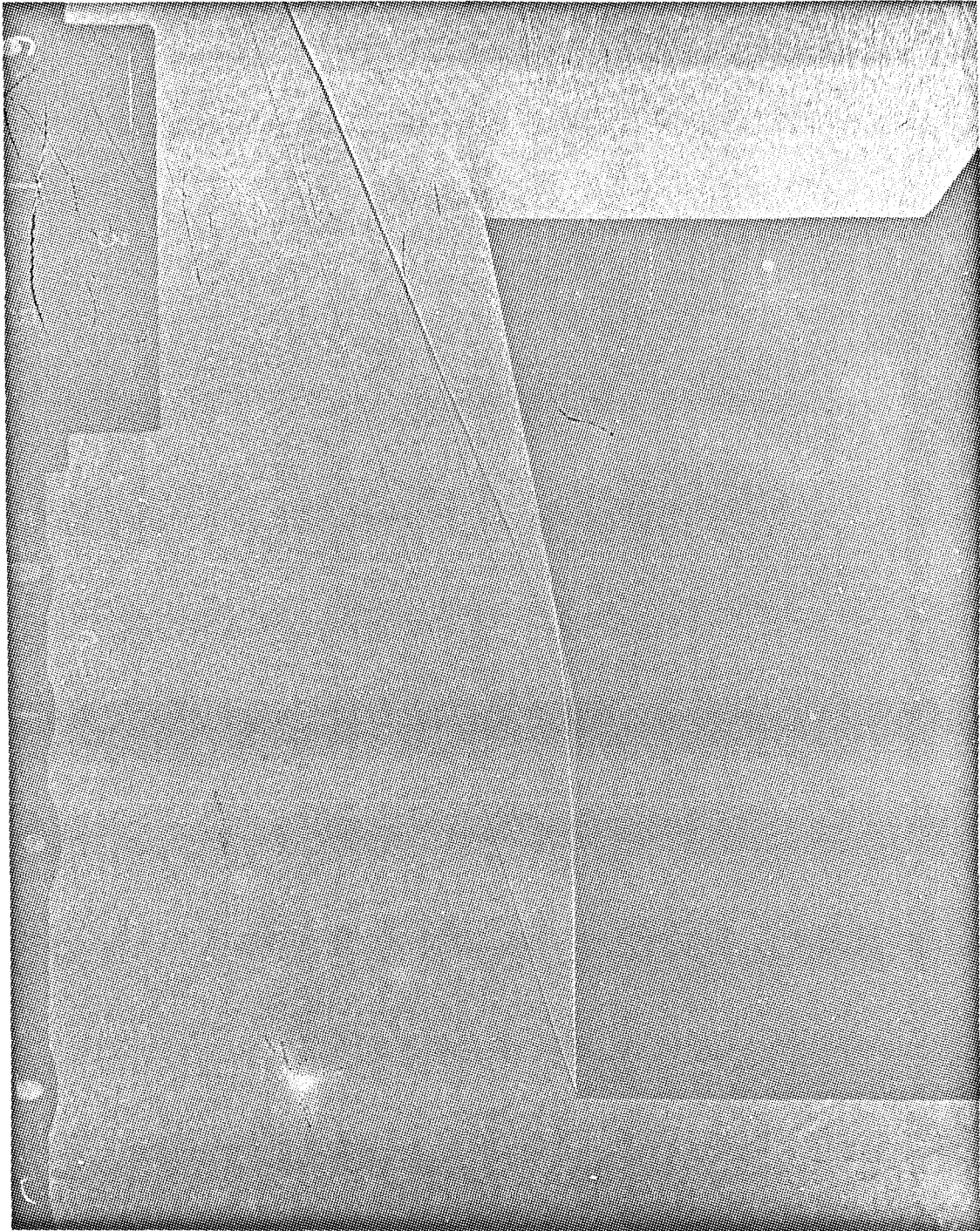


Figure 38. Shadowgraph of Model AR-1 at  $M_\infty = 4.0$ ,  $Re_{x_c} = .89 \times 10^6$ .

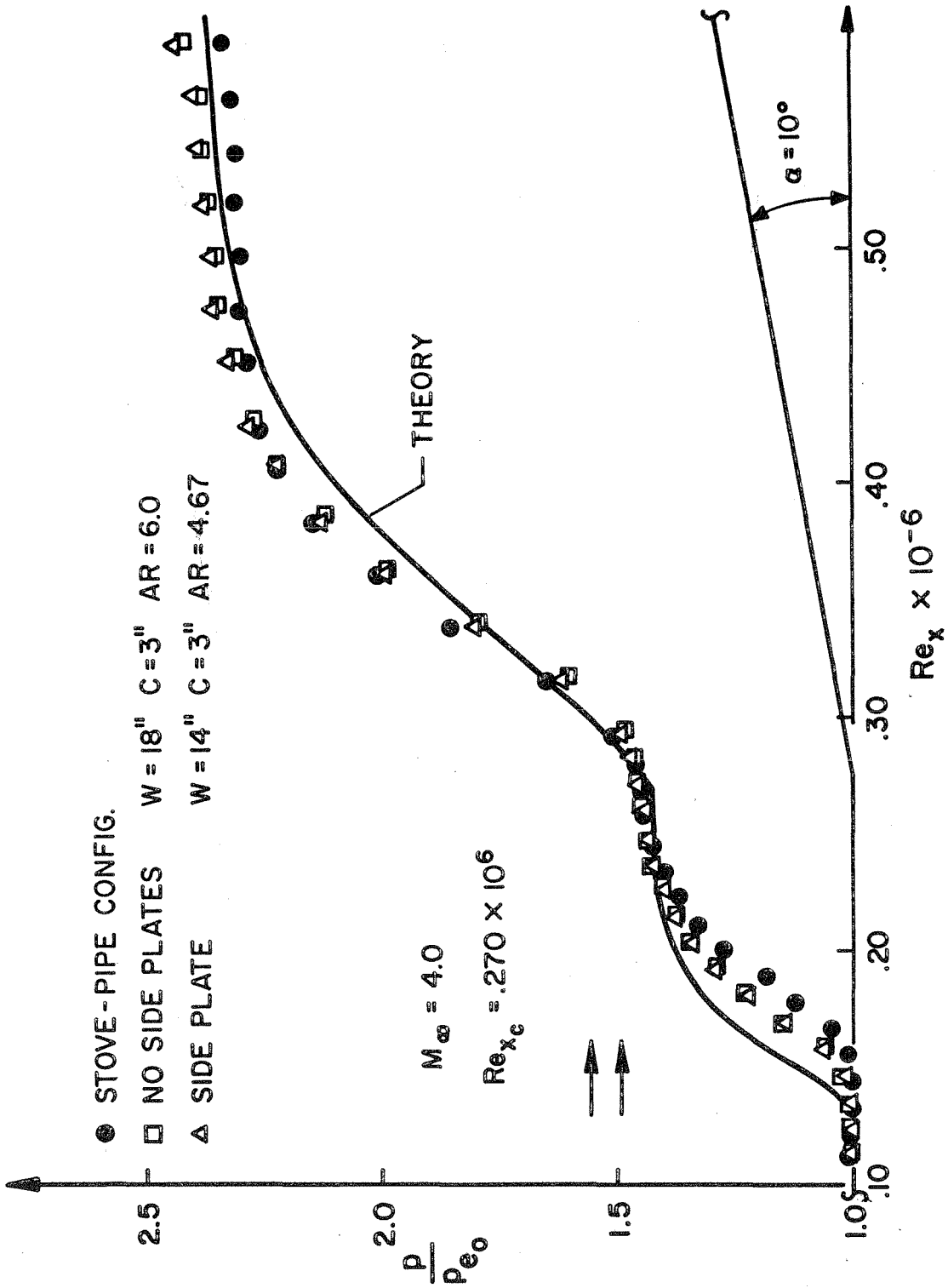


Figure 39. Comparison with Laminar Theory

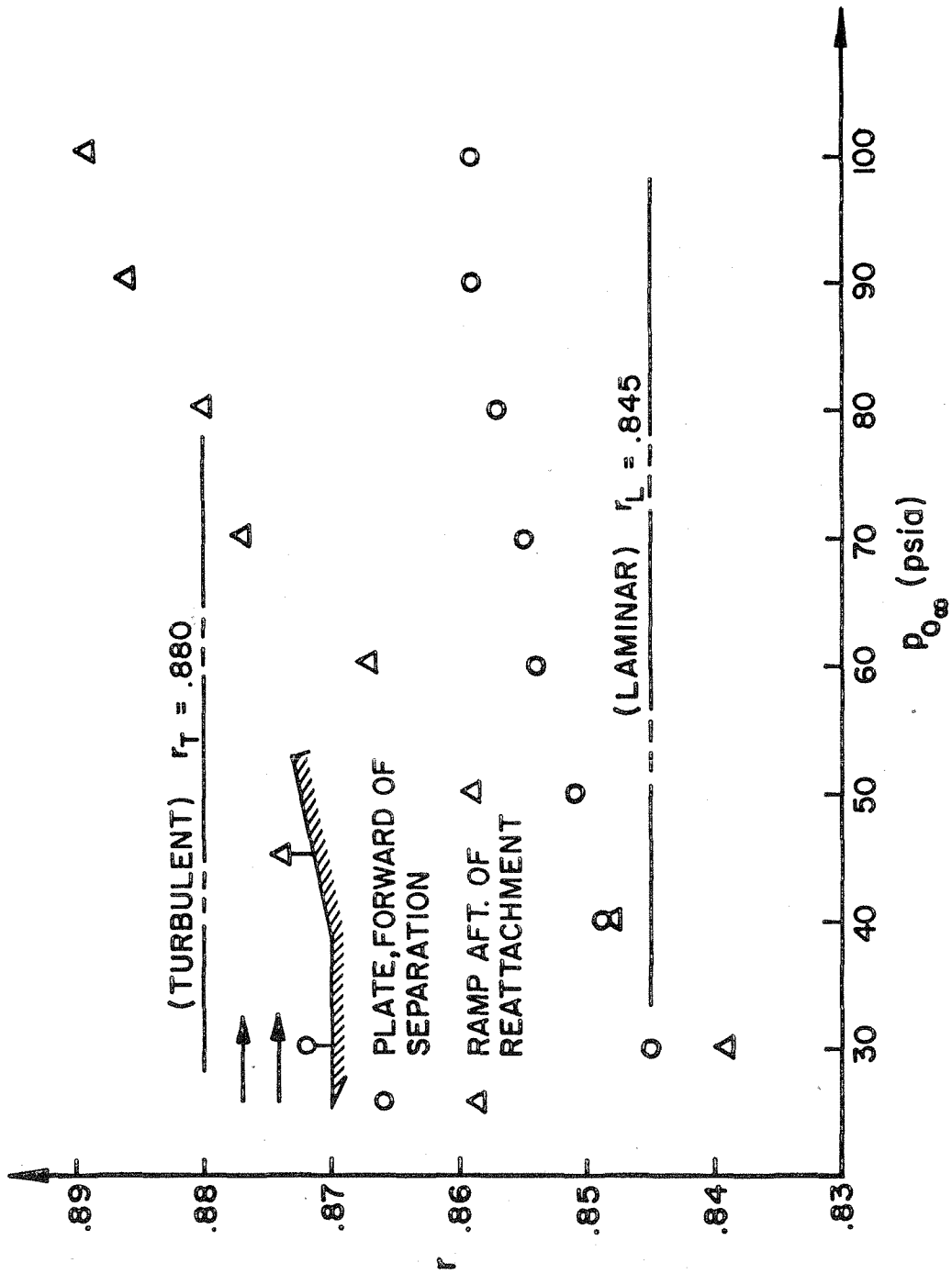


Figure 40. Recovery Factor, Model C-1

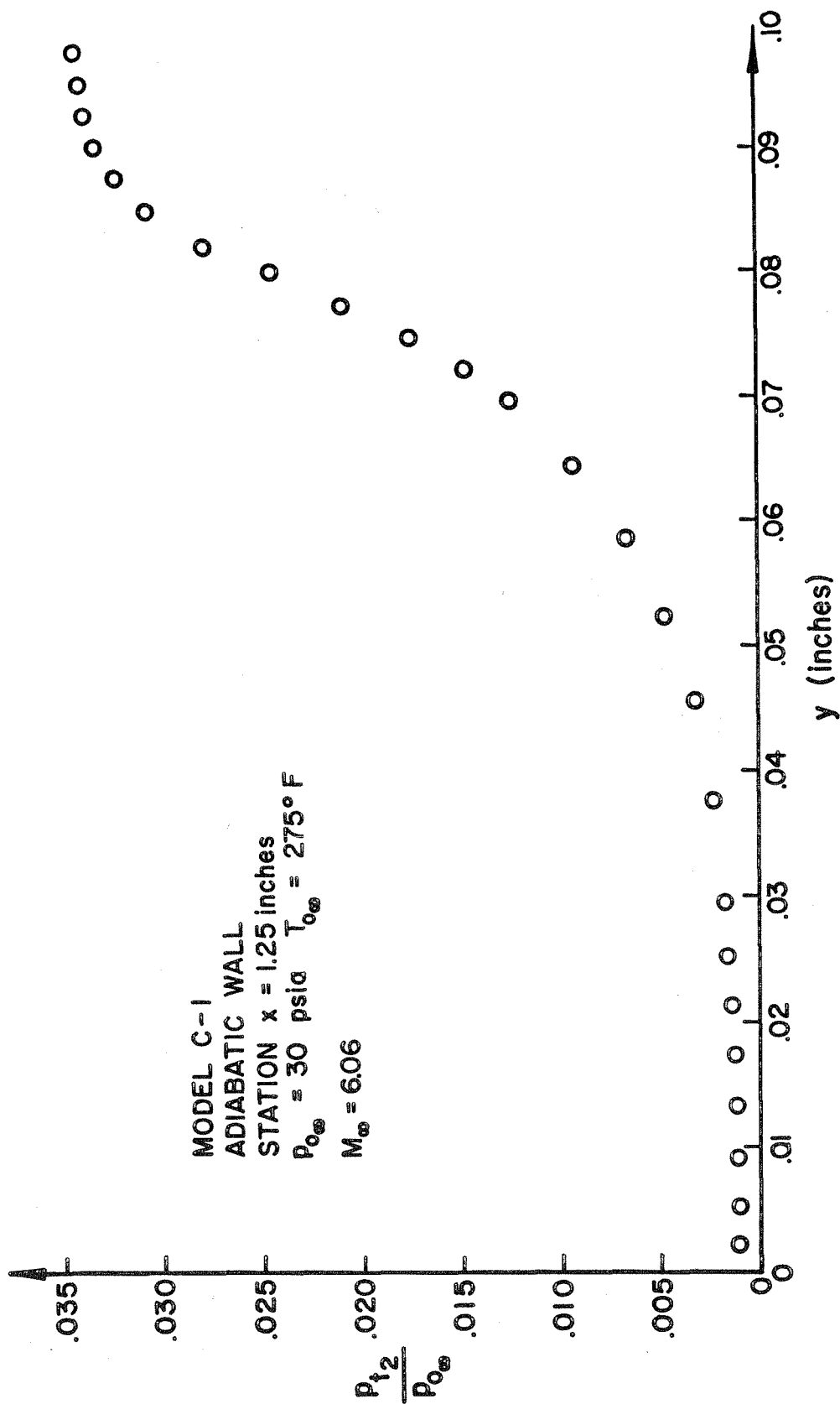


Figure 41. Pre-separation Pitot Trace

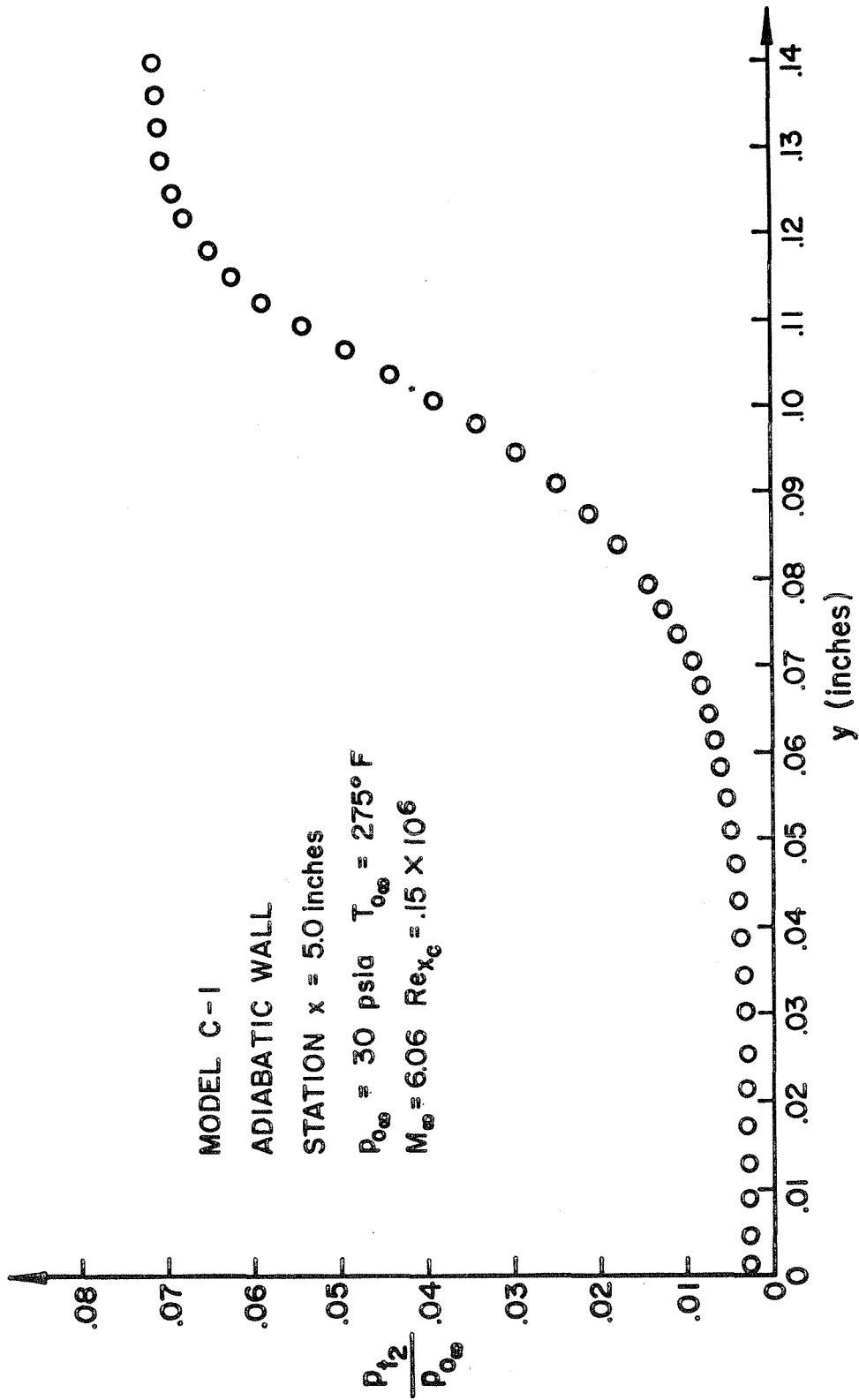


Figure 42. Post-reattachment Pitot Trace

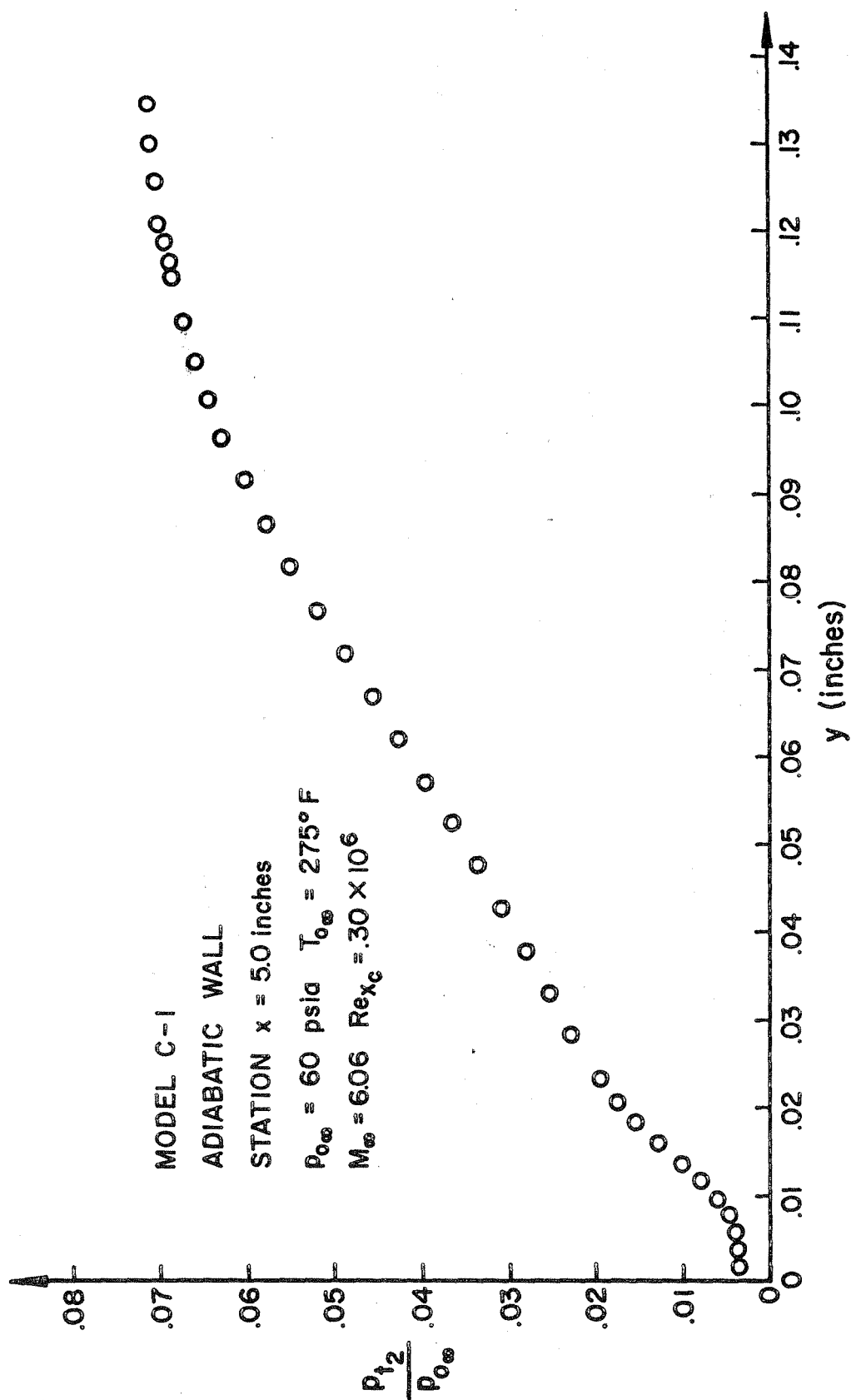


Figure 43. Post-reattachment Pitot Trace



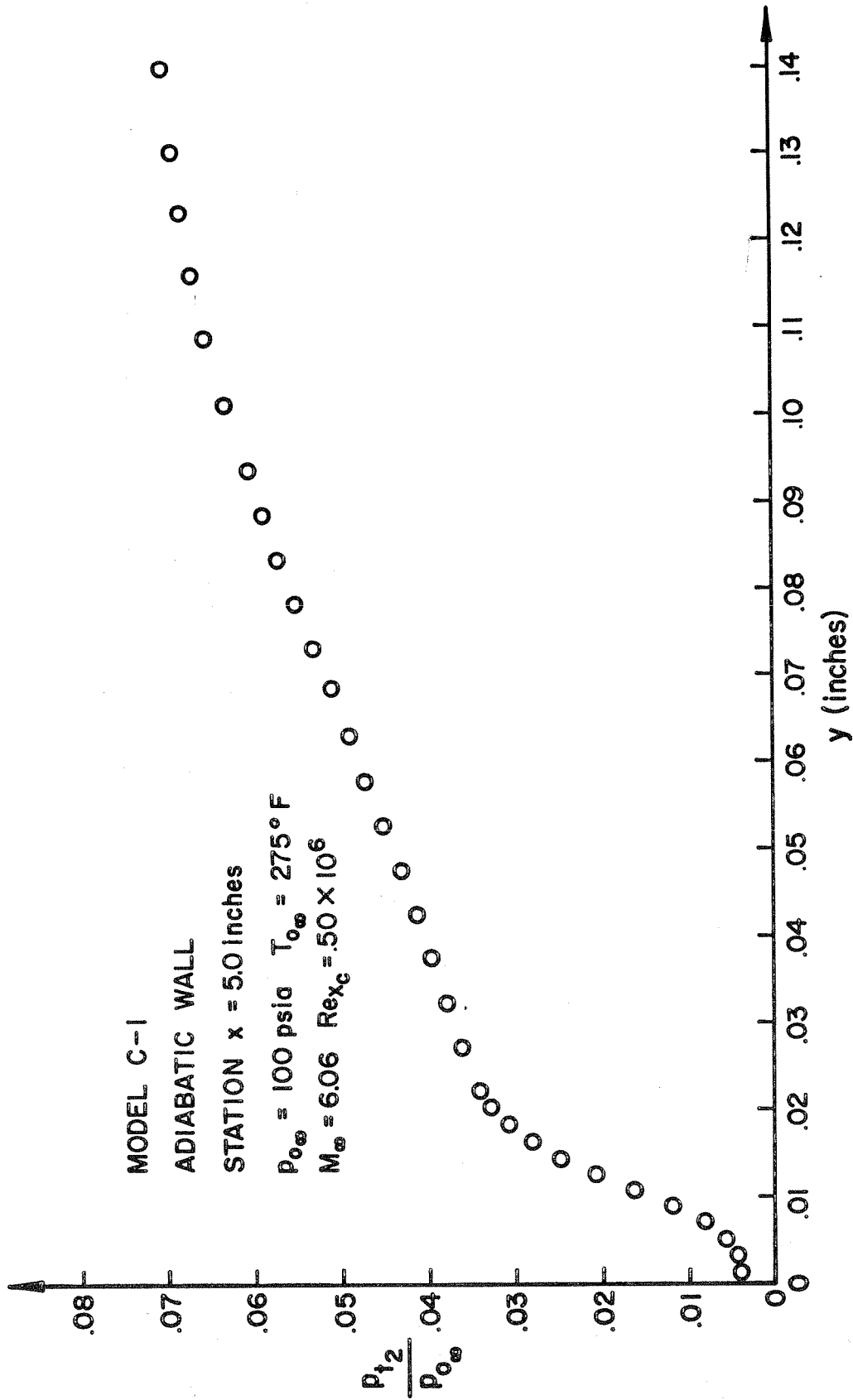


Figure 44. Post-reattachment Pitot Trace

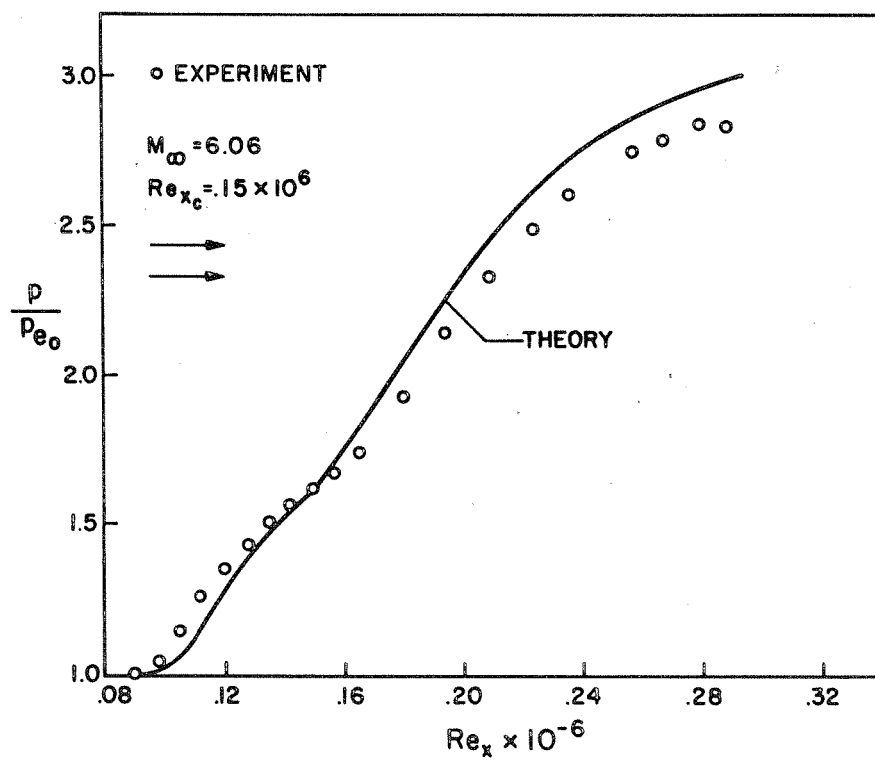
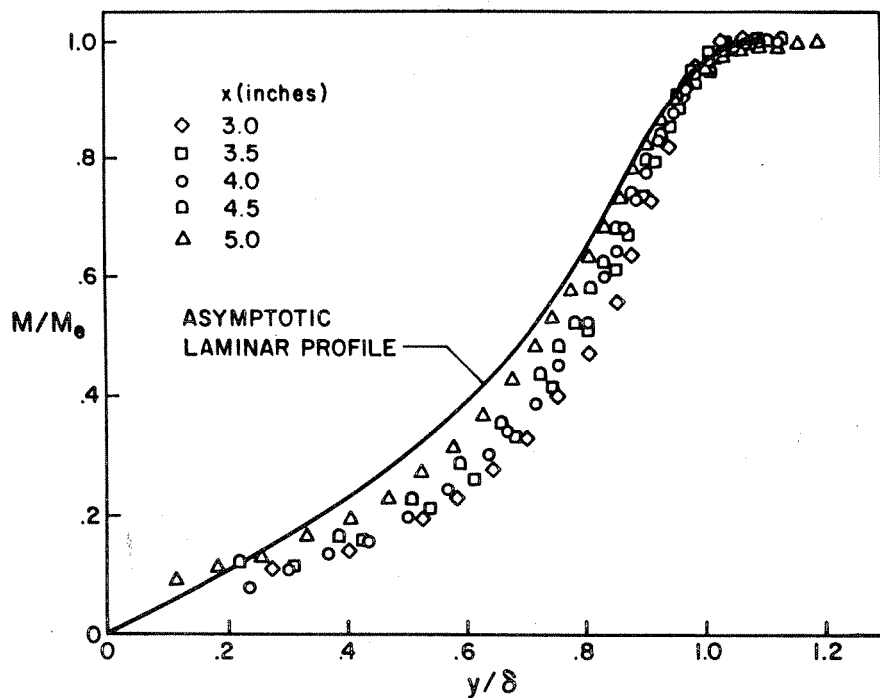


Figure 45. Comparison with Laminar Theory

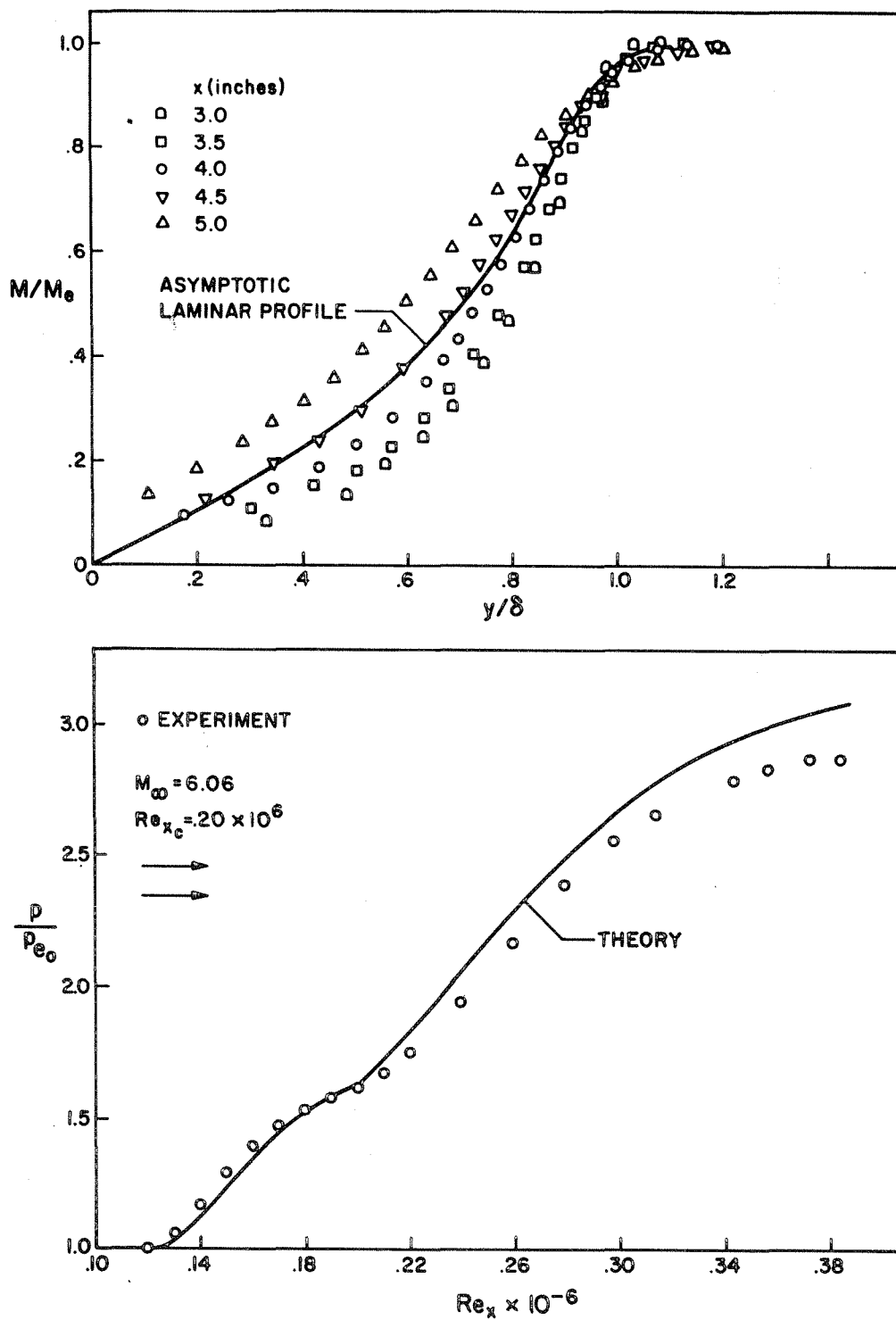


Figure 46. Comparison with Laminar Theory

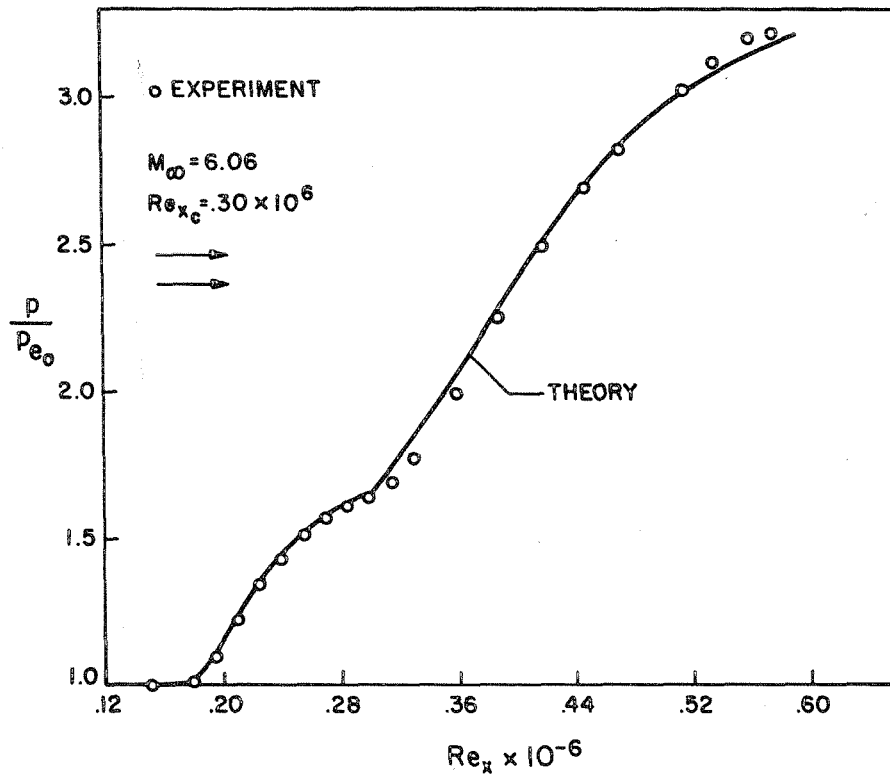
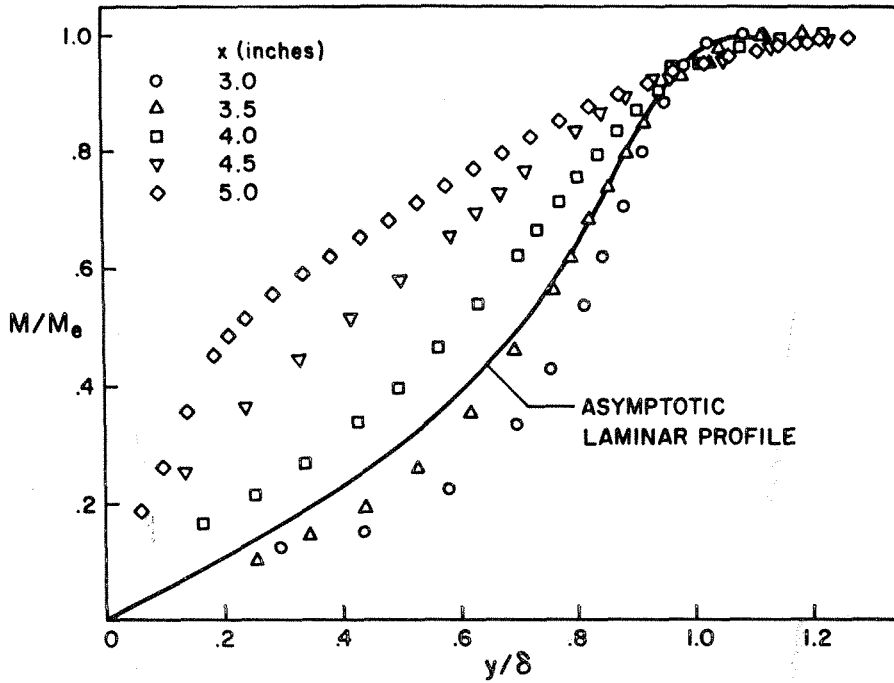


Figure 47. Comparison with Laminar Theory

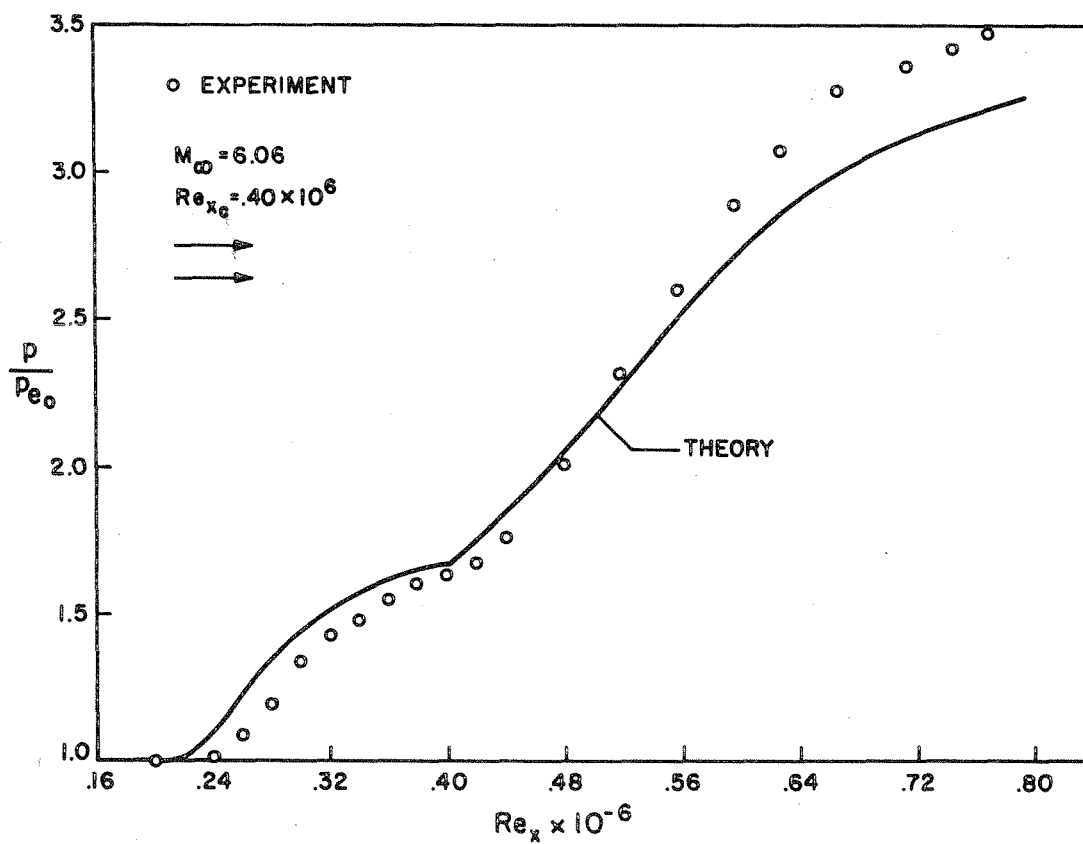
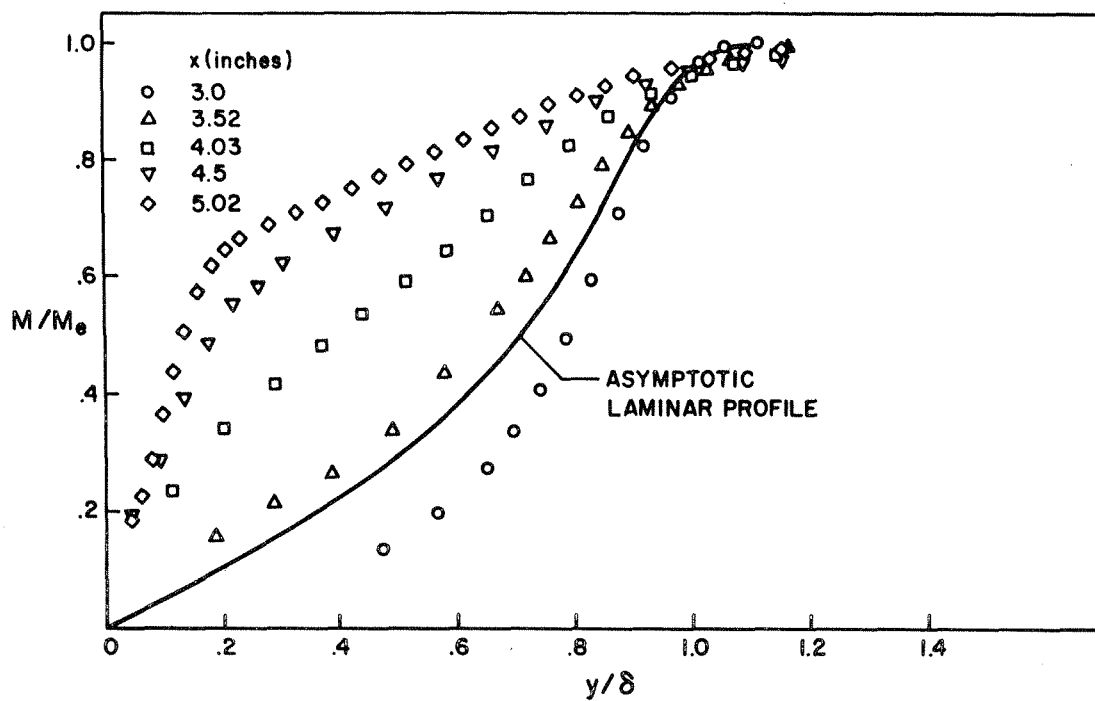


Figure 48. Comparison with Laminar Theory

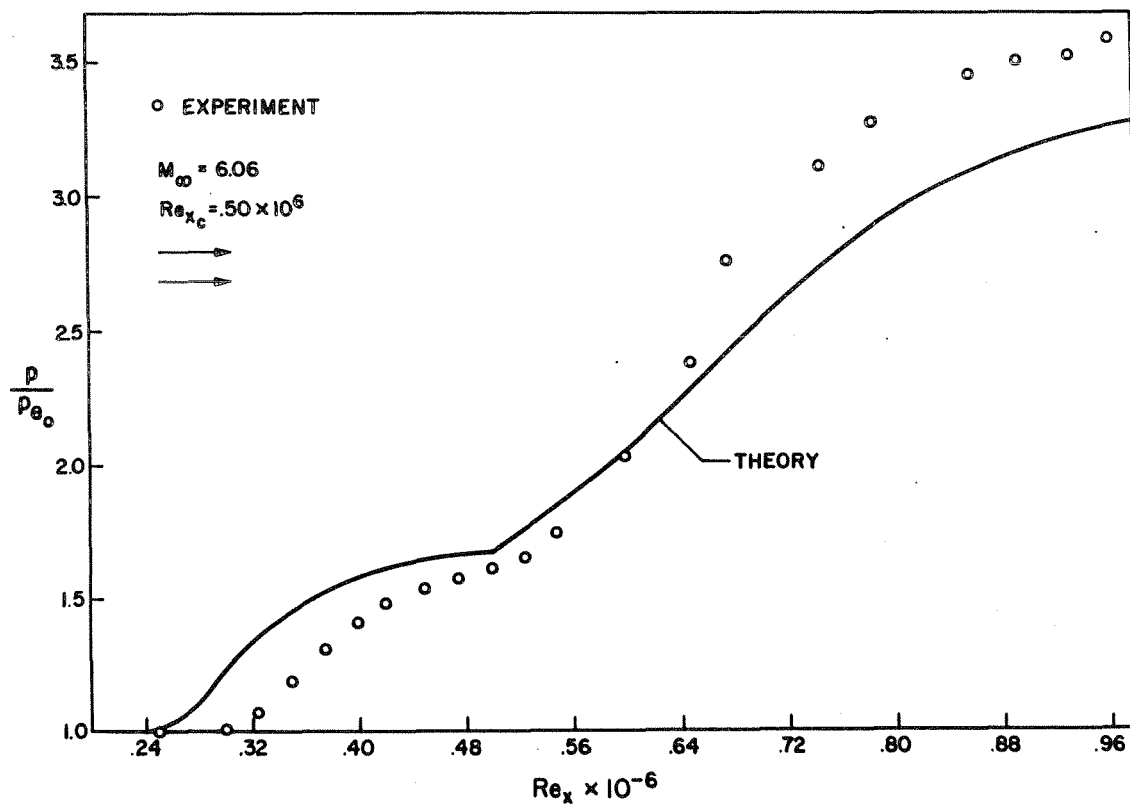
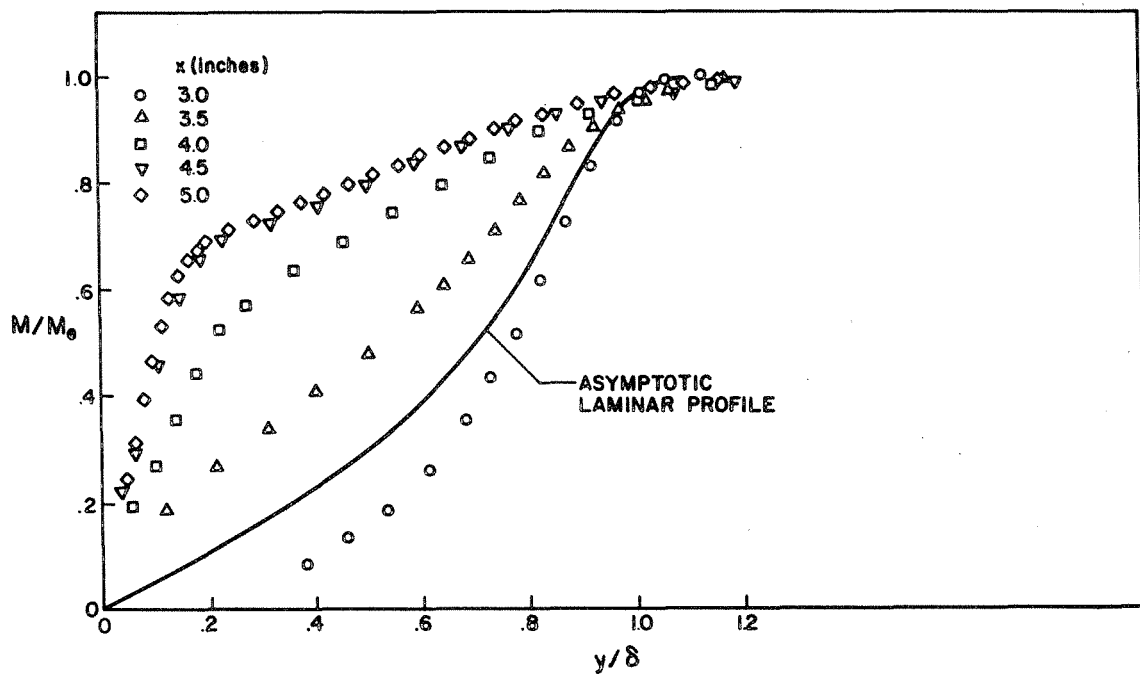


Figure 49. Comparison with Laminar Theory

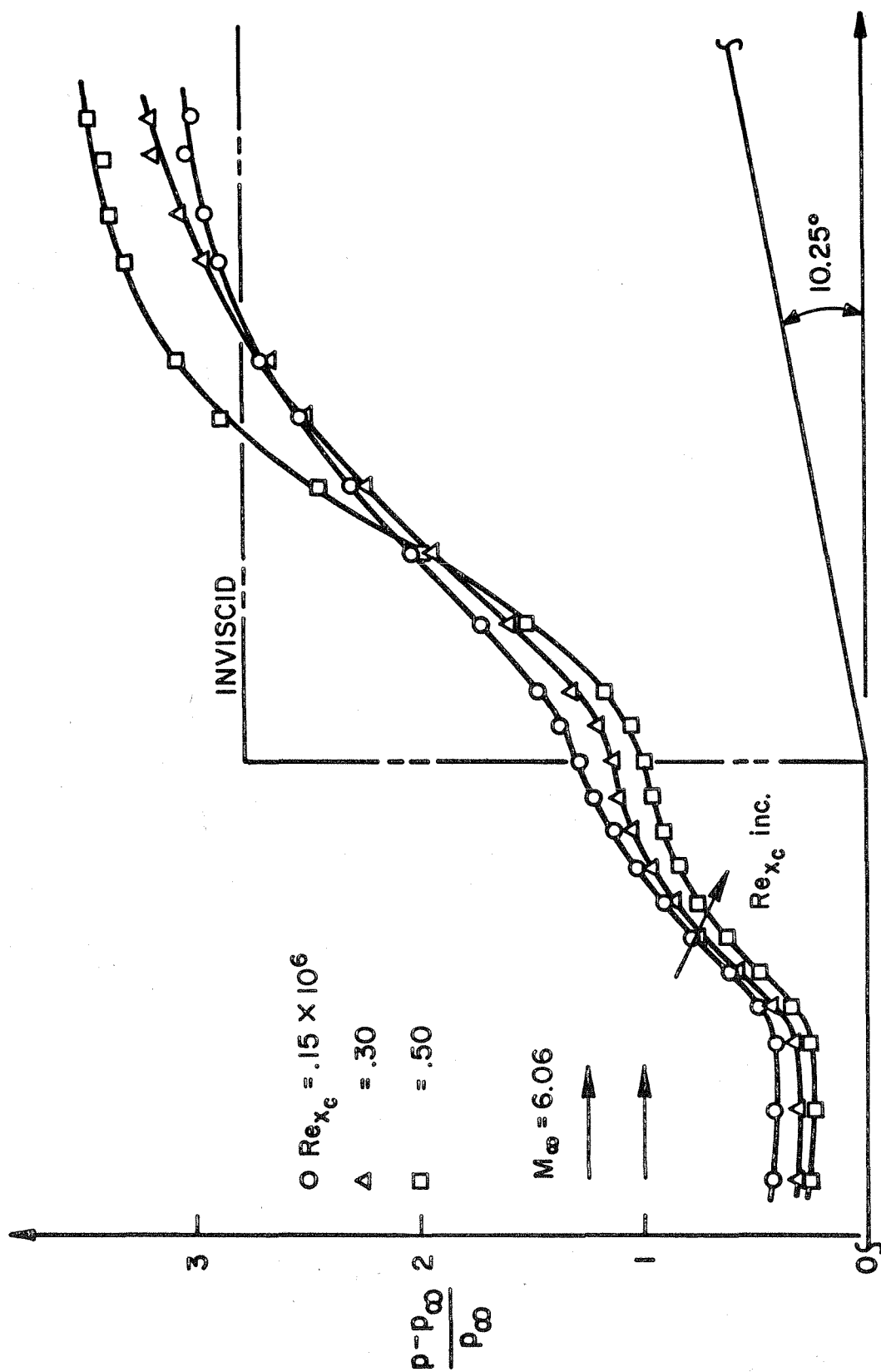


Figure 50. Reynolds Number Dependence of Transitional Interactions

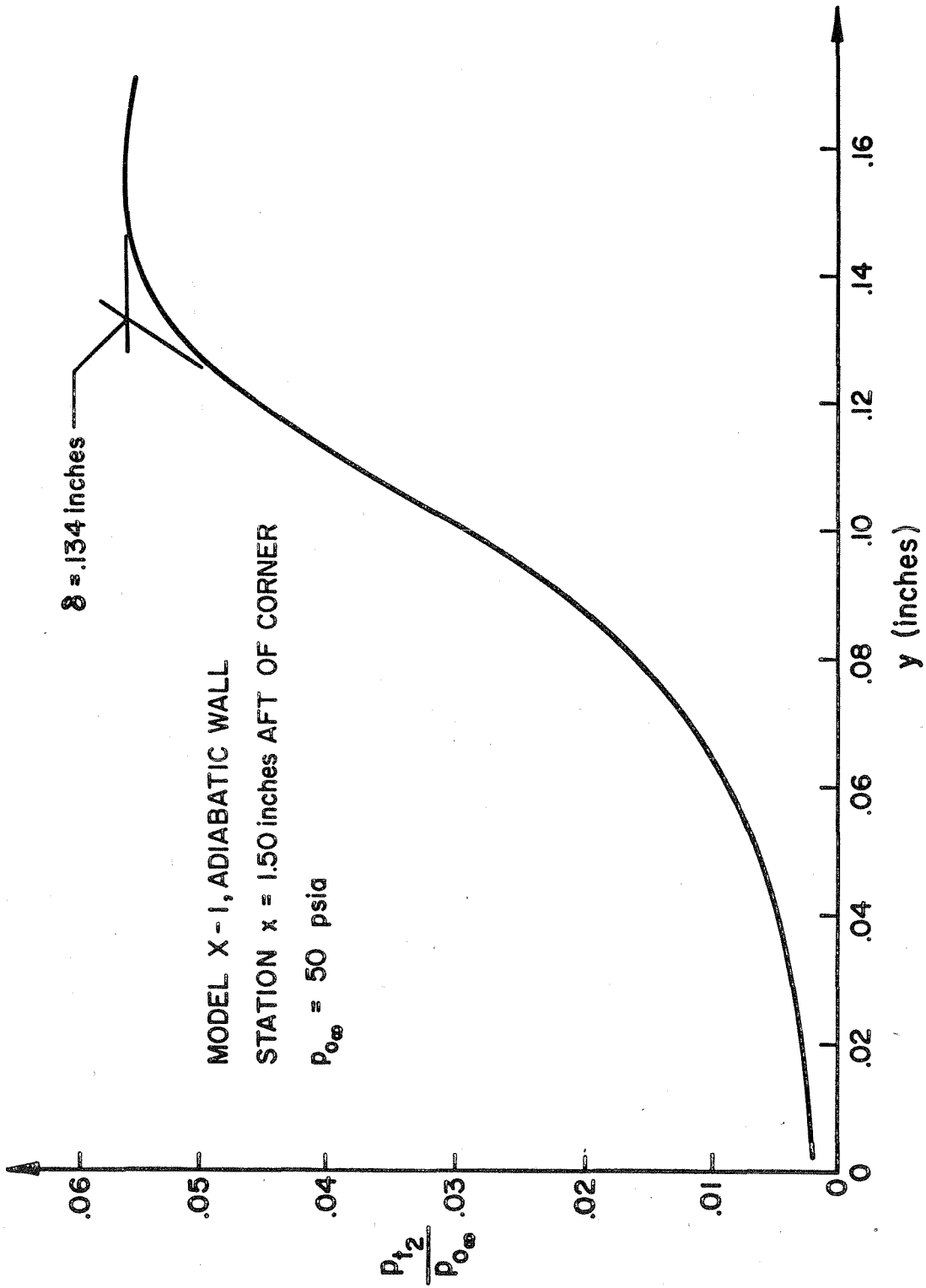


Figure 51. Boundary Layer Thickness Definition



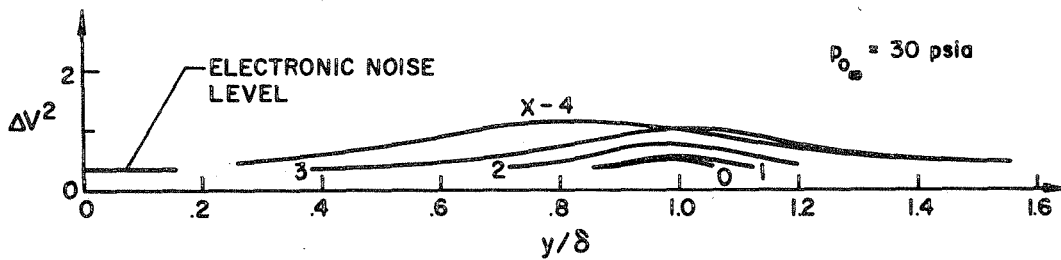
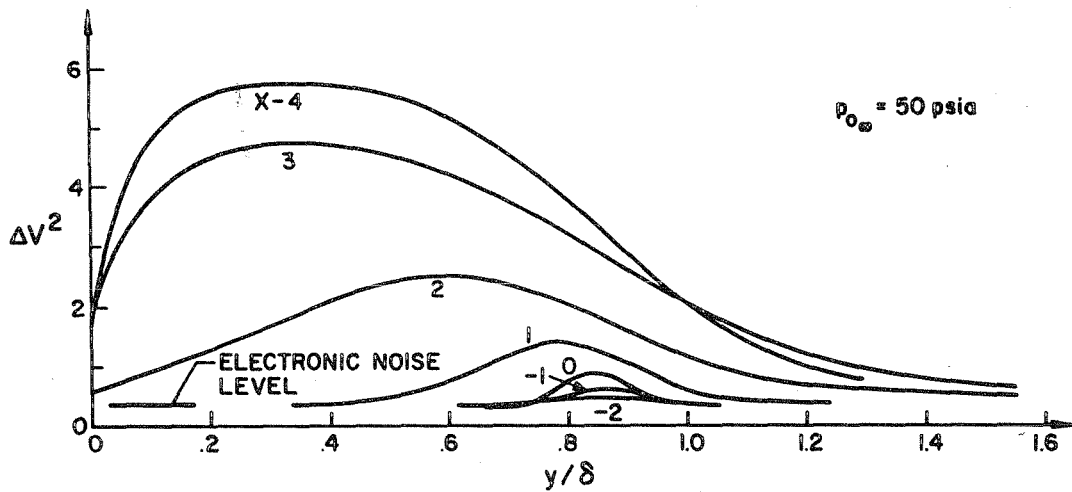
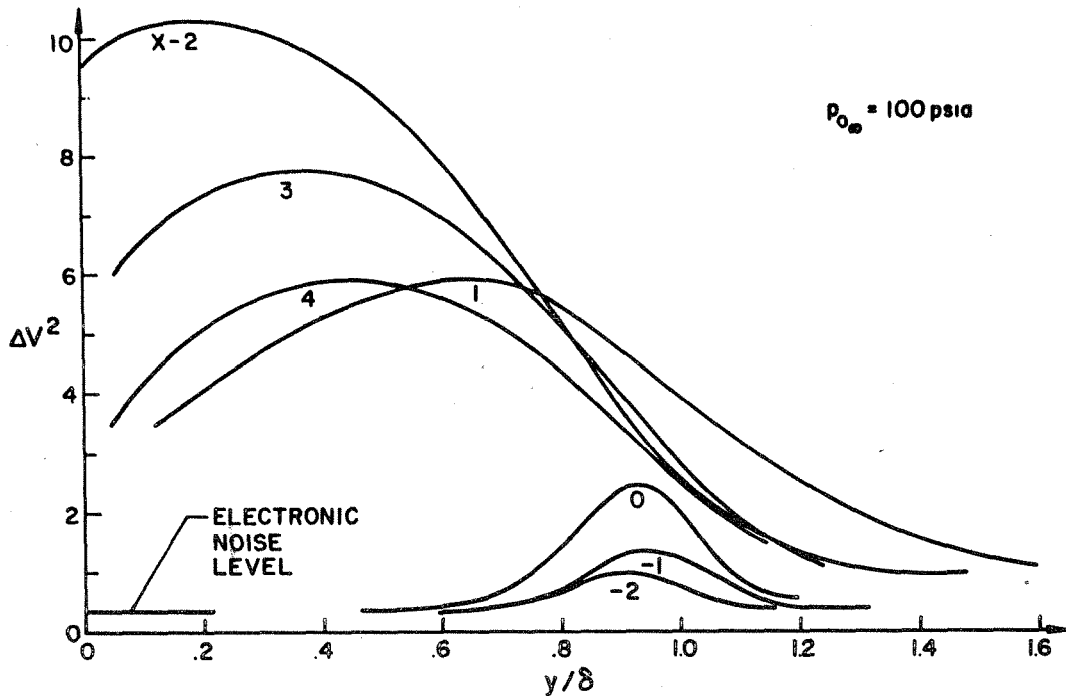
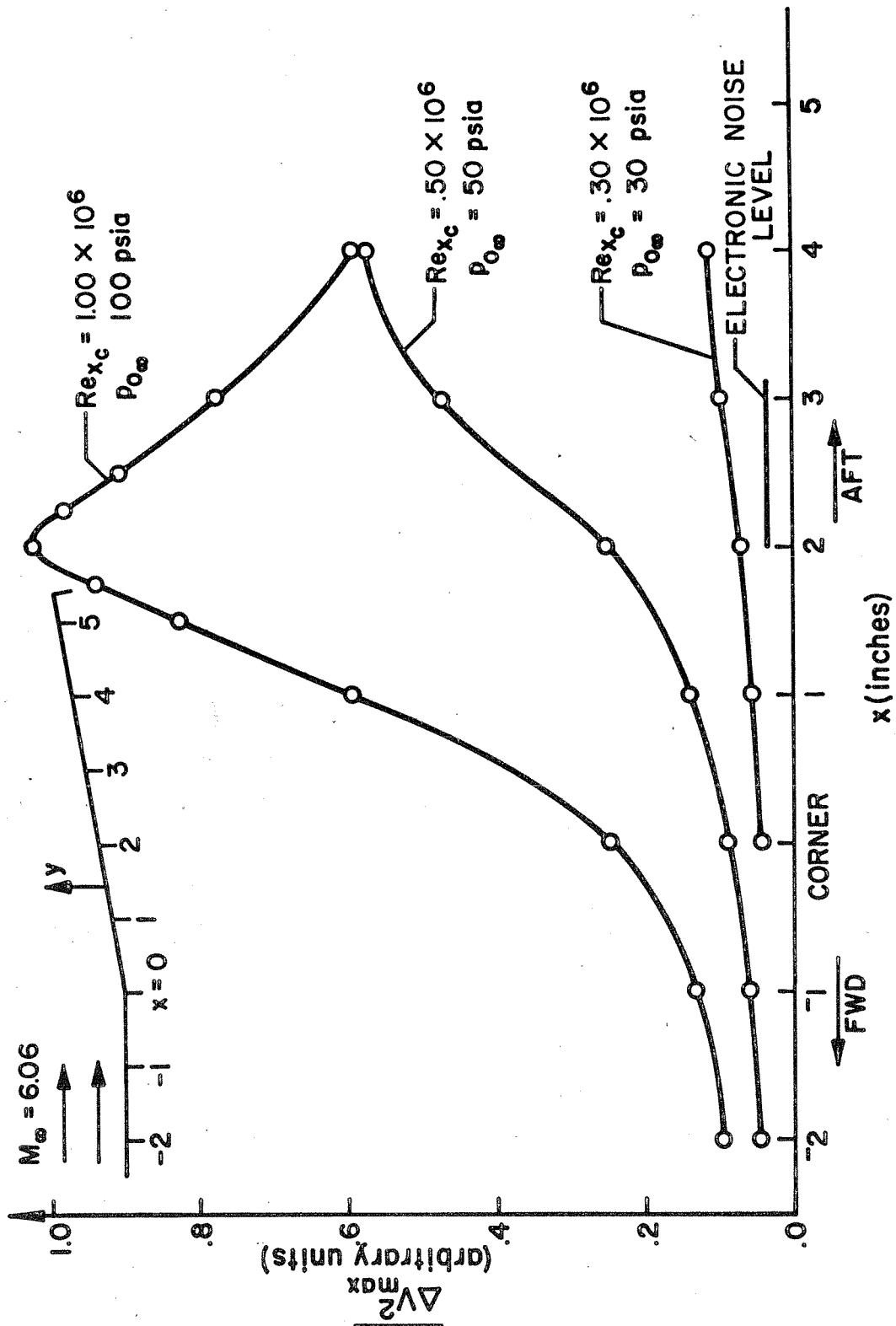


Figure 52. Fluctuation Measurements



**Figure 53. Maximum Fluctuation Signal**

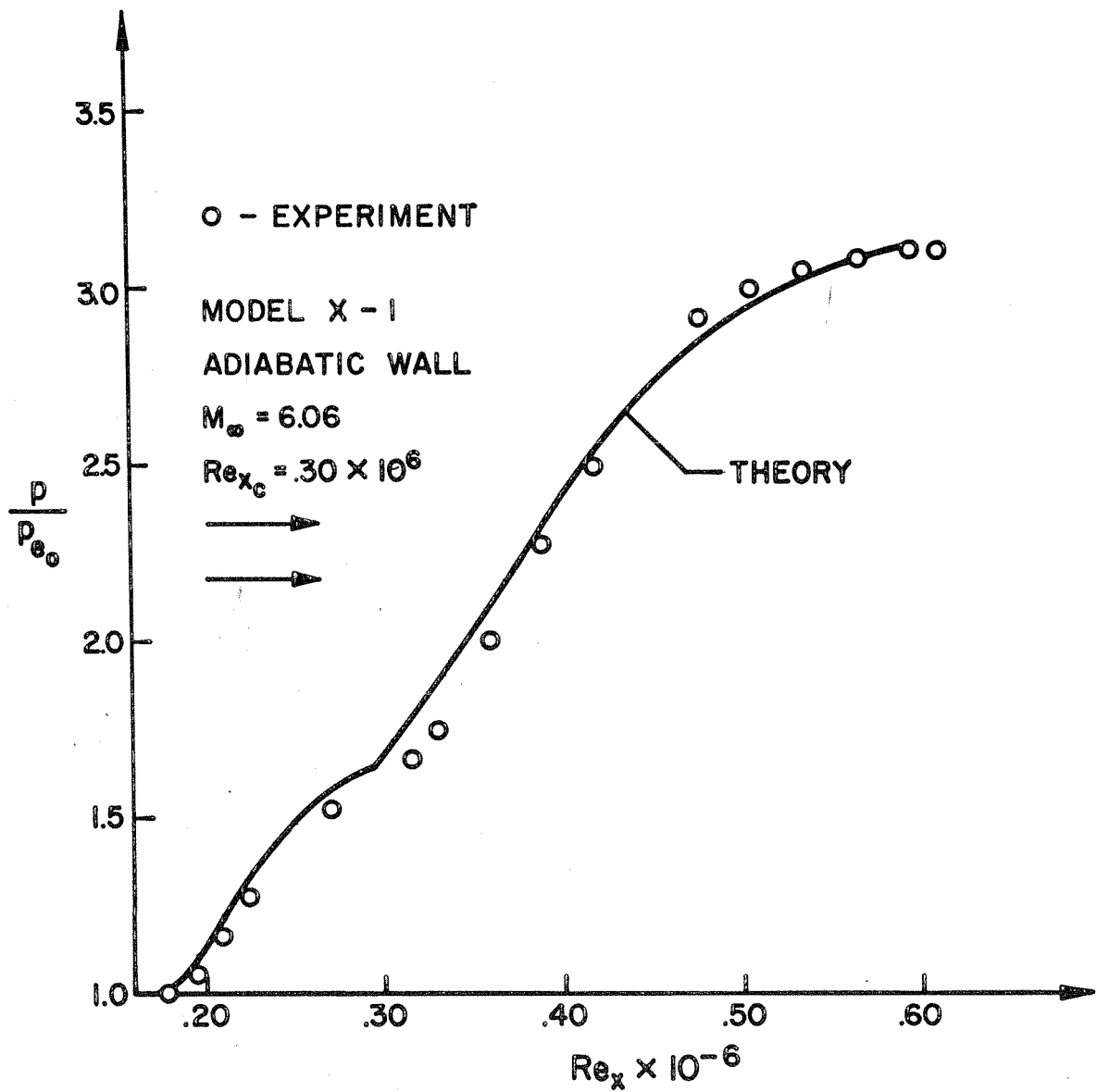


Figure 54. Comparison with Laminar Theory

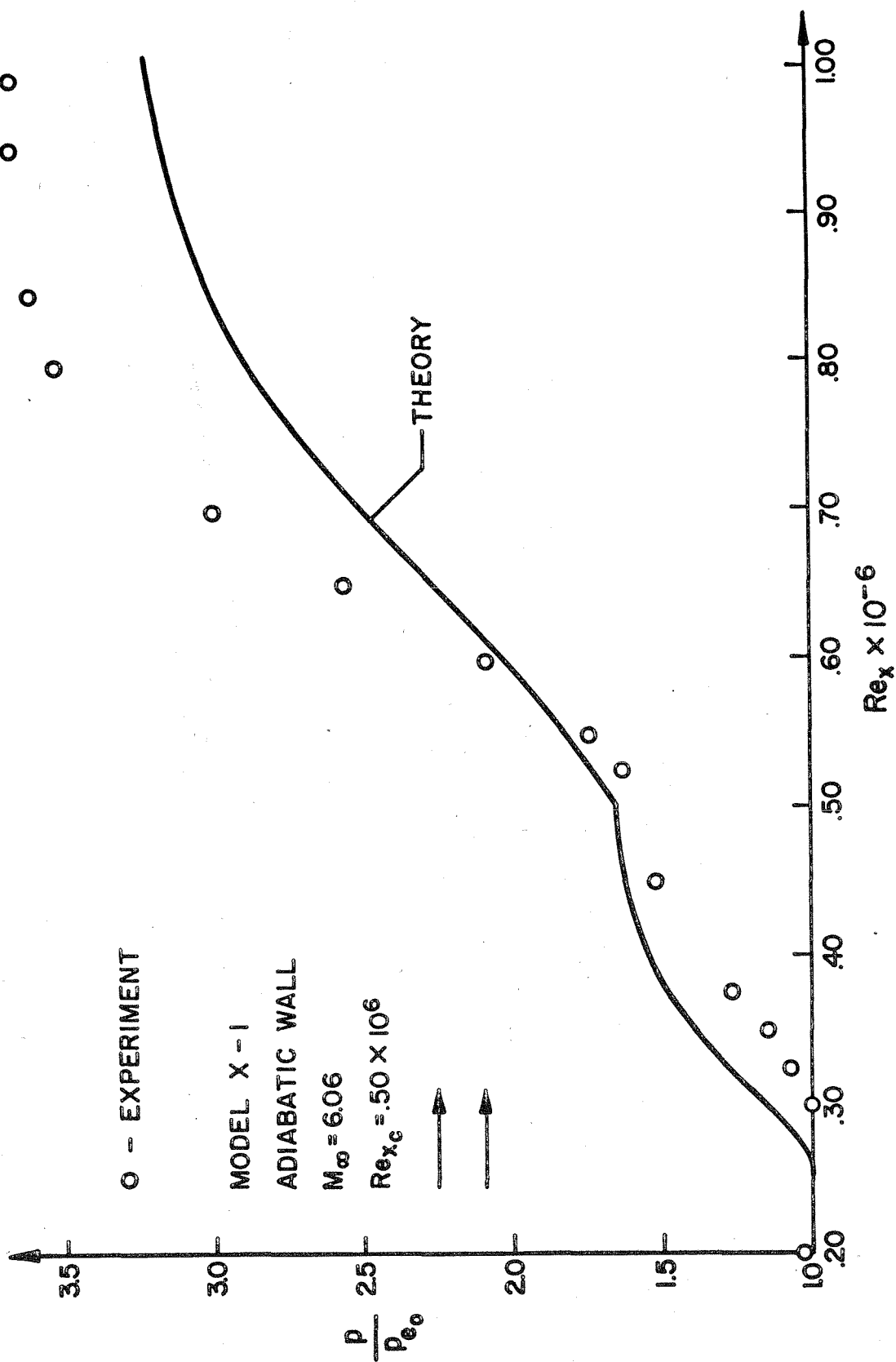


Figure 55. Comparison with Laminar Theory

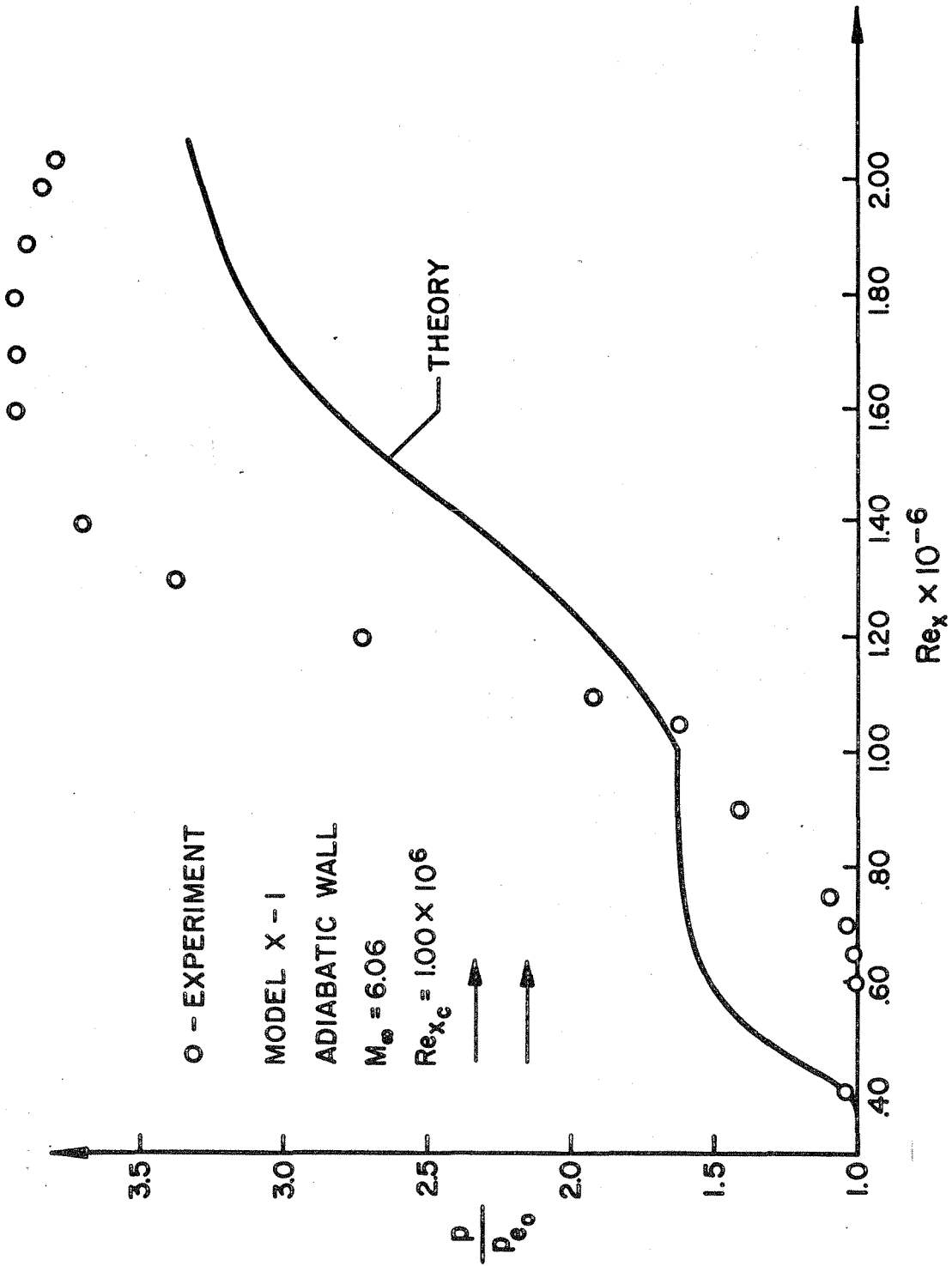


Figure 56. Comparison with Laminar Theory

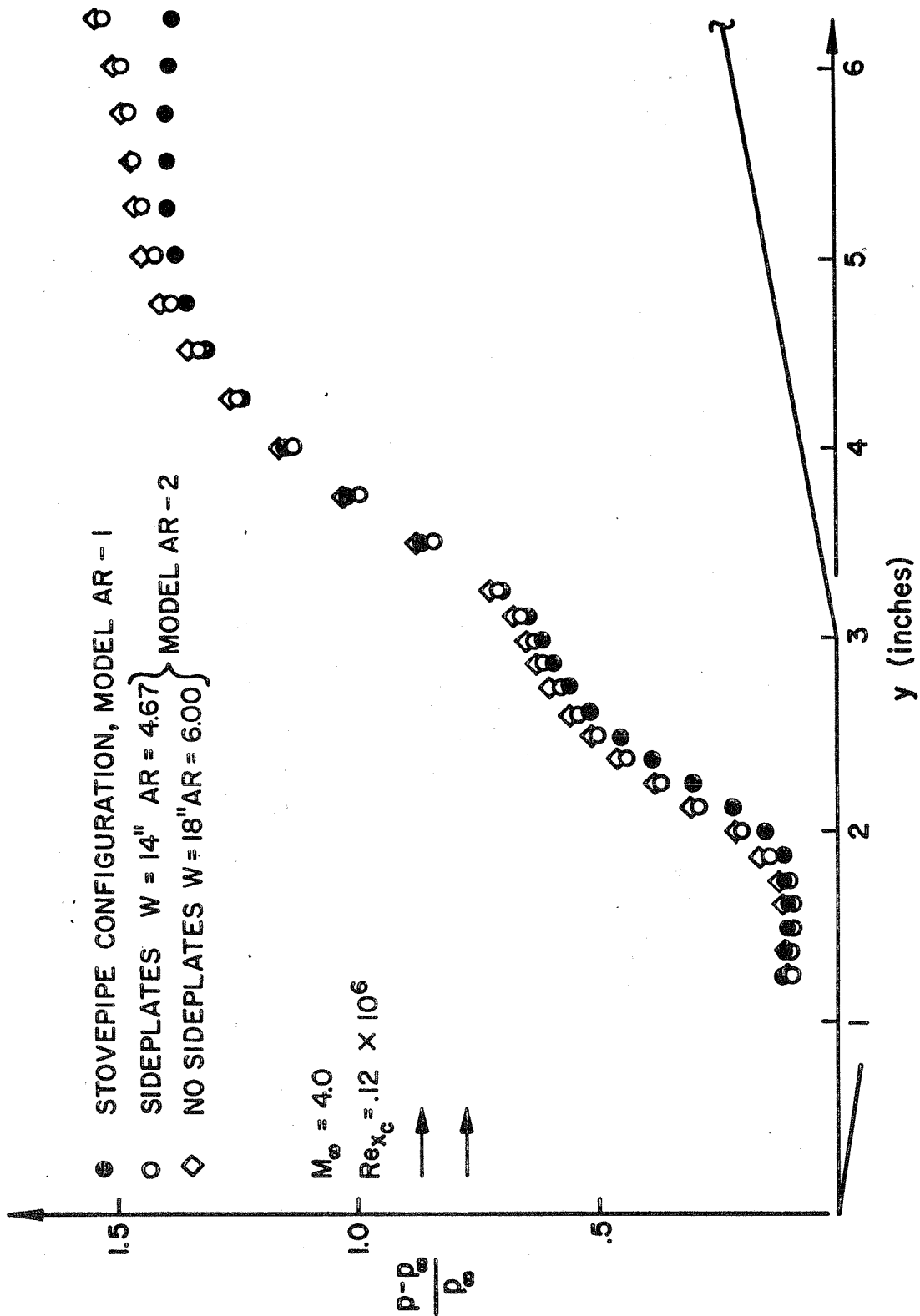


Figure 57. Model Correlation

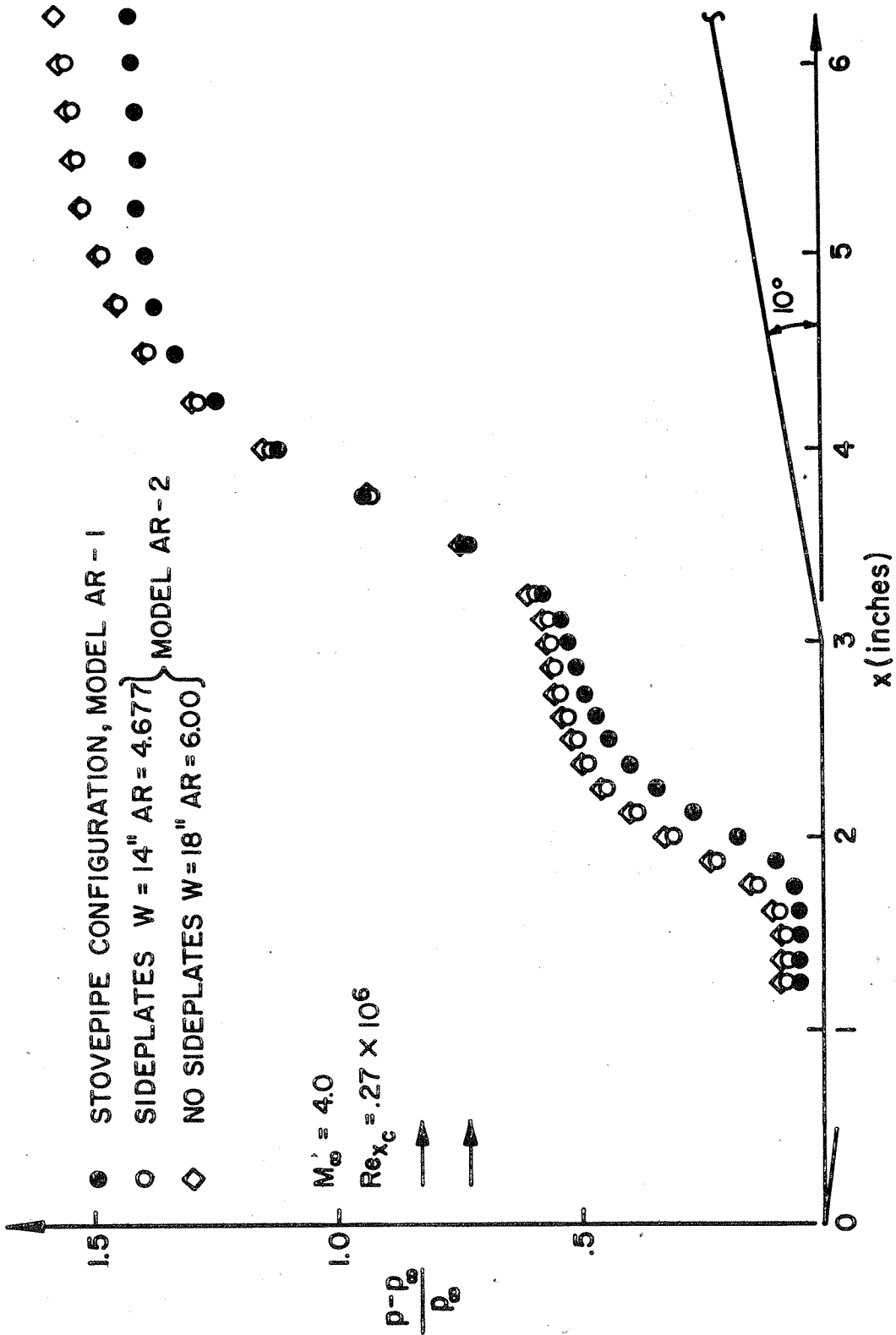


Figure 58. Model Correlation

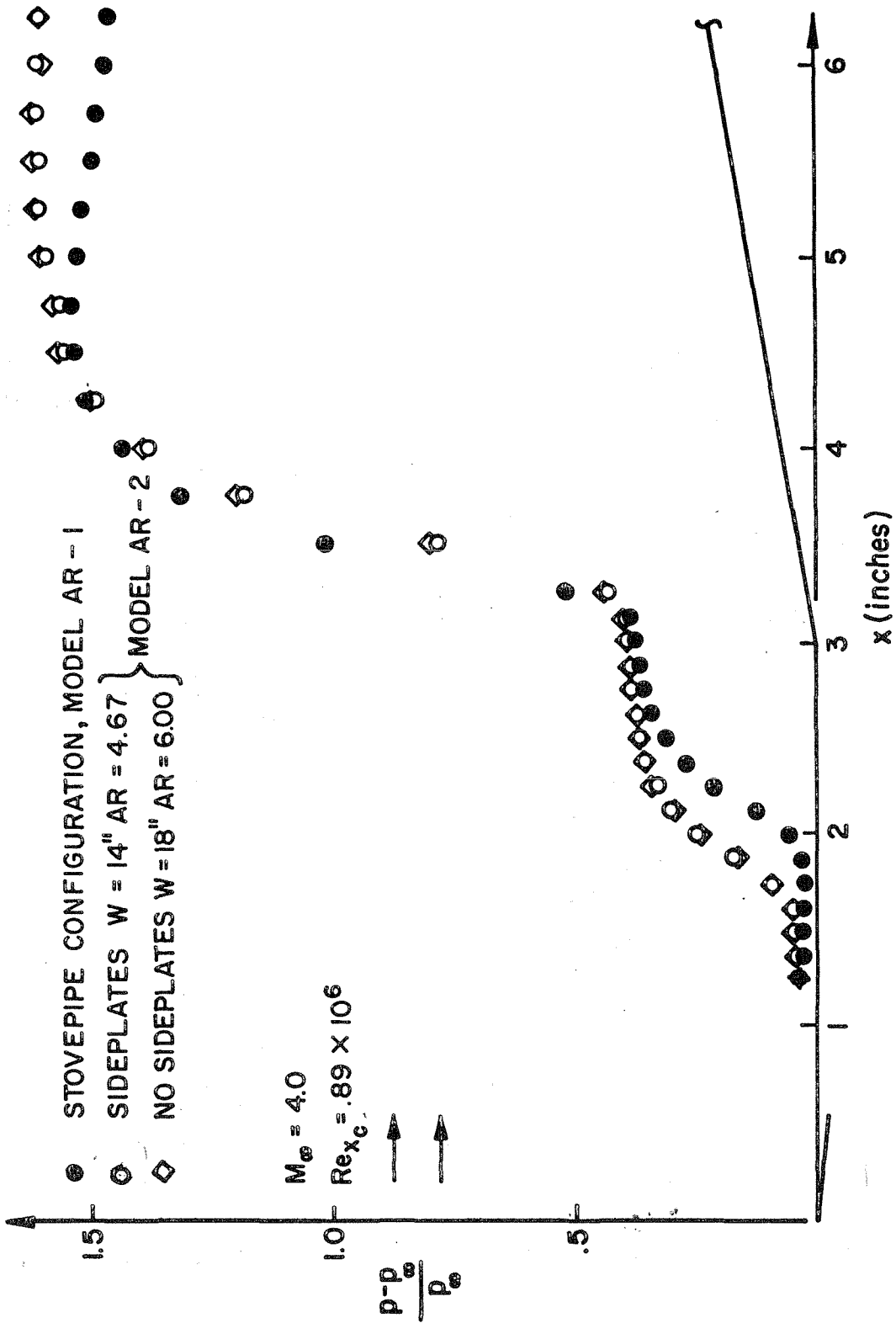


Figure 59. Model Correlation



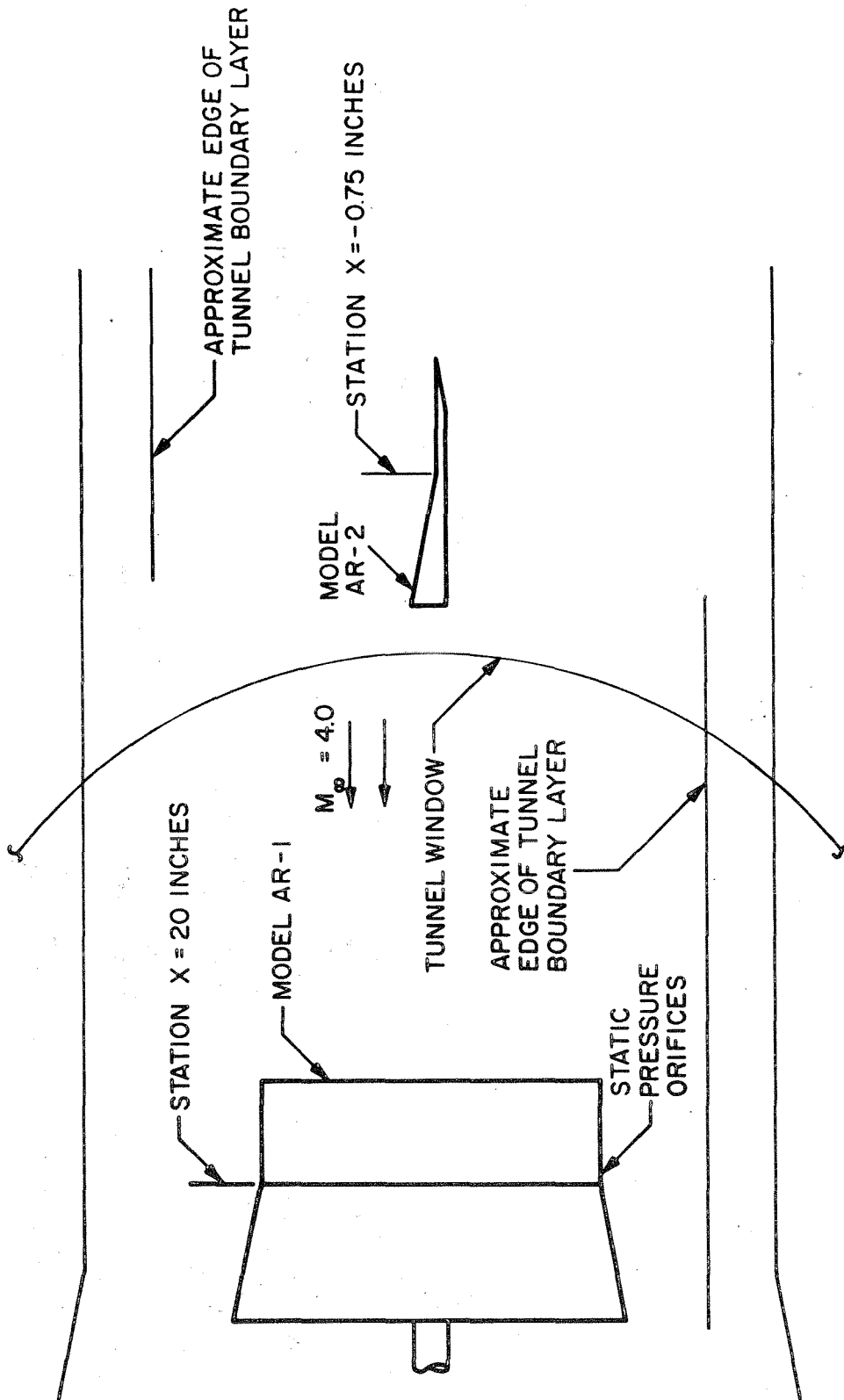


Figure 60. Schematic of Model AR-1, -2 Locations in JPL SWT

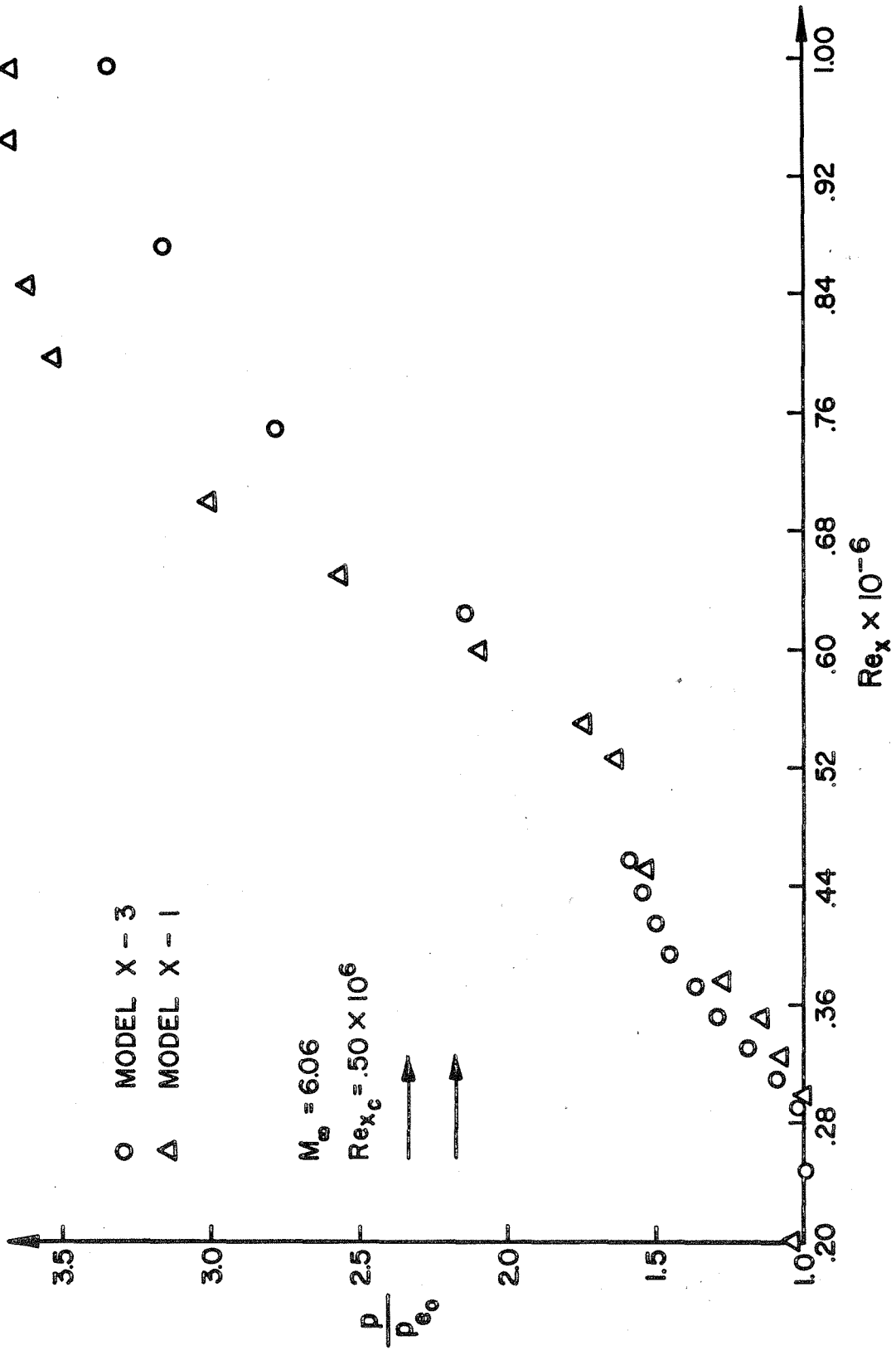


Figure 61. Reynolds Number Correlation

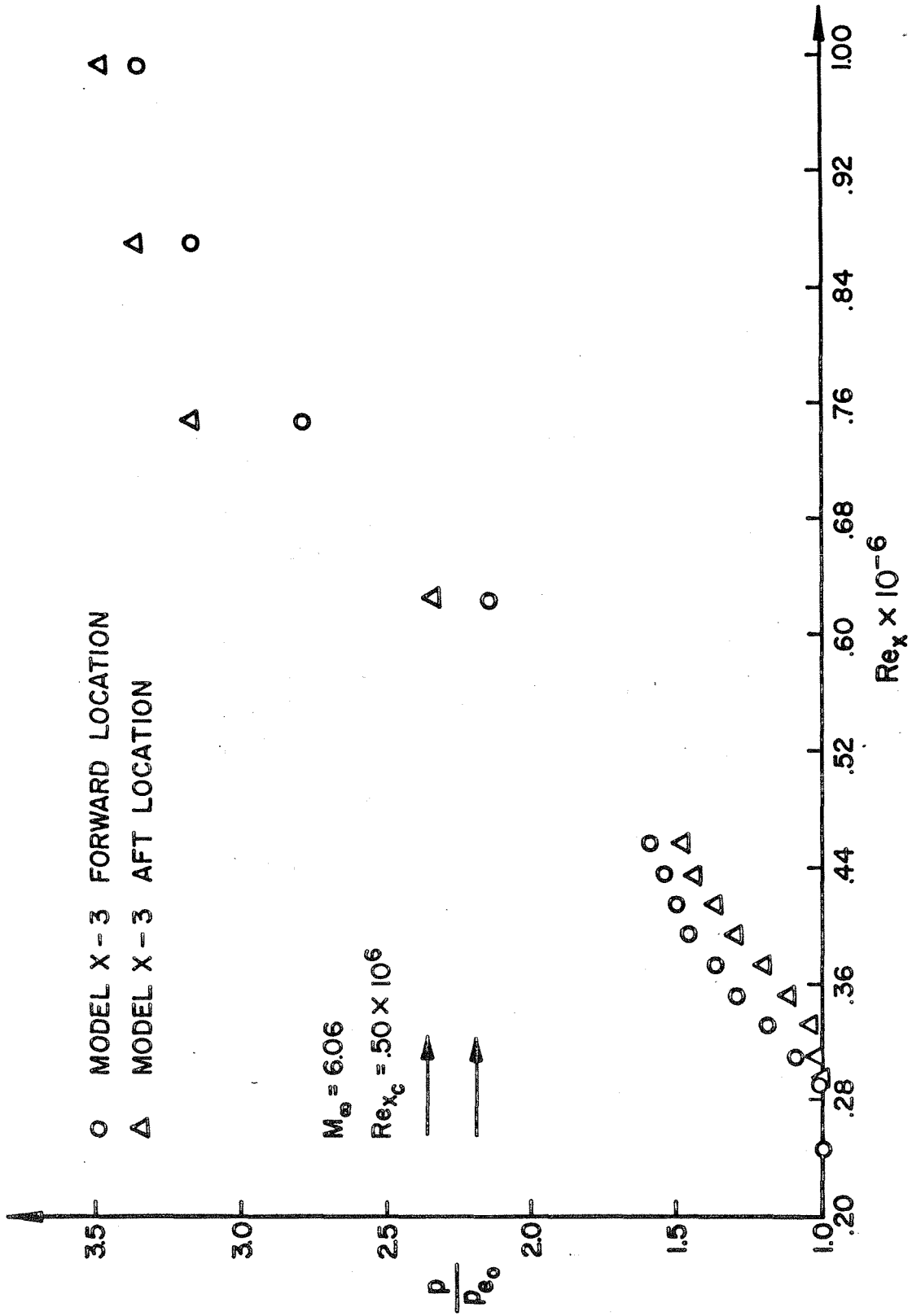


Figure 62. Sensitivity of Model Location

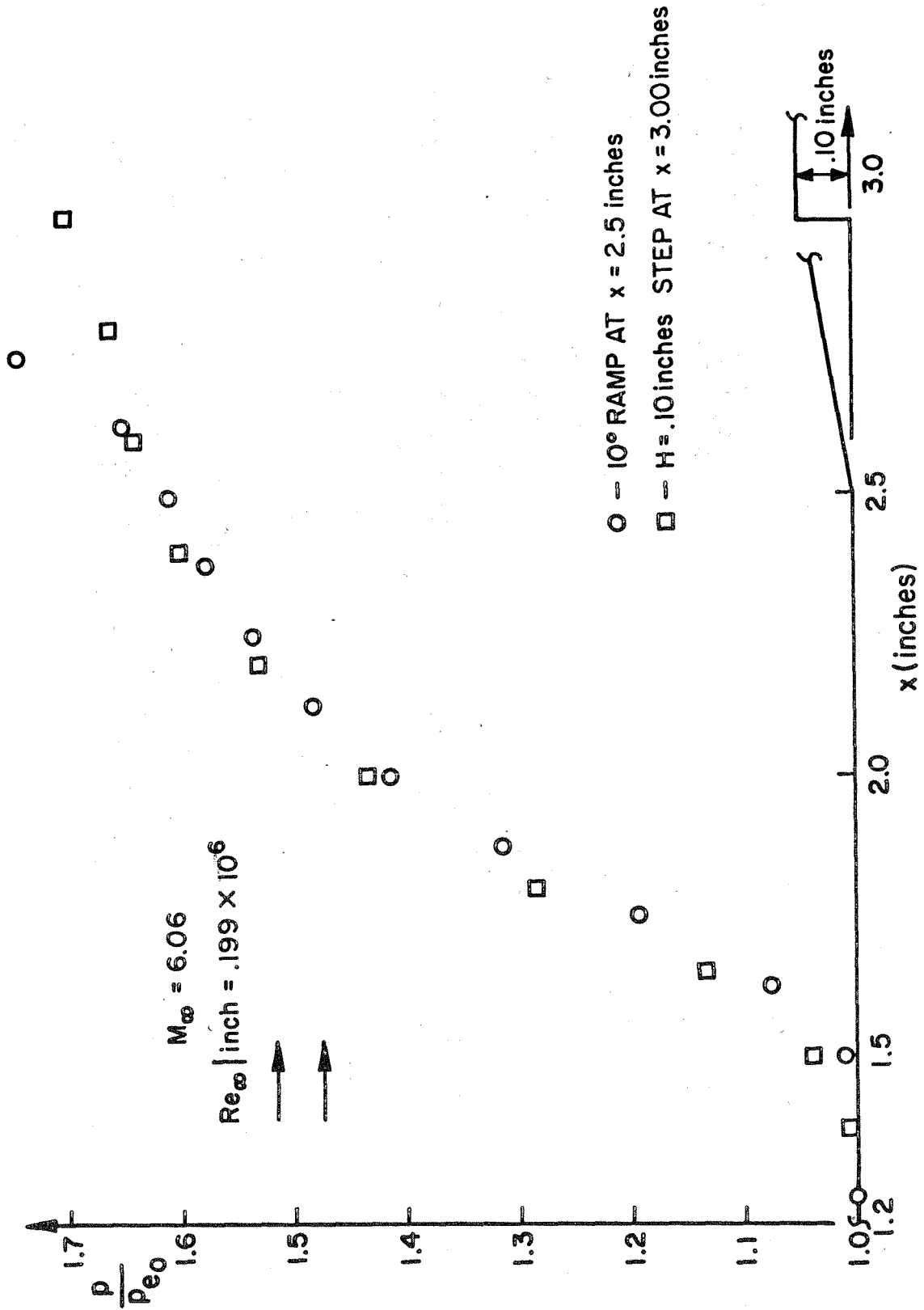


Figure 63. Free Interaction Step-ramp Comparison

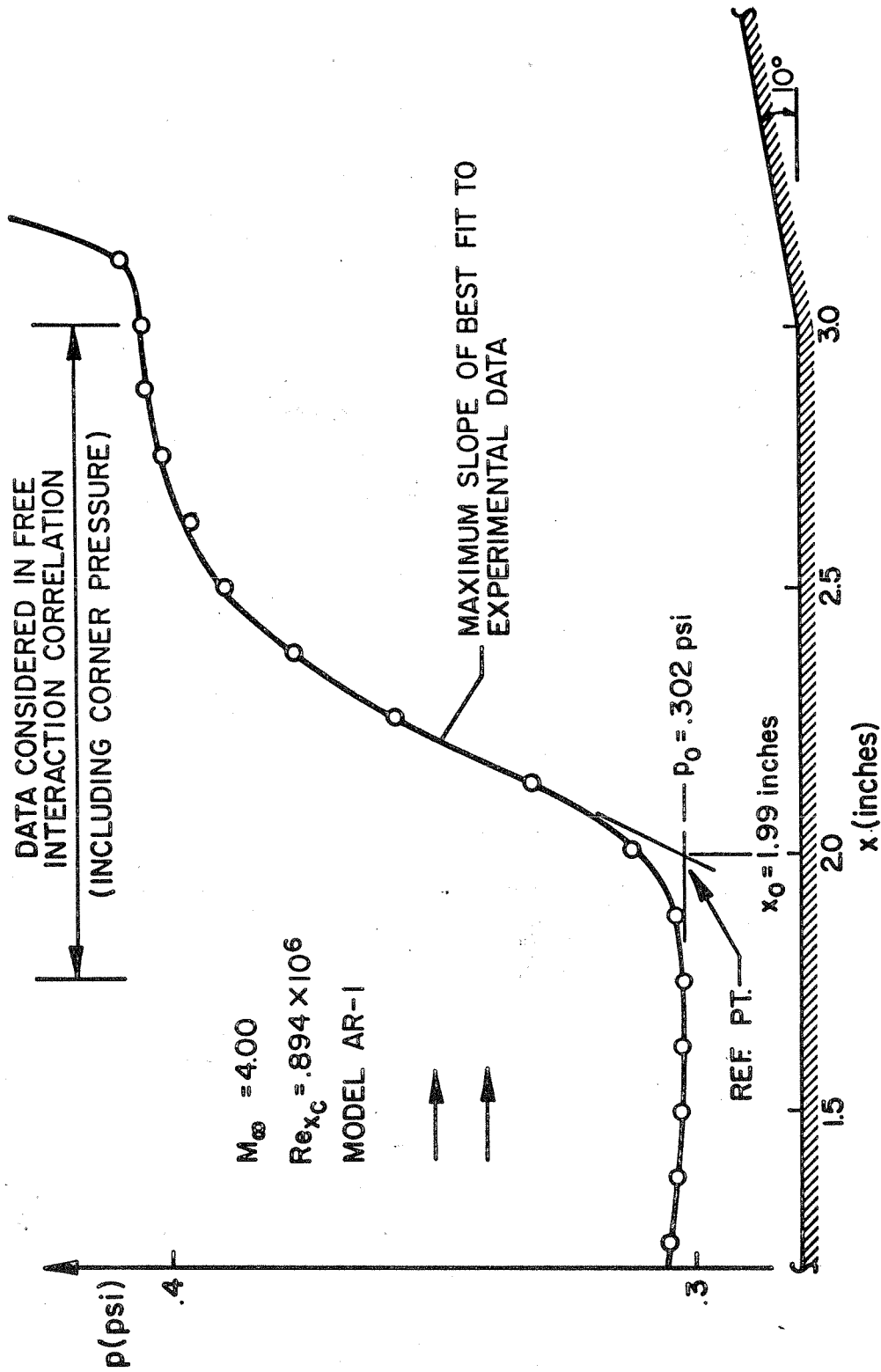


Figure 64. Typical Ramp Configuration Pressure Distribution (Adiabatic Wall)

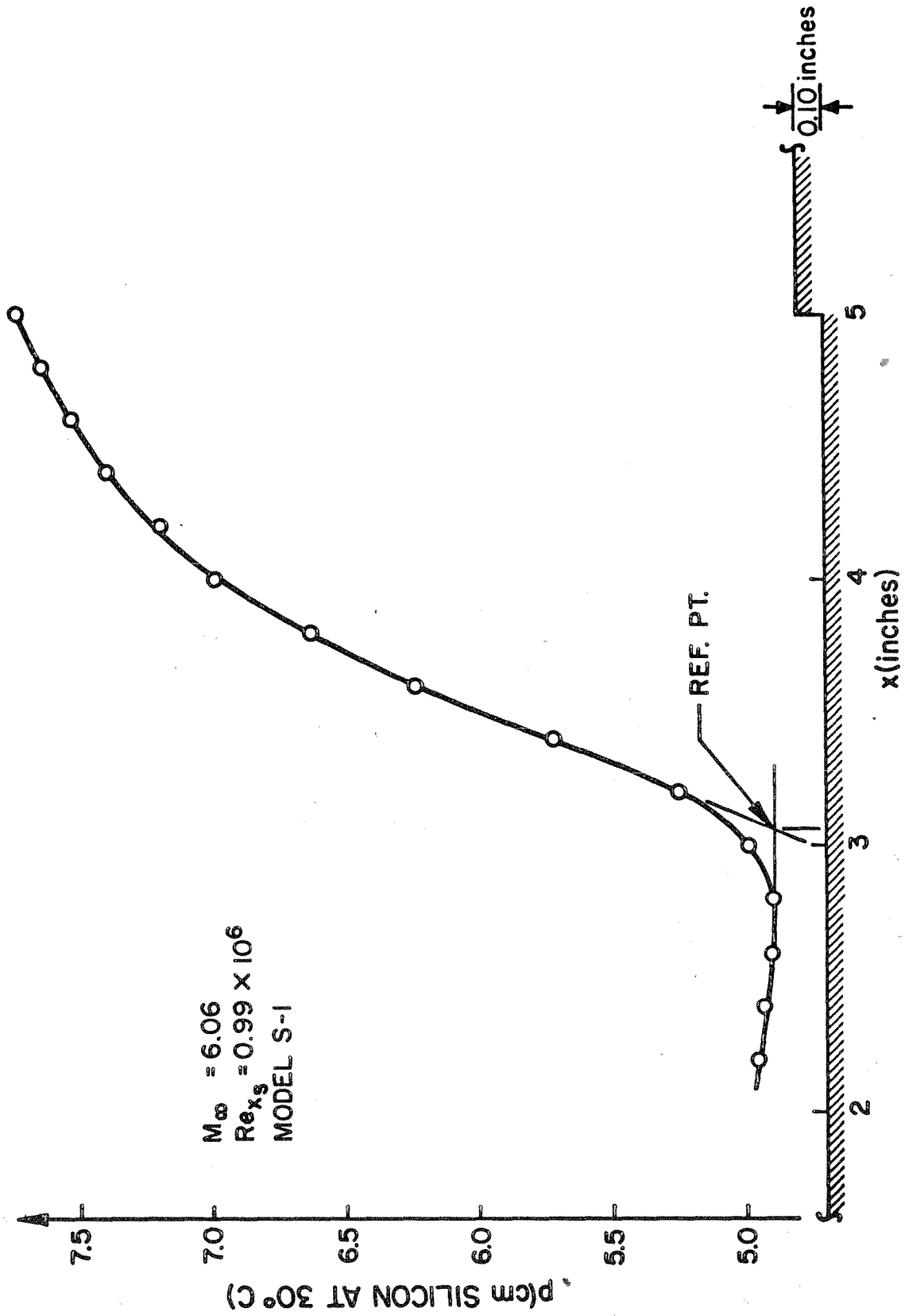


Figure 65. Typical Step Configuration Pressure Distribution (Adiabatic Wall)

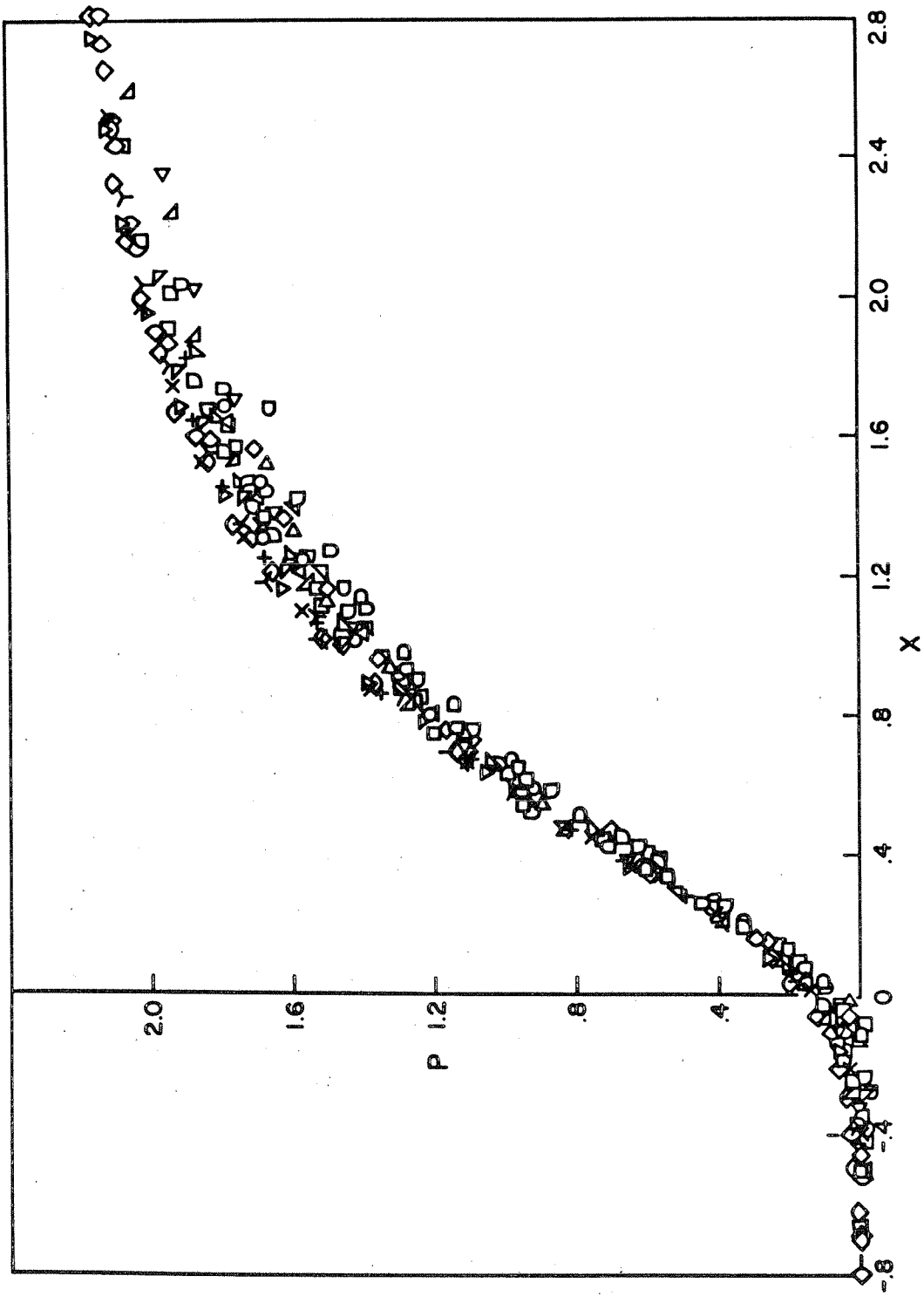


Figure 66. Chapman Correlation (Adiabatic Wall)

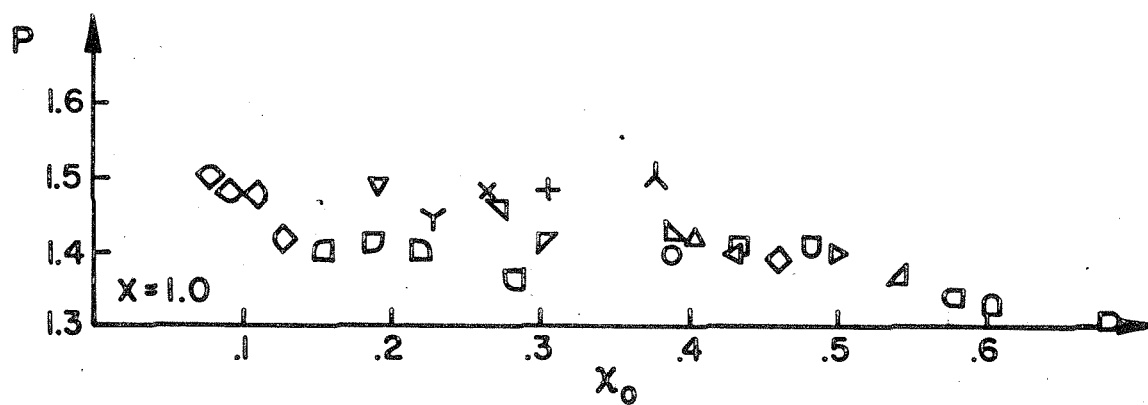
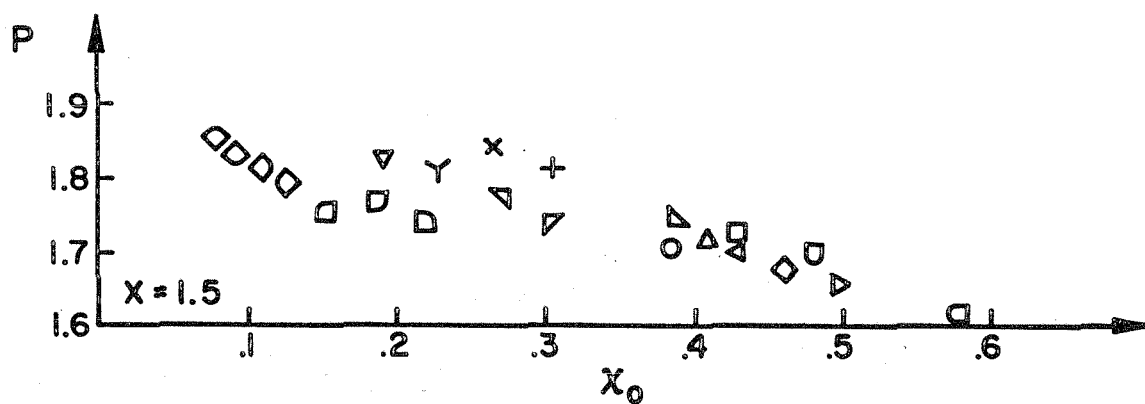
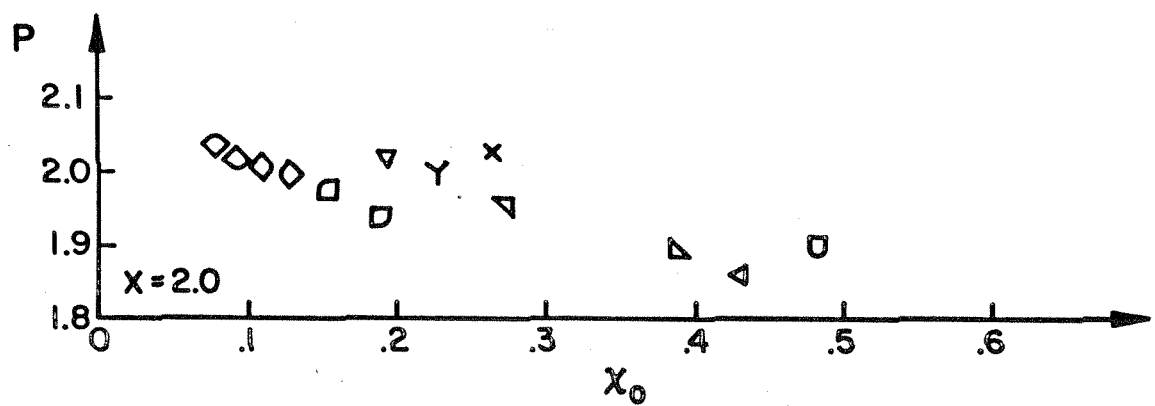


Figure 67. Chapman Correlation Dependence on  $\chi_0$



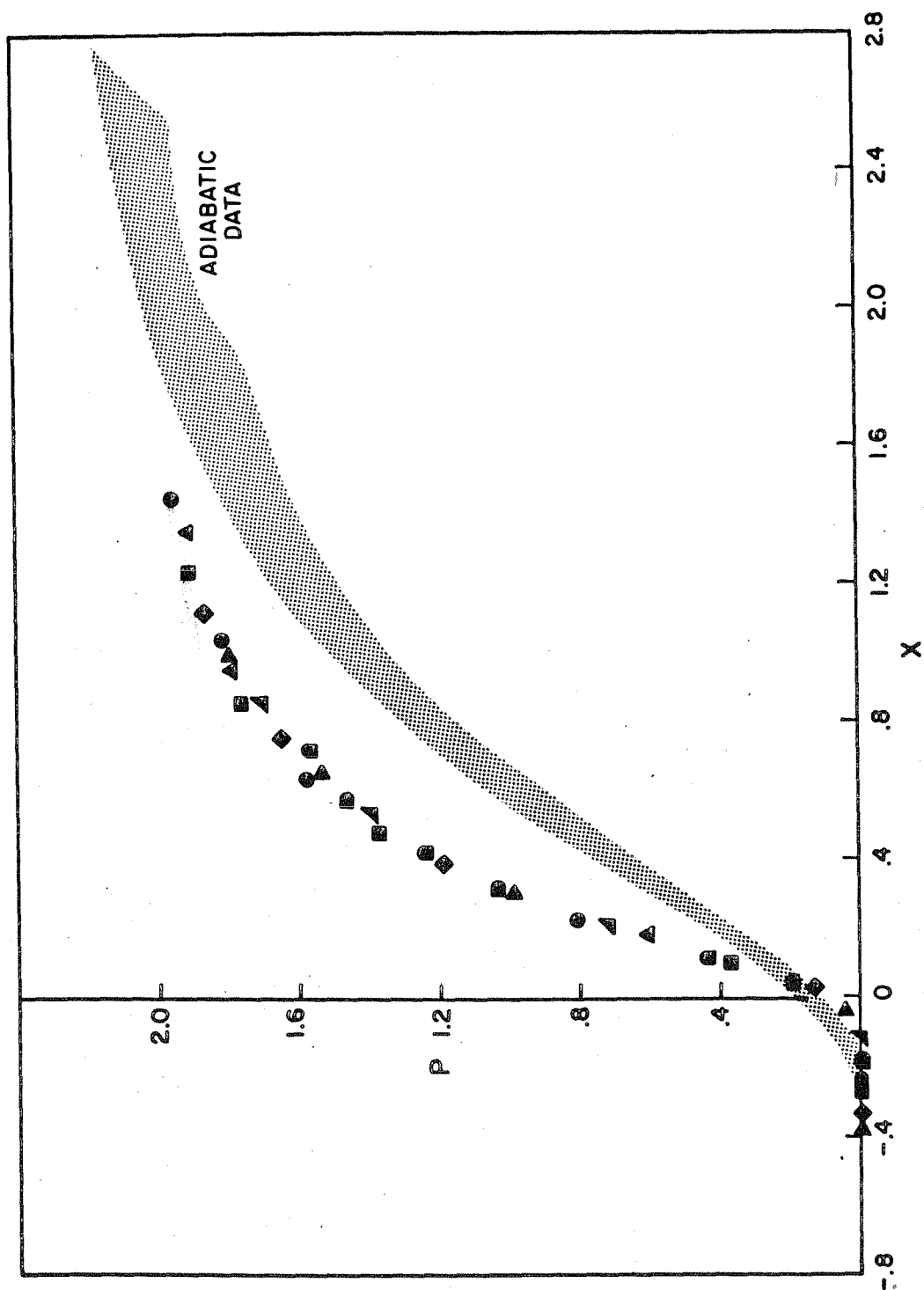


Figure 68. Chapman Correlation (Cold Wall)

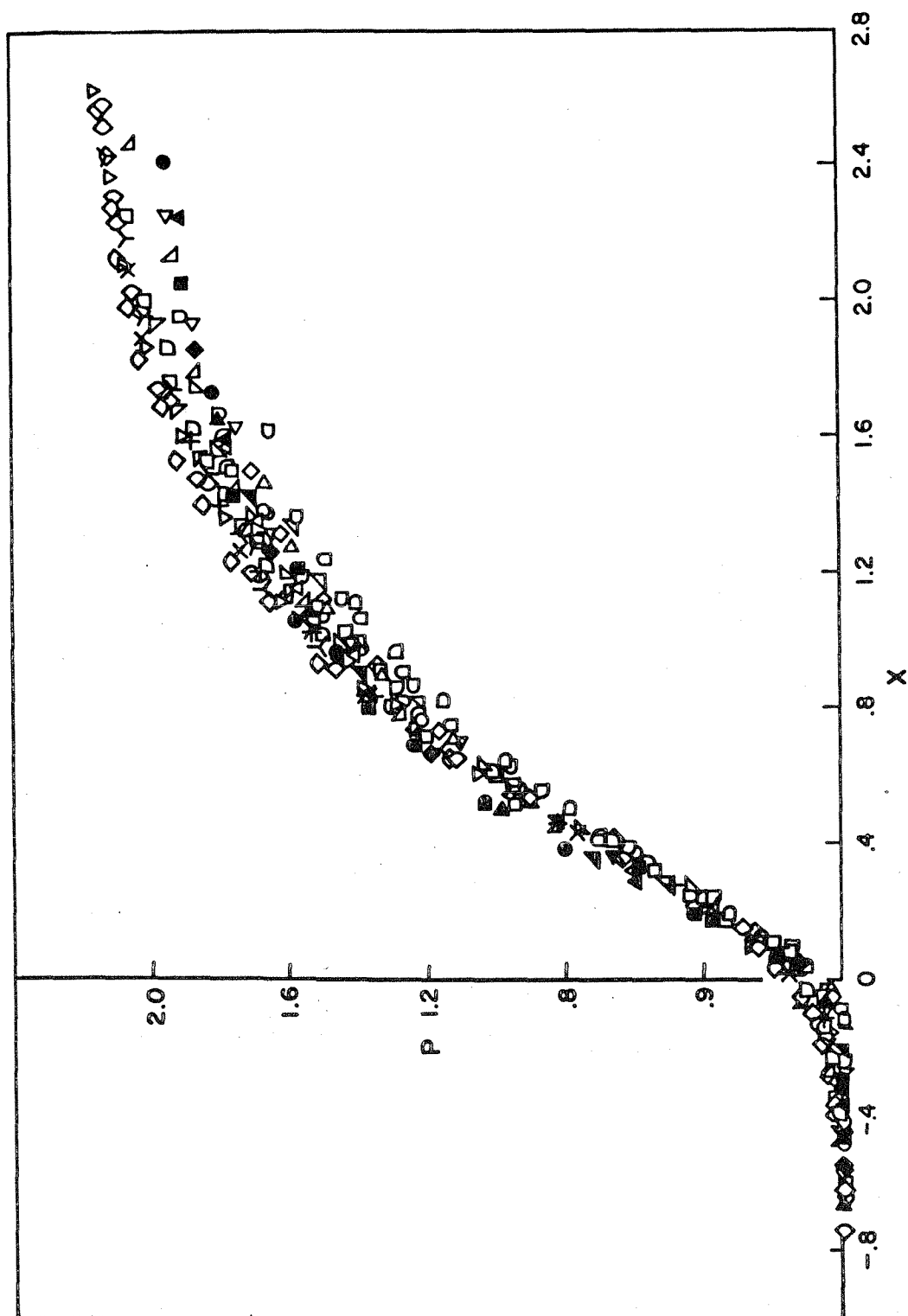


Figure 69. Curle Correlation

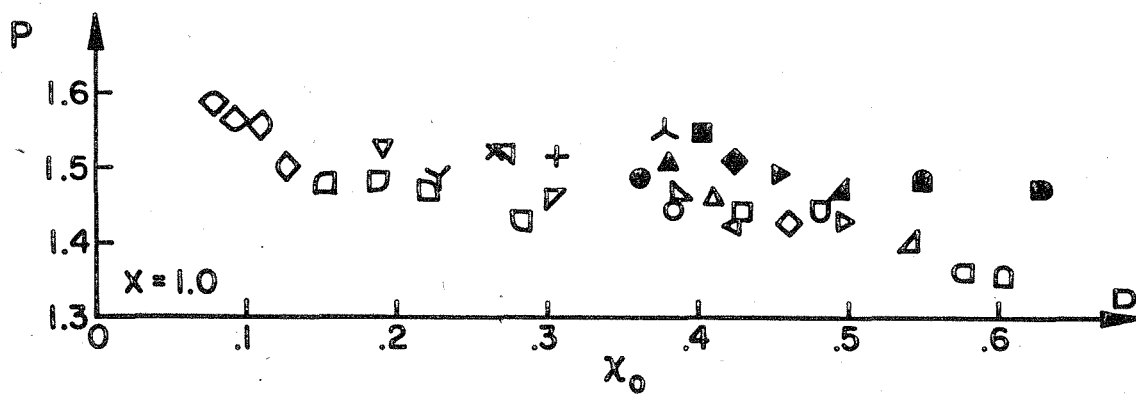
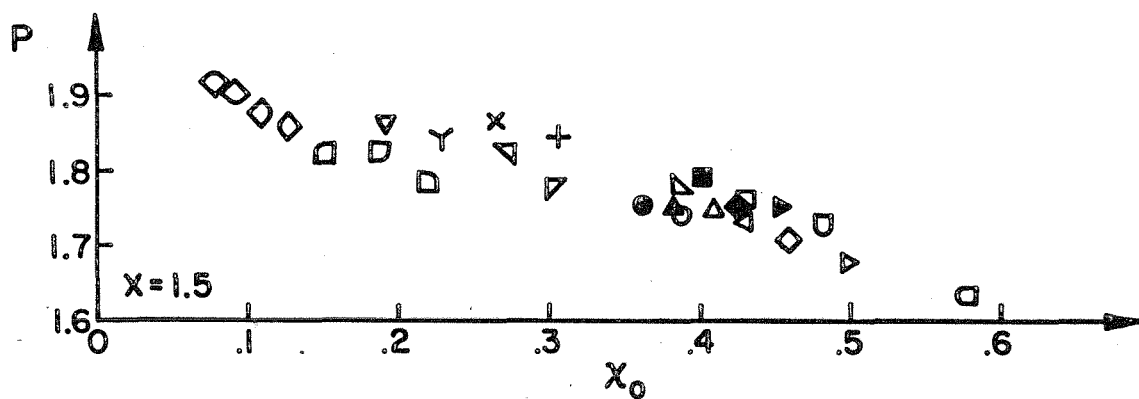
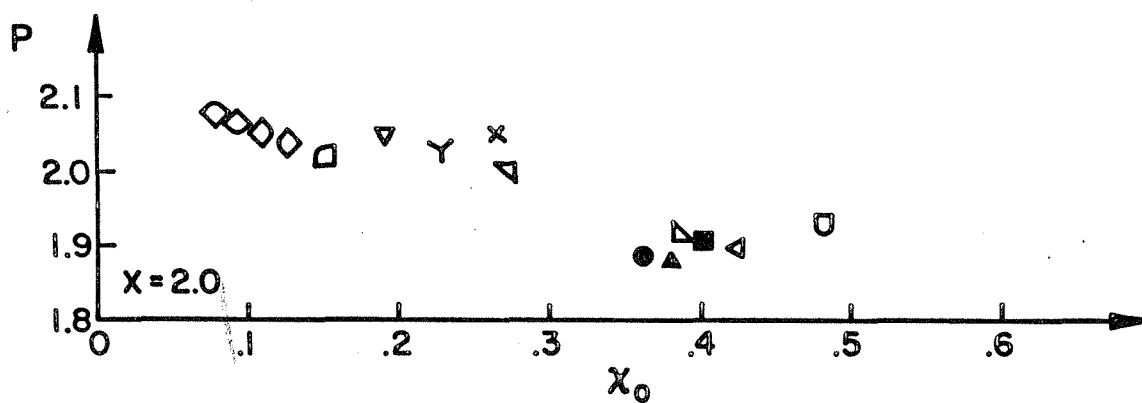


Figure 70. Curle Correlation Dependence on  $\chi_0$

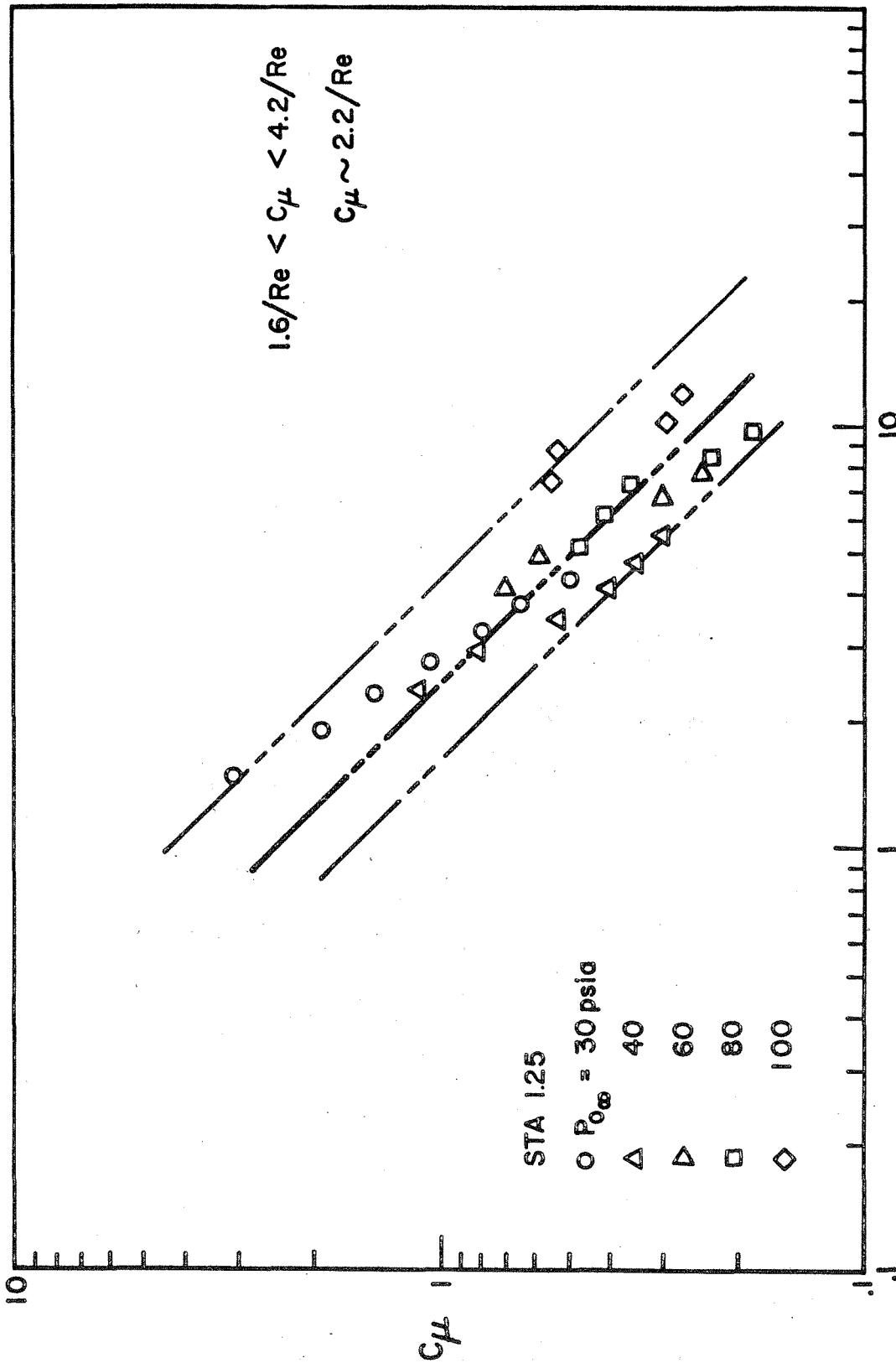


Figure 71. Reynolds Number Correction

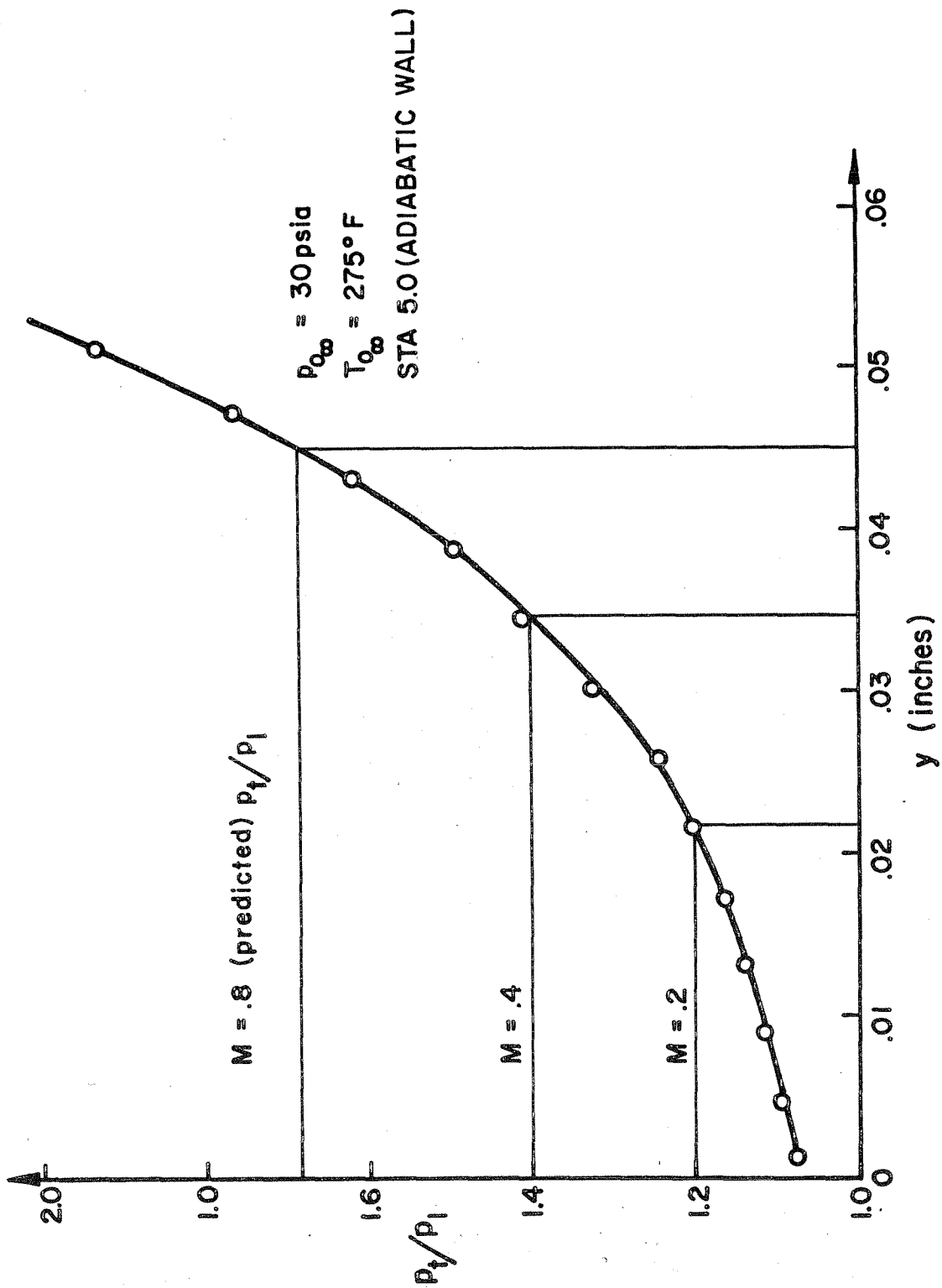


Figure 72. Explicit Subsonic Mach Number Prediction with Viscous Correction